SURFACE AND BULK DEFECTS IN CADMIUM ZINC TELLURIDE AND CADMIUM MANGANESE TELLURIDE CRYSTALS

By

Oluseyi Stephen Babalola

Dissertation
Submitted to the Faculty of the
Graduate School of Vanderbilt University
In partial fulfillment of the requirements
For the degree of

DOCTOR OF PHILOSOPHY

In

Interdisciplinary Materials Science

December, 2009

Nashville, TN

Approved:

Professor Leonard C. Feldman
Professor Arnold Burger
Professor Timothy Hanusa
Professor Jim Wittig
Professor Bridget Rogers
Doctor Ralph James

December, 2009.

Ope ni fun Olodumare

To Mary, Tolu, eleven siblings

ACKNOWLEDGEMENT

I owe my deepest gratitude to Professor Leonard Feldman, my advisor and chair of my Ph.D. committee for his encouragement, supervision and support from my early years in Vanderbilt through my preliminary and qualifying examinations to the concluding level of this thesis.

I am very grateful to Professor Arnold Burger, my co-advisor, for mentoring and supporting me through my advanced degree programs. I am also grateful to Doctor Ralph James for providing me with the opportunity to learn and do research with the brightest minds and world-class equipment. I specifically thank these three aforementioned mentors for creating the atypical inter-institutional collaboration involving Vanderbilt University, Fisk University and Brookhaven National Laboratory towards advancing the science of room temperature nuclear detector materials, and in so doing, expanding my horizon and providing me with an extensive list of scientific equipment and the golden opportunity of working with the best scientists in this field.

I would also like to acknowledge the other members of my committee; Professor Timothy Hanusa, Professor Bridget Rogers and Professor James Wittig for their tutoring and availability to help. I especially thank Prof. James Wittig for providing me with teaching assistantship during my early years at Vanderbilt.

I especially thank my collaborators, colleagues and friends, who have worked countless hours with me, and in so doing, shared laboratories, equipment, office spaces, lecture rooms and stories. I am grateful to Eugene, who introduced me to the

Materials Physics laboratories and the Van-De-Graff accelerator; Dr. Anthony Hmelo, who introduced me to, and helped me in, the VINSE clean room; Mike Groza, who shared his valuable knowledge of CZT detector fabrication and testing, Vladimir Buliga and Constantin Coca, who helped with detector fabrication steps of photolithography and gold sputtering, and to all other scientists at Fisk University's Advanced Materials Science and Applications group. I am grateful to Dr. Stephen Egarievwe for his mentorship and support.

I express my gratitude to Dr. Aleksey Bolotnikov for introducing me to and tutoring me on the Interactive Data Language (IDL) as well as his mentorship in other research areas. I also thank the entire Detector testing group at Nonproliferation and National Security Department of Brookhaven National Laboratory; Anwar, Giuseppe, Ge, Yonggang, Kim, Rubi and my fellow students. I am very grateful to Shirley Kendall and Rosa Palmore of the Diversity office of BNL for their continued help and support.

I thank Shola, Yemi, Funmi and Toyin as well as daddy and mommy for their unwavering and continued camaraderie. Finally, I would like to thank my loves, Mary and Tolu, who help give meaning to all of these. Thank you all. To God be the glory.

Oluseyi Stephen Babalola.

TABLE OF CONTENTS

Page

DEDICATION iii

ACKNOWLEDGEMENTS iv

LIST OF FIGURES x

LIST OF TABLES xiv

Introduction 1

PART ONE: A REVIEW 5

Chapter

I History and Motivation 6

Overview 6

1.1 History of Nuclear Detectors 6

1.1.1 Early Radiation Detectors 7

1.1.2 Recent detectors: Semiconductors 10

1.2 Motivation for CZT Research 13

1.3 Present Status and Challenges 17

1.4 CdMnTe, a new material for room temperature nuclear detector applications 19

References 21

II CZT detector properties, fabrication and operation 25

Overview 25

2.1 CZT properties 26

2.1.1 Crystal Structure 26
2.1.2 Resistivity 28
2.1.3 Charge Transport Properties: 29
2.2 CZT crystal growth and detector fabrication 30
2.2.1 Crystal growth 30

2.3 CZT detector fabrication 33
2.4 CZT Device operation 34
2.5 Nuclear Radiation 35
2.6 Radiation detection 36
2.6.1 Photoelectric absorption 36
2.6.2 Compton scattering 38
2.6.3 Pair Production 39
2.7 Operational Characteristics of Semiconductors 39
2.7.1 Band Structure 39
2.7.2 Charge Carriers 40
2.7.3 Impurities and dopants 41
2.7.4 Trapping and recombination 42
2.7.5 Electrical contacts 43
2.7.6 Leakage current 43
2.7.7 Reverse biasing 44
References 48

PART TWO: ORIGINAL STUDIES 51
III Studies of Surface Condition 52
Overview 52
3.1 Motivation 53

3.2 Experiment 55
3.3 Results and discussion 57
  3.3.1 Micro-characterization of surface roughness 57
  3.3.2 Effect of surface roughness on leakage current 59
  3.3.3 Effect of surface roughness on leakage current 60
  3.3.4 Rough surface as cathode 63
  3.3.5 Rough surface as anode 66
3.4 Conclusion 68
References 69

IV Chemical etching effects on CZT and CMT nuclear detectors 72

Overview 72

4.1 Motivation 73
4.2 Process of chemical etching 74
4.3 Experiment 76
4.4 Results and discussion 77
4.5 Conclusion 84
References 85

V Study of bulk defects in CZT and CMT crystals 88

Overview 88

5.1 Motivation 89

5.2 Defects 89

  5.2.1 Te inclusions and precipitates 90

  5.2.2 Other extended defects 91

5.3 Study of Defects in CZT and CMT crystals. 92

  5.3.1 Infrared (IR) microscopy and analysis 93

5.3.2 Chemical etching to reveal defects in CZT and CMT crystals 95

5.4 Effects of Te inclusions and precipitates on the performance of CZT nuclear detectors 99

5.5 Modeling charge loss due to Te inclusions 101

5.6 Study of defects in CMT nuclear detectors 104

5.6.1 Experiment 104

5.6.2 Results and discussion 107

5.6.3 Studies with Pockels effect 110

5.7 Conclusion 116

References 118

CONCLUSION 122

APPENDICES 125

Appendix A 125

Appendix B 133

LIST OF FIGURES

Figure Page

1.1 Dr. Hampson's Roentgen Radiometer 9
1.2 Herb Parker's free-air ionization chamber and Lind electroscope 11
1.3 Hand-built GM tube with glass wall (1940's) 11
1.4 Radiation Absorption vs. Energy for Typical Detector Materials 14
1.5 Detection efficiency for 100KeV gamma-ray photon in various thicknesses of CdTe, Si and Ge 17
2.1 CZT crystal structure and atomic arrangement in the lattice 26
2.2 Calculated solidus (upper) and liquidus (lower) lines in CdTe-ZnTe pseudo-binary system. 31
2.3 Bridgman growth technique 32
2.4 Traveling heater method of crystal growth 33
2.5 Schematics of three major nuclear detector geometries 34
2.6 Schematics of the operation of a nuclear detector 35
2.7 Schematic of photoelectric absorption 37
2.8 Schematic of Compton scattering 38
2.9 Schematic of pair production process 39
2.10 Band structure for electron energies in materials 40
2.11 Concentration profiles for n-p junction 46
3.1 Schematic diagram of x-ray scanning experimental setup 56
3.2 X-ray scanned images of a 2x2 mm^2 CZT detector surface with smooth polishing, 1µm grit and 3µm polished surfaces 57
3.3 Infrared and x-ray images of CZT crystal surfaces with different roughness 58
3.4 I-V measurement of surfaces with different roughness 60
3.5 Energy band diagram for separated metal and semiconductor 61
3.6 Energy band diagram for an ideal metal semiconductor interface. 61
3.7 Schematic of CZT interfacial charges 63

3.8 IR Image and spectral response of CZT surface with defects 64
3.9 X-ray image and spectral response of a smooth surface 65
3.10 Schematics comparing the images generated when rough cathode, anode are irradiated 67
4.1 IR reflected images of the polished and etched crystal surfaces 79
4.2 IR reflected image of the CZT and the CMT crystal surfaces before and after etching with the P-solution 79
4.3 Plot of the effect of different chemical etchants on CdZnTe crystals 81
4.4 Graph of the effect of aging the etchants in air on the removal of materials from two crystals 81
4.5 AFM images of polished and etched surfaces of the CdZnTe crystals 82
4.6 AFM images of the polished and etched surfaces of CdMnTe crystal 83
5.1 Schematic of formation of Te precipitate and CZT growth interface showing formation of Te inclusion 90
5.2 Schematics of a) edge dislocation, showing an extra plane of atoms, b) twin boundary, a highly symmetric grain boundary 92
5.3 Infrared images of CZT crystal showing grain boundaries, twins, dislocation lines and cracks present on the surface of the crystal 92
5.4 Schematics of automated IR imaging process 94
5.5 Size distribution and 3-D image of the 6 x 6 x 12 mm^3 CZT crystal generated from ~500 IR images showing grain boundaries and twins as decorated by Te inclusions 95
5.6 Nakagawa etching reveals linear etch-pit patterns on the surface of CZT crystals 97
5.7 (a) Schematic representations of the dislocation lines and etch pits; (b, c) two sets of images showing dislocation lines 98
5.8 Correlations between x-ray (bottom) and IR transmission (top) maps measured for a 1 mm thick CZT planar device 100
5.9 ^{60}Co spectra and X-ray scans measured for two Frisch-ring CZT detectors: (a) 11-mm long with a low concentration of Te precipitates, and (b) 16-mm long with high concentration of precipitates 101

5.10 Simulated results using the model described above for 15 mm long CZT detector at 662KeV 103

5.11 Schematic of 6 x 6 x 6 mm^3 CMT crystal showing a layer (plane) of Tellurium inclusions 106

5.12 Concentration and size distribution of Te inclusions in a 1.5x1.5x6 mm^3 region of CMT crystal from (a) ingot 1 and (b) ingot 2 108

5.13 IR images of CMT crystal from ingot 1, a) stitched together to show a 'line' of Te inclusions from one side of the crystal to the other. b) showing the layer of Te inclusion. IR light is parallel to (111) 109

5.14 IR images of 6 x 6 x 6 mm^3 CdMnTe crystals from ingot 2 with cross-polarized IR light at zero bias, showing strain-induced birefringence due to the plane of Te inclusions 110

5.15 Pockel's images of the CMT crystal illustrated in figure 5.11 111

5.16 Electric field distribution evaluated for the CMT crystal a) at -1400 V applied bias and b) at +1400 V applied bias 112

5.17 Electric field distribution of CMT crystal with a) negative bias, and b) positive bias 113

5.18 I-V characteristics measured during Pockels IR imaging, a. for negative bias, and b. for positive bias 113

5.19 Response of two CMT bar detectors from ingot 2 (6x6x12 mm3) to ^{137}Cs in planar configuration 115

A1 Infrared imaging setup 126

A2 Schematics of the process of image capture by the IR system 127

A3 A negative infrared image of a section of CZT crystal showing in-focus and out-of-focus Te inclusions 129

A4 IDL iterative algorithm showing the background subtraction and counting process 130

A5 a) Spectra of inverted intensity b) A stack of 200 images projected on a single plane after background subtraction 131

A6 A 3-dimensional image showing the positions of the Te inclusions in the bulk of a 5 x 5 x 12 mm^3 CZT crystal. 132

B1 Schematics of Pockels effect measurement setup 134
B2 Pockels effect setup at BNL 135
B3 Pockels effect setup showing the sample holder with a CZT crystal, the polarizer, analyzer, high voltage power supply connector and the CCD camera 136
B4 Pockels effect setup. The light source and associated power, as well as the high voltage power supply are seen 137
B5 Flowchart of IDL algorithm for processing Pockels images 139

LIST OF TABLES

Table Page

1 Properties of the major semiconductors used for nuclear detection [13-15] 16

2 Resistivities of Cd1-xZnxTe crystals as a function of x 28

3 Different etching reagents 76

4 Comparison of Te inclusions between ingot 1 and ingot 2 crystals 108

A1 List of the major components of the IR microscopy system 126

INTRODUCTION

The demand for wide band-gap semiconductors for nuclear detector applications has increased in recent years due to an ever growing demand for safeguard measures and medical imaging systems amongst other applications. Of importance in practical applications is the need for these devices to operate at room temperature, be portable and in most cases lightweight and handheld so as to meet the various needs and uses. The main requirements of semiconductor materials for nuclear detector and spectroscopy applications include an optimal energy gap, high average atomic number and stopping power, good charge transport properties and electrical resistivity as well as purity and homogeneity of the materials.

Cadmium Zinc Telluride (CZT) distinctly stands out among the many choices of semiconductor materials for nuclear detection and spectroscopic applications, mainly due to its attractive material properties that makes room temperature operation possible.

A tremendous amount of research is being conducted on improving CZT technology and its implementation into many commercial systems. Applications of CZT detector technology in nuclear nonproliferation and national security as well as medical imaging systems are of special interests. However, CZT devices still face many challenges and drawbacks that must be overcome in order to have new and ideal systems that will answer these application challenges. One such drawback lies in the understanding of the surfaces of CZT detectors and surface effects on detector quality and performance. Another major drawback is the quality of bulk crystals that are commercially available. Commercial crystals have large concentrations of extended defects such as twins, grain boundaries, tellurium inclusions, precipitates and dislocations.

The main objective of this thesis is to study the surfaces of CZT detectors in an effort to optimize the surface processing and thereby improve detector performance. This thesis also addresses the presence of extended defects in bulk CZT crystals. The defects and their effects on performance of CZT nuclear detectors are reported. Lastly, a new material for room temperature nuclear detector applications, Cadmium Manganese Telluride (CMT) is also presented. The properties are compared to those of CZT, and the effects of defects on properties of CMT are discussed. This thesis focuses on four main areas that are crucial to the development of CZT and CMT based nuclear detectors.

The first study aims at understanding the influence of surface roughness on charge transport properties of CZT. The dependence of x-ray irradiation of electrodes on detector response is observed and explained by a theory. The surface roughness was controlled by polishing with different grit sizes coupled with chemical etching and optimized for nuclear detector applications. The resultant surfaces from different etching agents were studied with infrared, both in reflection and transmission modes, and also with atomic force microscope (AFM).

Electric field distributions within the bulk of CZT and CMT crystals were obtained using Pockels electro-optic effect and profiled to observe bulk non-uniformities and defects. Infrared imaging and high resolution x-rays were used to scan the crystals to reveal both intrinsic and extrinsic defects responsible for the non-uniform electric fields. The presence of Te precipitates originating from point defects is correlated with both non-uniformity of electric field within the crystal and detector performance.

Extended defects inside commercial CZT crystals are studied with transmission IR microscopy, white X-ray beam diffraction topography, and surface etching with Nakagawa solution. The effects of these defects on charge transport of charge carriers were studied with a high-spatial-resolution X-ray mapping system.

The results and analyses are reported in six peer reviewed manuscripts and were also presented at conferences. During this research, an experimental setup for Pockels imaging was modified and optimized for direct imaging of the electric field. Also an Integrated Data Language (IDL) programming code was compiled and executed to give a direct profiling of the internal electric field distribution of detectors from Pockels images.

The thesis is divided into two parts. Part 1 is a general review of nuclear detectors and consists of chapters 1 and 2. Chapter 1 presents a brief history of nuclear detectors and discusses the motivation for the work contained in this thesis as well as the present research status and challenges. Chapter 2 presents the CZT and CMT detector properties, fabrication and general operation of nuclear detectors. Part 2 reports the original studies and consists of chapters 3 to 6. Chapter 3 presents the studies of surface morphology that result from different surface processing methods. The effects of surface morphology and roughness on detector performance are also reported. Chapter 4 presents the studies of the effects of chemical etching on CZT and CMT nuclear detectors. Chapter 5 presents the studies of bulk defects on CZT and CMT crystals. A model is presented for estimating the effects of concentration and size distribution of Te inclusions on detector performance. Infrared imaging technique as well as the employment of ‘Pockels effect’ for bulk defect and internal electric field studies are presented. Chapter 6 is a general conclusion that highlights the important results from these studies and how these results have advanced the production of room temperature nuclear detectors from CZT and CMT crystals.

Part One

A review

CHAPTER I

HISTORY AND MOTIVATION

Overview

This chapter gives a brief history of radiation detectors. It discusses the first radiation detectors and how the detection technology had evolved over the years. The recent detectors, semiconductors, as well as the need for room temperature nuclear detectors are discussed. The chapter compares the properties of the current semiconductor nuclear detectors, presents Cadmium Zinc Telluride (CZT) as possessing interesting characteristics for use as a room temperature nuclear detector and discusses the present status and challenges of CZT research. The chapter ends with the introduction of Cadmium Manganese Telluride (CMT) as a new material with interesting properties for room temperature nuclear detector applications.

1.1 History of nuclear detectors

Energetic electromagnetic radiation was observed over a hundred years ago, before any form of radiation detector was in place. Georg Brandes [1] first reported an 'effect' that he saw as a faint 'blue-gray' glow which seemed to originate from the eye itself after dark adaptation followed by placing his eye close to an x-ray tube. Roentgen later reported seeing 'a feeble sensation of light that spread over the whole field of vision' in 1897 [2].

While the mechanism is not completely understood, the observed effects, known as ‘radiation phosphenes’, are assumed to be due to the direct action of the X-rays on the visual pupil of the retina. [3].

Wilhelm Roentgen discovered "X rays" in 1895, for which he received the first physics Nobel prize in 1901. Shortly after, Antoine Henri Becquerel, Pierre Curie and Marie Curie received the 1903 Nobel prize for their discovery of spontaneous radioactivity and joint researches on the radiation phenomena. After these discoveries, better methods to detect and measure radiation were developed.

1.1.1 Early radiation detectors: The first radiation detector can be attributed to Claude Fe´lix Abel Niepce de St. Victor’s observation in 1858 [2] that “a design traced on a sheet of cardboard with a solution of uranyl nitrate and applied on a sheet of sensitive paper prepared with silver bromide, imprints its image.” In 1884, Alfred Ditte commented that “the salts of uranium are capable, long after the exposure to sunlight, of shining invisible rays around themselves”. [2,4]

The first attempt to measure radiation was made by Louis Benoist (1902), who developed a “penetrometer,” designed to measure the quality (energy) of x-rays. The penetrometer consisted of a thin silver disk in the center of a ring of aluminum steps of different thicknesses. The first detectors as film dosimeters were made of photographic plates, dated back to 1907 and reported by Rome Wagner in his address at the 1907 meeting of the American Roentgen Ray Society. Ernest Wollan then incorporated a cadmium filter in his dosimeter in 1944.

Other instruments developed to measure radiation include the calorimeter in which the measurements are usually performed by one of four general methods [5]: measuring the rate of temperature increase in a material with a known heat capacity; measuring the temperature gradient along a heat path (e.g., metal bar) under steady state conditions; measuring the temperature increase in a continual stream of cooling fluid; and measuring liquid evaporation rates. The equipment is rugged and easy to use, and provides an absolute measurement of the fundamental energy emission rate (decay rate). However, calorimetric measurements are not suited for routine work.

Color dosimeters were developed in which a colored disk of barium platinocyanide, known as pastilles, turns darker when exposed to x-rays and its color after exposure is compared with standard scales that correspond to different levels of exposure. Color dosimeters have a simple mode of operation and could provide immediate estimate of high doses. Color dosimeters were deployed by the U.S. Army in the 1950s.

Ionization chambers were developed following J.J. Thomson (1896a, b) and Ernest Rutherford's demonstration (1896) that the new type of radiation could make a normally insulating material, such as air, conductive by stripping small negatively charged particles, now called electrons, from the molecules of the air. They placed two conducting plates with opposite charges at opposite ends of the ionization chambers, maintained a fixed potential between the plates and measured the intensity of x-rays via the chamber's current (1896-1899). Different modifications of the ionization chamber include the free-air ionization chamber and the liquid ionization chamber.

Figure 1.1: a) Dr. Hampson's Roentgen Radiometer (1901 to 1925) consists of 6 small half-moon shaped pastilles that change color in response to incident radiation, b) U.S. Army colorimetric dosimeter (1950s), [2].

Ionization chambers are operated in pulse mode as well as in integrating mode. In the pulse mode, an alpha-emitting sample located inside the chamber emits alpha-particle pulses that are large enough to be counted and permit pulse height analysis. The Frisch grid ion chamber [6] is an alpha-particle spectrometer that has resolution comparable with that of semiconductor detectors. In most cases, however, the ion chambers operate in an integrating mode due to the small size of individual pulses. Electroscopes were developed to measure the rate at which a stored charge decreases.

Geiger Muller (GM) counters were developed in 1923 [7,8,9]. These are nuclear detectors that consist of a cylindrical tube with the outer wall serving as the cathode and a fine wire stretched along the axis of the tube serving as the anode. Light sensitive GM tubes were used to convert light emissions from scintillators into electrical pulses. GM tubes could operate in current as well as in pulse modes.

The advantages of GM detectors over photomultiplier tubes (PMT) are simpler associated electronic circuits as well as the ability to detect single photoelectrons. However, GM tubes have large dead times and did not respond well to the long wavelengths associated with most scintillators.

Another type of radiation detector that was developed are the fluoroscopes, such as the barium platinocyanide detectors (also known as fluoroscopes,) which were portable and allowed an immediate visualization of the x-ray reflector, and intra-oral fluoroscope. Other scintillator counters developed include various photomultiplier tubes (PMTs), zinc sulfide alpha scintillation counters, liquid scintillation counters and plastic scintilators.

1.1.2 Recent detectors: Semiconductors: Solid state detectors are the most recent class of detectors developed. These detectors operate by converting the incident photons directly into electrical pulses. The first modern semiconductor detector, a reverse-biased p-n junction detector, was built at Bell Laboratories by Kenneth McKay in 1951 [10] and used to detect alpha particles and the first lithium-drifted germanium (Ge) detector for high-resolution gamma spectroscopy was developed by Alister Tavendale and George Ewan of Chalk River Laboratories in 1963. [11].

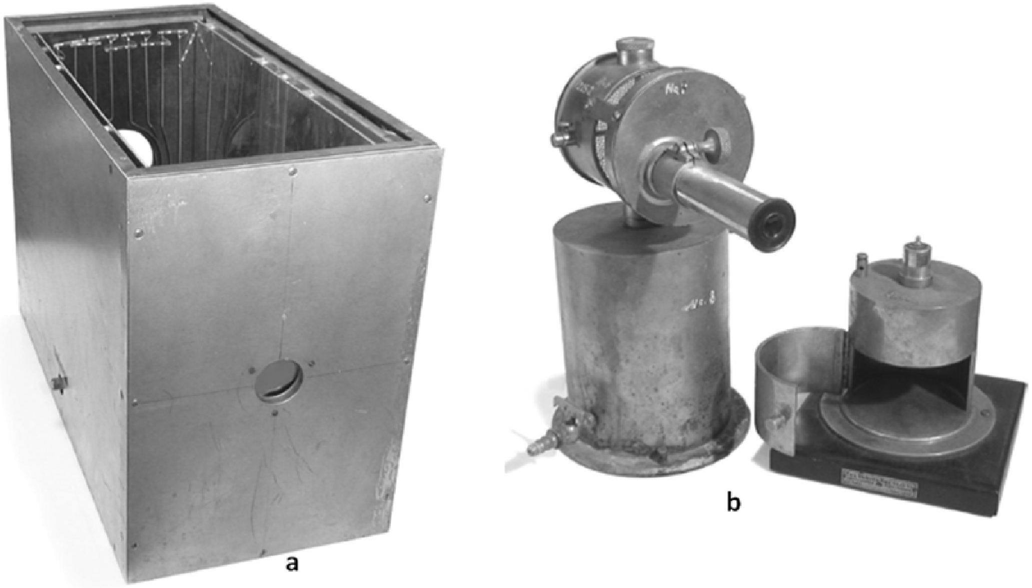

Figure 1.2: a) Herb Parker's free-air ionization chamber (1935-1940) with top cover removed to reveal guard wires on the back wall of the chamber. b) Lind electroscope (1920 – 1930) with two interchangeable chambers, one (left) is mounted on a flow-through ion chamber for random measurements while the other (right) is for measuring solid samples [2].

Figure 1.3: Hand-built GM tube with glass wall (1940's). A cylindrical copper tube serves as cathode. The ends of the tube are coated with wax to reduce leakage currents [2].

By 1964, Ge (Li) detectors had replaced NaI scintillation crystals in most gamma ray studies. [12]. This was enabled by efforts at Oak Ridge National Laboratory to produce Ge with impurity levels below 10^{10} cm^{-3} to remove the need for lithium compensation. This led to production of commercial high purity germanium (HPGe) detectors. Solid state detectors are fabricated from a variety of materials including: germanium, silicon, cadmium telluride, mercuric iodide, and cadmium zinc telluride. The best detector for a given application depends on several factors. Ge detectors have superb resolution due to the extremely large number of charge carriers are a result of the narrow band-gap of less than 1 eV.

Unfortunately, the narrow band-gap characteristic creates a significant potential for thermally generated noise which can only be reduced by operating the detector at low temperatures. For this reason Ge detectors require cryogenic cooling, which makes them expensive, bulky and therefore impractical for portable applications. Silicon, on the other hand, needs no cooling, but is inefficient in detecting photons with energies greater than a few tens of kilo electron volts (keV). In the last few years detectors fabricated from high atomic number semiconductor materials have gained acceptance due to their ability to operate at room temperature and their inherent high efficiency. Detectors made from cadmium telluride, mercuric iodide, and cadmium zinc telluride are routinely used. Large band-gap materials can be used to produce room temperature semiconductor materials, but this involves sacrificing resolution and size limitation, which limits the detection efficiency at high energies.

1.2 Motivation for CZT research

The use of a solid detection medium has many advantages. One advantage of solid state detectors is their small and controllable sizes. Solid state detector dimensions are kept much smaller as compared with equivalent gas filled detectors due to solid density being 1000 times greater than that of gases. Within the solid state detector classes, semiconductor diode detectors have advantages over scintillators in their processes of operation. Scintillators are also compact but yield poor energy resolution as the scintillating process involves many inefficient steps. Energy of the order of 100 eV is required to produce one photoelectron, so that a smaller number of information carriers are produced and statistical fluctuations place a limit on energy resolution. To reduce statistical limits one needs to increase the number of information carriers per pulse, which is achieved by using semiconductor materials as radiation detectors. Other advantages of semiconductor materials as radiation detectors include relatively fast timing characteristics, variable effective thickness and ruggedness for field applications. Limitations however could be small size and susceptibility to performance degradation from radiation damage.

There are some key properties that x-ray and gamma ray detector materials must possess. These include:

a. High atomic number of absorbent material: The rate of photoelectric interaction, which is the prominent interaction in the operation of nuclear detector devices, increases with increase in atomic number (Z^4 to Z^5).

b. High band-gaps of more than 1.3 eV are needed for room temperature operation with low noise level. However, probability of trapping and electron hole pair production energy increases with increasing band-gap. Optimal values of band-gap are 1.5 to 2.2 eV.

c. Resistivity: Semiconductors must have absolute value of net electrically active impurity concentration (N_a - N_d) less than 10^{11} free carriers per cm^3 at room temperature, which is equivalent to a resistivity of 10^8 – 10^9 Ω.cm. Materials with high atomic numbers, require thicknesses of about 2 mm to absorb the major fraction of gamma rays in the 100 keV range.

d. Small transit time of carriers across active volume of detectors is needed to reduce trapping probabilities. Trapping of carriers due to discrete levels in the band-gap introduced by defects affect average carrier lifetime, mobility and electron-hole pair creation energy. Detector materials must be produced with a great degree of purity and crystalline perfection.

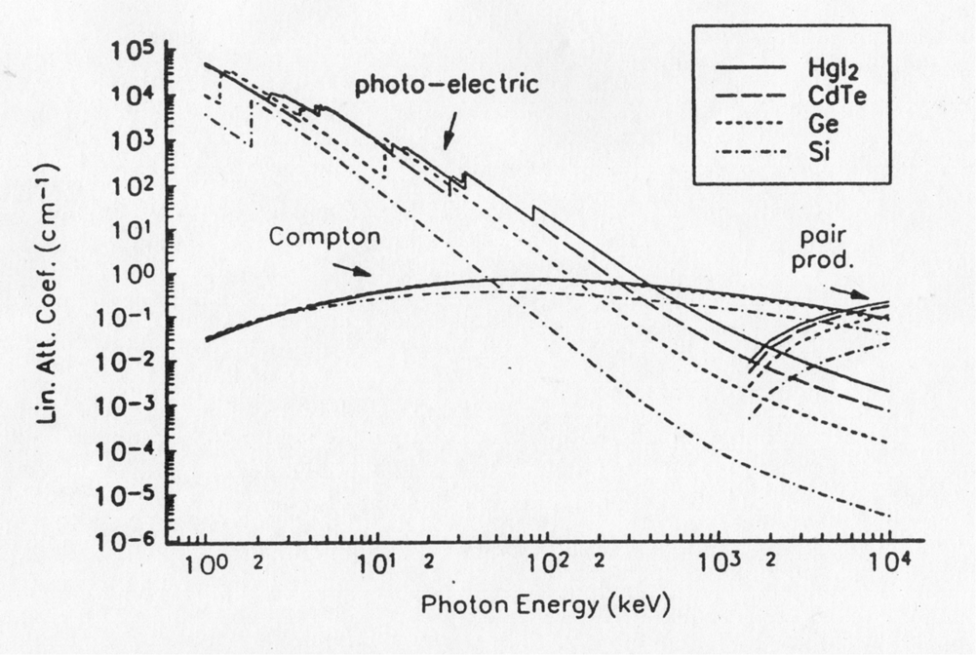

Figure 1.4: Radiation Absorption vs. Energy for Typical Detector Materials [13].

Figure 1.4 shows the excitation processes in different radiation detector materials as a function of photon energies. Cadmium telluride (CdTe) and mercuric iodide (HgI_2) are the main materials that satisfy the above criteria. CdTe has advantages of stability and less toxicity than HgI_2. CdTe crystals are more stable in air than HgI_2, which require encapsulation to prevent deterioration of the crystal surfaces on exposure to air over periods of weeks to months.

CdTe combines relatively high atomic numbers (48 and 52) with large bandgap energy (1.47 eV) to allow for room temperature operation. The probability of photoelectric absorption per unit path-length is roughly 4-5 times higher in CdTe than in Ge, and 100 times larger than in Si for typical gamma ray energies. However, CdTe has some drawbacks such as poor collection efficiency of holes that limit the achievable energy resolution. Also CdTe is very expensive to grow into big sizes. This small size limitation makes instruments less sensitive to gamma emitting sources. CdTe sometimes display effects in which counting rates or peak positions change with time, known as polarization effects [2].

A new material, cadmium zinc telluride (CZT), formed by alloying CdTe with ZnTe, is found to be better than CdTe for spectroscopic applications. Firstly, alloying ZnTe with CdTe increases the bandgap from 1.44 in CdTe to about 1.7 in CZT. The increased bandgap provides an immediate solution to the problem of noise due to leakage current in CdTe and allows for use at either lower photon energies or higher temperatures. Also CZT crystals can be grown to larger sizes at a reduced cost compared to CdTe crystals.

High atomic number also provides good stopping power for energetic photons. All these properties allow for producing rugged, compact devices for field applications, and make CZT detectors more desirable than CdTe in detector and applications.

Table 1: Properties of the major semiconductors used for nuclear detection [14-16]

	Si	**Ge**	**HgI_2**	**CdTe**	**CdZnTe**
Atomic Number	14	32	80, 53	48, 52	48, 30, 52
Density (g/cm^3)	2.33	5.32	6.4	6.06	6.06
Band gap (at Temperature, eV)	1.115 (300K) 1.165 (0K)	0.665 (300K) 0.746 (0K)	2.13	1.44	1.6 - 1.7
Ave. Energy/e-h pair (eV)	3.61	2.98	4.2	4.43	4.7
Electron Mobility (cm^2/Vs)	1350	3900	100	1100	1100
Hole Mobility (cm^2/Vs)	480	1800	4	100	100
Electron $\mu\tau$ Product (cm^2/V)	2.7 x 10^{-2}	0.72	10^{-4}	10^{-3}	10^{-3}
Hole $\mu\tau$ Product (cm^2/V)	9.6 x 10^{-3}	0.84	10^{-5}	5 x 10^{-5}	3 x 10^{-5}
Operating Temp. (K)	300	77	300	300	300

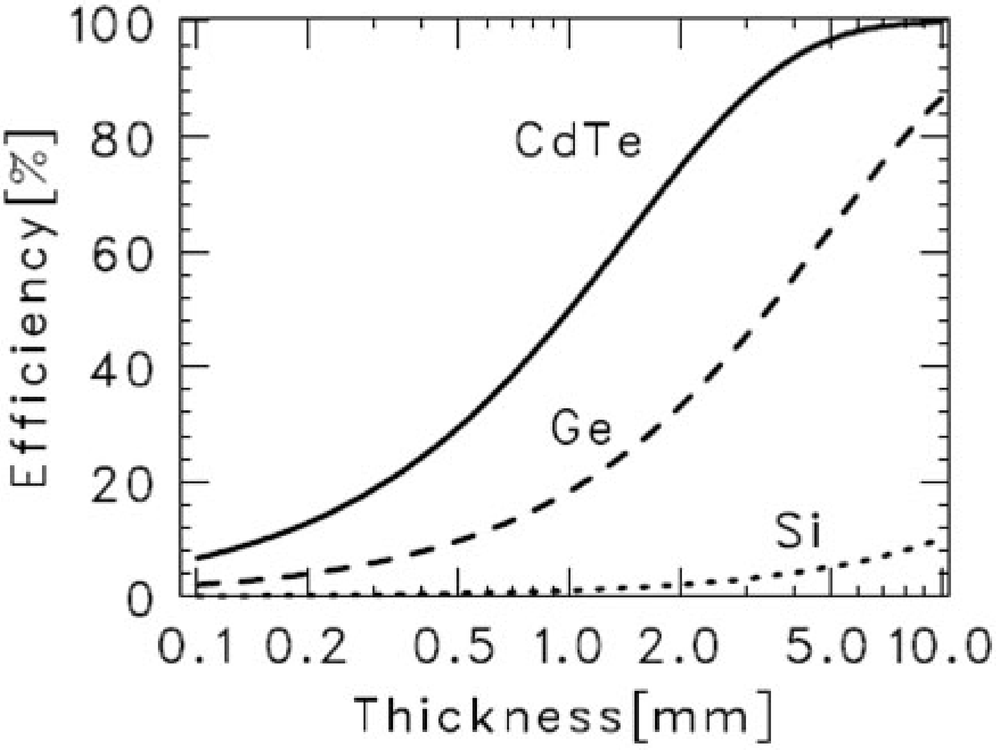

Figure 1.5: Detection efficiency for 100KeV gamma-ray photon in various thicknesses of CdTe, Si and Ge. [17]

1.3 Present status and challenges

Detection of low energy x-rays (less than 200 KeV) is achieved by using CZT detectors of 6 mm or less thickness. Low energy detection is adequate for x-ray astronomy and gamma-camera imaging in nuclear medicine. One major deployment of CZT crystal in applications include the Burst Alert Telescope (BAT) onboard the SWIFT Gamma-Ray Burst (GRB) explorer launched by NASA on November 20th, 2004. BAT consists of 32,768 CZT ($Cd_{0.9}Zn_{0.1}Te_1$) detectors of 4x4 mm^2 large and 2 mm thick dimensions to form a 5,243 cm^2 detector plane. The CZT crystals, manufactured by eV Products Inc, observe an energy range of

15 to 150 KeV and have energy resolution of ~6 KeV (FWHM) at 122 KeV. (see references 18-21 for publications relating to BAT). However, large volume CZT detectors are in great demand for high energy applications such as spectrometers for homeland security uses. These applications require that the detector has good (less than 1%) energy resolution.

Technologies for growing large volume single crystal CZT have been significantly improved of recent, thereby allowing for making CZT devices with extended thicknesses and effective active volumes for gamma ray detection and imaging. [22, 23]

However, large CZT detectors are still uncommon. The largest single crystal CZT detectors reported are 6 cm^3 pixellated CZT devices in quantities of tens [24]. The major limiting factor for realization of large volume CZT detectors is the high concentrations of extended defects in today's CZT crystals. These defects include Te inclusions, twins, grain and sub-grain boundaries and dislocations. The extended defects can impair the performance of semiconductor devices. Their specific effects were thoroughly investigated in many semiconductors, especially Si and Ge [25]. This thesis is focused on study of the extended defects, especially Te inclusions. The techniques used for this study include the high-spatial-resolution X-ray mapping system, transmission infrared (IR) microscopy and infrared imaging employing the Pockels' electro-optic effect. The results have led to better understanding of the roles of defects in CZT nuclear detector performance.

1.4 CdMnTe, a new material for room temperature nuclear detector applications.

Cadmium manganese tellurium (CdMnTe or CMT) has recently been shown to be a promising material for room temperature nuclear detector semiconductor [26,27] as well as other applications [28,29]. Advantages of CMT include better lattice strengthening [30] and wider bandgap energy in comparison to CdTe due to the addition of Mn. The energy bandgap of CMT has been found to increase at a rate of 13 meV per atomic percent of Mn [31], which is twice as fast as 6.7 meV per atomic percent of Zn added to CdZnTe, the reported rate at which Zn increases the band gap in CdZnTe [32] Mn in CdTe has a segregation coefficient of 0.95 and axial distribution of 0.001 mole fraction [33]. The near-unity segregation coefficient of Mn in CdTe crystal compared to 1.35 for Zn in CdTe results in a more homogeneous Mn distribution and therefore more uniform CMT crystals.

For CMT to become advantageous in gamma ray detector applications, high quality crystals are needed. Crystals should have good uniformity of composition and low defect concentrations. However there are problems associated with production of good quality defect-free CMT crystals. Commercially available Mn used for CMT crystal growth has a low purity of about 99.99%, so that there is need to further purify Mn and achieve lower impurity concentration. Also CMT crystals grown by Bridgman method are found to contain high concentration of twins [32]. Twin boundaries are highly decorated with Te inclusions. Te inclusions have been identified in CdTe crystals as solidified Te-rich melt captured at the interface of crystal growth due to morphological instabilities and incorporated into the ingot [33, 34]. They are usually ≥1 micron [35-37]. The effects of such twins and associated Te inclusions on CMT nuclear detector devices however have not been well documented.

REFERENCES

1. Brandes GSB. Preuss Akad Wiss 1:547; 1896
2. P. W. Frame, Health Physics, June 2005, Volume 88, Number 6 pp 612 – 637
3. Steidley KD, Eastman RM, Stabile RJ. Observations of visual sensations produced by cerenkov radiation from highenergy electrons. Int J Radiat Oncol Biol Phys 17:685– 690; 1989
4. 1884 edition of the Encyclope´die Chimique,
5. Posey JC. Calorimetry for measuring radioactivity. Isotop Rad
    1. Tech 1:92–95; 1963.
6. Frisch O. British atomic energy report. BR-49; 1944
7. Geiger H. A method of counting alpha and beta rays. Deutsch Phys Ges 15:534 –539; 1913.
8. Geiger H, Muller W. Elektronenzahlrohr zur messung schwachster aktivitaten. Naturwissenschaften 16:617– 618; 1928b (in German).
9. Geiger H, Muller W. Das Elektronenzahlrohr I. Wirkungsweise, Herstellung Eines Zahlrohrs. Phys Zeit 29:839–841; 1928a (in German)
10. McKay KG. Electron-hole production in germanium by alpha particles. Phys Rev 84:829–832; 1951.
11. Tavendale AJ, Ewan GT. A high resolution lithium-drift germanium gamma-ray spectrometer. Nuc Instr Meth 25:185–187; 1963.
12. Shirley DA. Applications of germanium gamma-ray detectors. Nucleonics (March):62– 66; 1965.

13. T.E. Schlesinger and R.B. James Eds.; Semiconductors for Room Temperature Nuclear Detector Applications; Semiconductors and Semimetals, Vol. 43, Academic Press 1995, pp 497.
14. G. F. Knoll, Radiation Detection and Measurements, Wiley, New York 3rd edition (2000).
15. E. Sakai, Nucl. Instr. And Meth. 196, (1982), pp 121-130
16. Y. Eisen, Nucl. Instr. And Meth. A380, (1996), pp 431 – 439
17. T. Takahashi and S. Watanabe. IEEE Trans. Nucl. Sci., Vol. 48, No. 4 (2001) pp. 950-959.
18. G. Sato et al. Properties of CdZnTe detectors in the Burst Alert Telescope (BAT) array. Hard X-Ray and Gamma-Ray Detector Physics V. Edited by Franks, Larry A.; Burger, Arnold; James, Ralph B.; Hink, Paul L. Proceedings of the SPIE, Volume 5198, pp. 209-216 (2004).
19. G. Sato et. al. Development of a spectral model based on charge transport for the Swift/BAT 32K CdZnTe detector array Nuclear instruments & methods in physics research. Section A 2005, vol. 541, no 1-2, pp. 372-384.
20. Masaya Suzuki, Makoto Tashiro, Goro Sato, Shin Watanabe, Kazuhiro Nakazawa, Tadayuki Takahashi, Yuu Okada, Hiromitsu Takahashi, Ann Parsons, Scott Barthelmy, Jay Cummings, Neil Gehrels, Derek Hullinger, Hans Krimm, Jack Tueller Hard X-Ray Response of CdZnTe Detectors in the Swift Burst Alert Telescope IEEE Trans. Nucl. Sci. Vol. 52, No. 4, 2005, page 1033

21. Ann Parsons, Jack Tueller, Hans Krimm, Scott D. Barthelmy, James Cummings, Craig Markwardt, Derek Hullinger, Neil Gehrels, Ed Fenimore, David Palmer, Goro Sato, Kazuhiro Nakazawa, Tadayuki Takahashi, Shin Watanabe, Yuu Okada, Hiromitsu Takahashi, Masaya Suzuki, Masaya, Makoto Tashiro: Swift/BAT calibration and the estimated BAT hard x-ray survey sensitivity Hard X-Ray and Gamma-Ray Detector Physics V , SPIE, 5165, pp. 190-200, 2003
22. H. Chen, S. A. Awadalla, K. Iniewski, P. H. Lu, F. Harris, J. Mackenzie, T. Hasanen, W. Chen, R. Redden, G. Bindley, I. Kuvvetli, C. Budtz-Jørgensen, P. Luke, M. Amman, and J. S. Lee, J. Appl. Phys., v. 103, pp. 014903, 2008.
23. C. Szeles, IEEE Trans. Nucl. Sci., NS 51, n.3, pp. 1242-1249, 2004.).
24. Z. He, F. Zhang, "The First Polaris 3-D CdZnTe Detector Array System", presented at IEEE Nuclear Science Symposium and Medical Imaging Conference, 2007 October 27 – November 3, Honolulu, Hawaii, USA Published? If not, put (Unpublished).
25. H. F. Matare, "Defects Electronics in Semiconductor", Wiley-Interscience, 1971.
26. A. Burger, K. Chattopadhyay, H. Chen, J. O. Ndap, X. Ma, S. Trivedi, S. W. Kutcher, R. Che, and R. Rosemeier. J. Crysal Growth 198/19 (1999) 872.
27. A. Mycielski, A. Burger, M. Sowinska, M. Groza, A. Szadkowski, P. Wojnar, B. Witkowska, W. Kaliszek, and P. Siffert, Phys. Stat. Sol. (c) 2, No. 5, (2005) 1578.

28. A. Hossain, Y. Cui, A. e. Bolotnikov, G. S. Camarda, G. Yang, D. Kochanowska, M. Witkowska-baran, A. Mycelski and R. B. James ,Vanadium-doped CMT crystals as X- and gamma ray detectors. Journal of Electronic Materials. (2009) *In Press.*
29. G. A. Brost, K. M. Magde, S. Trivedi, Opt. Mater. 4 (1995), 224.
30. U. Hommerich, X. Wu, V. R. Davis, S.B. Trivedi, K. Grasza, R. J. Chen, S. Kutcher, Opt. Lett. 22 (15) (1997) 1180.
31. Y. R. Lee and A. K. Ramdas, Solid State Commun. 51 (1984) 861.
32. A. Y. Wu and R. J. Sladek, J. Appl. Phys. 53 (1982) 8589.
33. S. Sen and J.E. Stannard, Semiconductors for Room Temperature Radiation Detector Applications, Vol. 302, eds. R.B.. James,T.E. Schlesinger, P. Siffert, and L. Franks (Pittsburgh,. PA: Materials Research Soc.), (1993) 391
34. C. J. Johnson, E. E. Eissler, S. F. Cameron, Y. Kong, S. Fan, S. Javanovic, and K. G. Lynn, Semiconductor for Room Temperature Radiation Detector Applications, R. B. James, T. E. Schlesinger, P. Siffert, and L. Frank, Eds. (Pittsburgh, PA: Materials Research Soc.), vol. 302 (1993) 463.
35. J. Gonzales-Hernandez, E. Lopez-Cruz, D. D. Allred, and W. P. Allred, J. Vac. Sci. Technol. A 8 (4), (1990) 3255.
36. P. De Antonis, E. J. Morton, and F. J. W. Podd, IEEE Trans. Nucl. Sci. 43, no. 3, (1996) 1487.
37. P. Rudolph, M. Neubert and M. Miihlberg. Journal of Crystal Growth 128 (1993) 582.

CHAPTER II

CZT DETECTOR PROPERTIES, FABRICATION AND OPERATION

Overview

To fully understand the importance of studying the defects in CdZnTe and CdMnTe crystals, the detector properties and fabrication processes need to be understood and considered. Some fabrication process steps can introduce defects on the surface of the crystal, such as disruption of the atomic surfaces as well as residues from chemical polishing and etching processes. Also handling of the crystals is important as improper handling can induce stress within the bulk of the crystal or propagate dislocations which will affect the operation of the crystal as a nuclear detector. This chapter starts with a discussion of the material properties that make CZT crystals highly desirable for gamma ray detectors. It goes on to detail the principles behind operation of CZT as a nuclear detector. The discussion covers the types of interaction between nuclear radiation and atoms of CZT and the energy spectrum generated as a result of these interactions. The general process of CZT detector fabrication is also discussed. It should be noted that CZT crystals have a wide variety of applications but the discussion is mostly limited to its use in nuclear detection applications.

2.1 CZT properties

2.1.1 Crystal Structure: CdZnTe crystals have a building block of two interpenetrating face center cubic (FCC) sub-lattices that are apart by one-quarter of a unit cell body diagonal. Cd or Zn nuclei occupy one sub-lattice while Te occupies the other. These lattice nuclei arrangements result in a zinc blende (Zinc Sulfide) crystal structure [1].

Cadmium Zinc Telluride atoms are primarily held together by covalent bonds, as are zinc blende structured semiconductors, hence valence band electrons are shared. Covalent crystals have no partially filled bands in k-space (which corresponds to k-levels). [2]

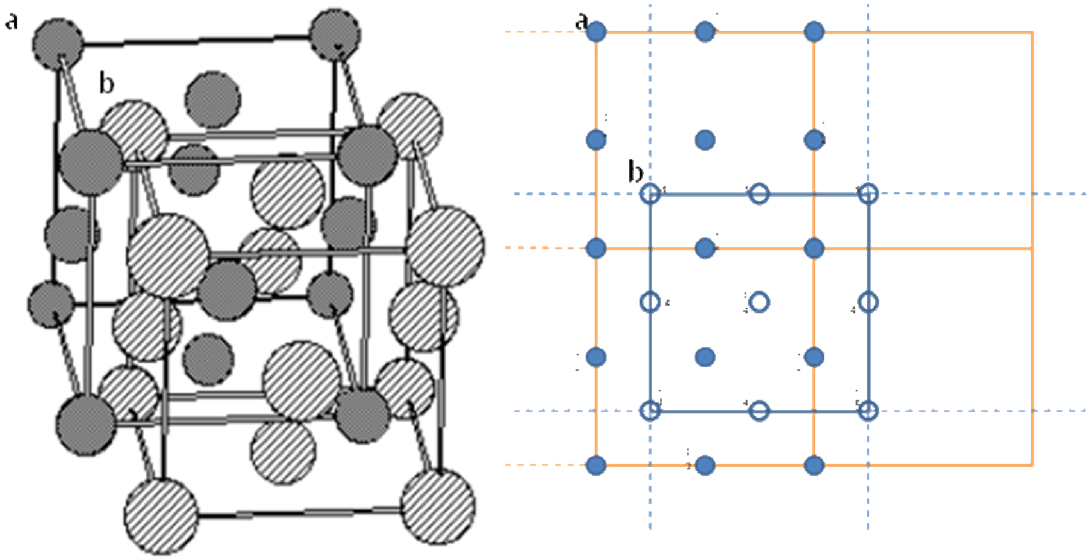

Figure 2.1. CZT crystal structure and atomic arrangement in the lattice. a. represents Cd (or Zn) atoms while b. represents Te atoms.

CZT crystals have a FCC Bravais lattice with a two-point basis $\sigma_1 = (0,0,0)$ and $\sigma_2 = (\frac{1}{4}a, \frac{1}{4}a, \frac{1}{4}a)$ as shown in Figure 1b above. The geometric structure factor is given by

$$S(q) = \sum_{i=1}^{2} f_i e^{j(\sigma_i \cdot q)} \qquad \text{.............. (1)}$$

where q is the scattering vector and f_1 and f_2 are the atomic form factors for Cd (or Zn) and Te respectively. The Bragg peak q equals the reciprocal lattice vector, K, hence structure factor becomes

$$S(K) = \sum_{i=1}^{2} f_1 + f_2 e^{j(\sigma_i \cdot q)} \qquad \text{......... (2)}$$

In Zinc blende structures f_1 and f_2 are different so that the structure factor never equals zero. The crystal thus has the same set of diffraction peaks as FCC crystals with different relative amplitudes [3]. The CZT alloy can then be described as CdTe crystal with Zn atoms randomly substituting Cd atoms.

The lattice constants of CdTe and ZnTe are 6.482Å and 6.104Å respectively. The CZT lattice constant can therefore be estimated using a linear approximation from Vegard's Law [4] given by

$$a(x) = a_1(1-x) + a_2 x \qquad \text{..................... (3)}$$

where a_1 and a_2 are lattice constants of CdTe and ZnTe respectively. The difference in lattice constants of CdTe and ZnTe shows that Zinc substitution of Cd atoms results in small change in average unit cell dimensions. Extended X-ray Absorption Fine Structure (EXAFS) [5] measurements suggest distortion of the Te sub-lattice as shown by a bimodal distribution of bond lengths. X-ray diffraction and Bragg's law ($n\lambda = 2dSin\,\theta$, where λ is the wavelength of x-rays, d is plane spacing within the lattice, θ is the angle between incident ray and scattering plane and n is an integer) is used to estimate average lattice constants. The distance between planes, d, is directly proportional to a, and depends on crystal orientation. Lattice constants can be more accurately determined by using high resolution triple axis X-ray diffraction with well oriented crystals [6].

2.1.2 Resistivity: The materials properties required for a good room temperature nuclear detector include high resistivity and long lifetime of charge carriers. Zinc telluride has a higher bandgap than CdTe so that alloying CdTe with Zn increases the bandgap and intrinsic resistivity of CZT from 10^{10} Ωcm to over 10^{16} Ωcm. Butler et al [7] observes an increase of about two orders of magnitude in the resistivity of CZT as the fraction of zinc is increased as shown in table 2.1. This increase in resistivity translates to a decrease in leakage current.

Table 2 Resistivities of $Cd_{1-x}Zn_xTe$ crystals as a function of x. Crystals were grown by the high pressure Bridgman technique. (Extracted from [7])

Composition	**Resistivity (Ω-cm)**
CdTe	3.0×10^9
$Cd_{.96}Zn_{.04}Te$	2.5×10^{10}
$Cd_{.8}Zn_{.2}Te$	$2.5 X 10^{11}$

2.1.3 Charge Transport Properties: Charge carrier's free mean path should be larger than the detector thickness [8] in order for all photo-generated careers to be collected at the electrode thereby avoiding incomplete charge collection. Carrier mean free path is the product of mobility, electric field and lifetime. Carrier lifetime has been measured by transient charge techniques. [9]. Time of flight measurements were used to measure charge carrier mobilities. [10,11]. It should be noted that values of charge mobilities can be affected by impurity levels.

Mobility-lifetime product is a fundamental figure of merit for semiconductor x-ray and gamma ray detectors and is usually measured by fitting the photopeak shift as a function of applied bias in the Hecht equation. [10]. Electron and hole mobility-lifetime products have been reported to be 6–8 x 10^{-4}cm^2/V and 3 x 10^{-5}– 3 x 10^{-6} cm^2/V respectively. [9, 11-15]. Improvement in crystal purity and crystallinity show improvement in the carrier lifetimes. However hole lifetimes need to either be increased or compensated for by electronics to further improve the detection ability of CZT detectors.

Deep impurities occupy substitution lattice positions and introduce energy levels near the middle of band gap. They can act as traps for charge carriers by immobilizing a hole or electron. They can also act as recombination centers by capturing electrons and holes and causing them to annihilate. Trapping and recombination contribute to loss of charge carriers and hence reduce average lifetime of carriers. Structural defects such as point defects (vacancies and interstitials that behave as acceptors and donors respectively) and line defects or dislocations produced in stressed crystals within the crystal lattice can also lead to trapping and charge carrier loss.

2.2 CZT crystal growth and detector fabrication

2.2.1 Crystal growth: The phase diagram of CdTe-ZnTe consists of an upper liquidus and a lower solidus curve as shown in figure 2.2 below. The melting points of the two pure components determine the end points of the curves. CdTe and ZnTe form a solid solution throughout the alloy range. For CZT crystals grown from the melt, the first solids formed from the melt will contain more zinc than the average melt content according to the phase diagram. The Zn variation has been shown to vary according to sample location in the ingot [16] due to the segregation coefficient of zinc which is 1.3. The commercially available starting materials are greater than 6N pure, but for nuclear detectors, purer starting materials are desired.

The materials are separately pre-synthesized due to the difference in vapor pressure between cadmium and tellurium. CZT crystals are best grown from the melt as the melt mixes the elements; however there is problem of thermal dissociation pressure at the melting point that causes cadmium to evaporate at a higher rate than tellurium resulting in non-stoichiometry and precipitation of tellurium in the crystal. [16]. Cadmium vacancies have been compensated by doping CdTe with group III elements such as In and Al. [17].

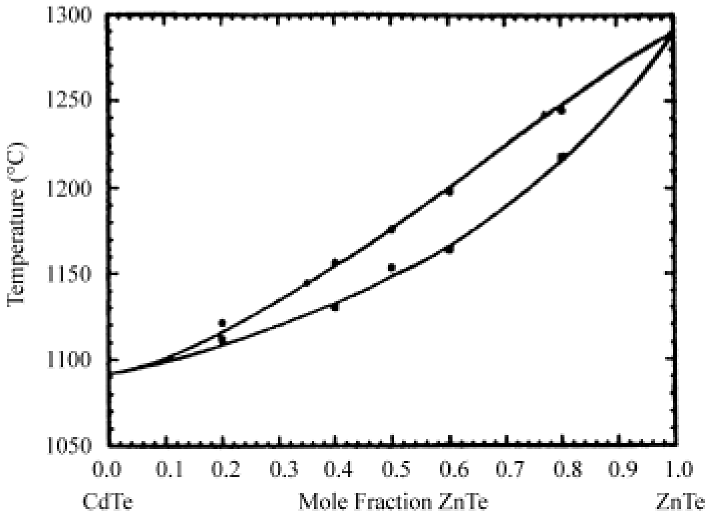

Figure 2.2 Calculated solidus (upper) and liquidus (lower) lines in CdTe-ZnTe pseudo-binary system. Dots represent experimental points. [16]

Growth methods include the Bridgman method [18-20] which has variations as horizontal and vertical Bridgman method, high pressure Bridgman [21-24] and low pressure Bridgman [25-27], Physical Vapor Transport method, [28-30] and traveling heater method (THM) [31]. Most of the defects affecting CZT nuclear detectors results in crystal growth, and for this reason a brief review of the growth techniques is given below.

Bridgman growth is a controlled freezing process occurring at the liquid-solid equilibrium condition. Growth occurs under a temperature gradient with the aim of producing a single nucleus from which a single crystal will propagate and grow. In Bridgman growth the elemental materials are mixed into a sealed ampoule, and the contents melted and cooled to solidify into a crystalline form by allowing the solid-liquid to move slowly until the whole molten charge is solidified.

Different modifications to Bridgman method include High Pressure Bridgman (HPB) and Low pressure Bridgman (LPB). HPB involves maintaining a high pressure of an inert gas over the melt in order to reduce the loss of cadmium in the molten materials. In LPB, CZT crystal is grown without the use of high gas pressure. LPB can be achieved either in the horizontal or vertical configuration.

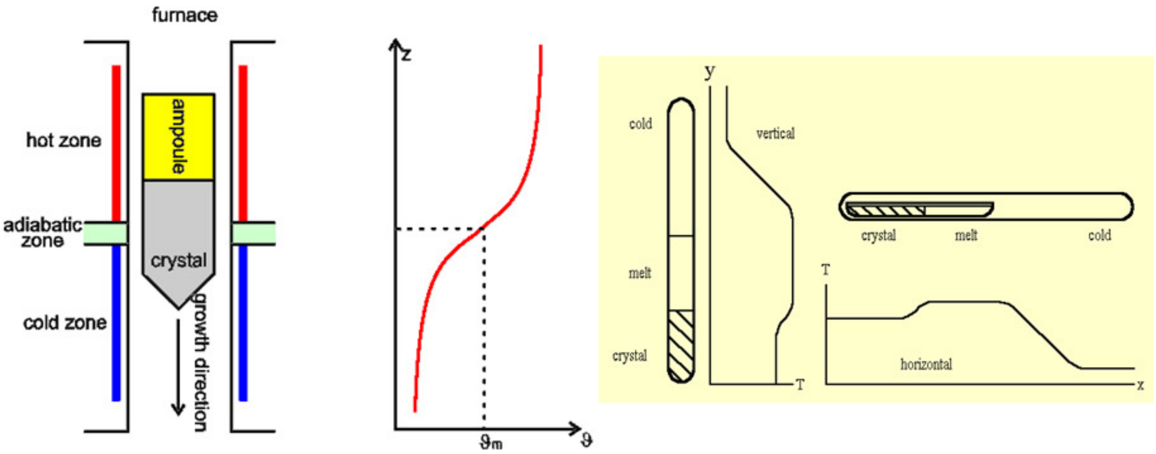

Figure 2.3. Bridgman growth technique a) showing different zones, b) showing horizontal and vertical configurations with temperature profile.

Physical vapor transport (PVT) of crystal growth has advantages such as lower growth temperature and smaller contact area with walls of the ampoule that results in reduction of impurities. Also with PVT it is easier to control the stoichiometry as we demonstrated in earlier works [32-34] where we effectively controlled the segregation coefficient and hence uniformity of grown cadmium sulfo-selenide doped with chromium.

The traveling heater method (THM) is a seeded growth process that operates by precipitation of grown material from a solution. A CZT seed is placed in the growth crucible and molten Te is added as solvent while polycrystalline CZT is added as feed material. The polycrystalline CZT dissolves into molten tellurium. As the traveling heater is moved, CZT crystal precipitates from the tellurium solvent and grows on the CZT seed to form homogenous single grains of CZT crystal.

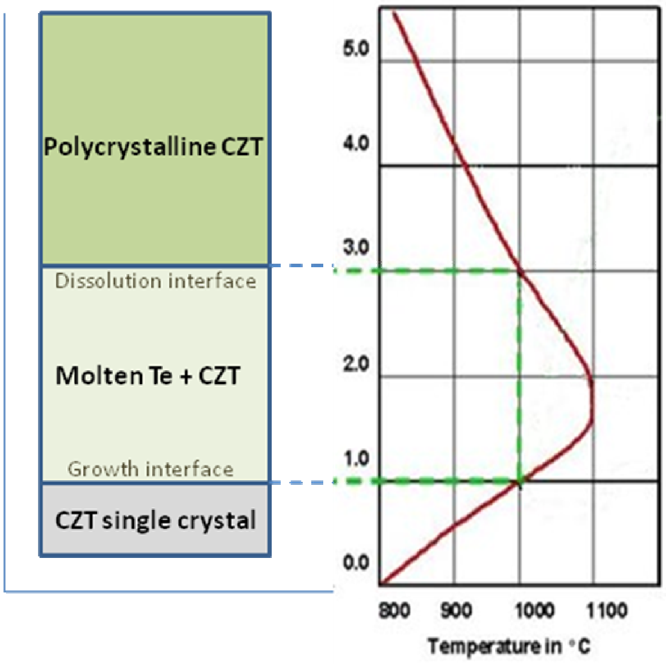

Figure 2.4 Traveling heater method of crystal growth.

2.3 CZT detector fabrication

CZT nuclear detector devices are fabricated by applying metallic contacts on the finely prepared parallel surfaces. The contacts serve as the electrodes, i.e. cathode and anode that collect charges mobilized by an internal electric field due to the applied bias. The three major device configurations for room temperature semiconductor nuclear detector applications are simple planar, co-planar grid and pixellated configurations as shown schematically in fig. 5. Simple planar and co-planar grid configurations are generally used for large-volume single element detectors. Co-planar configurations can be used as electron-only devices to provide higher spectral resolution, especially for higher energy gamma rays, i.e. energy above 50 KeV. Pixellated detectors are used in imaging systems where position information is obtained in signals from individual pixels. Photolithography is used to design complex electrode structures such as co-planar and pixellated electrodes.

Other configurations include the small-pixel-effect and the capacitive Frisch-grid configurations.

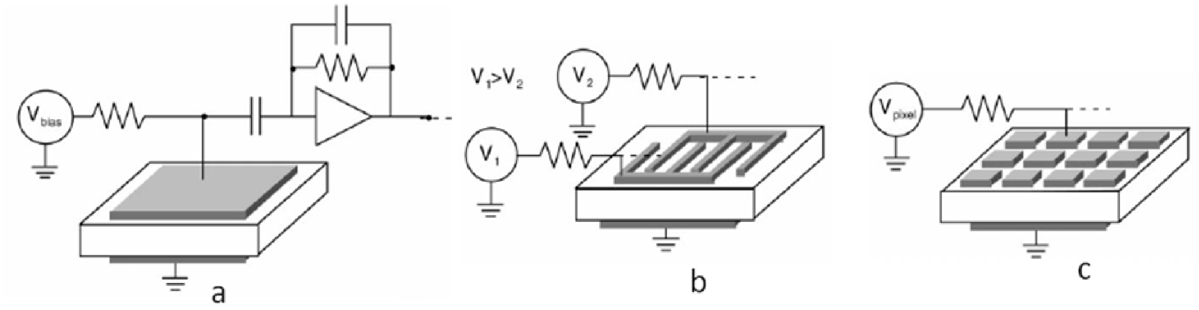

Fig. 2.5 Schematics of three major nuclear detector geometries: (a) planar detector; (b) co-planar grid detector; (c) pixellated detector.

2.4 CZT Device operation

Operation of CZT nuclear detector is based on the interaction between the detector and gamma radiation. An incident photon interacts with the detector material through any of the processes described below, depending on the energy of incident radiation. The interaction produces electron-hole pairs. When a reverse bias is applied to the detector, a depletion region is created which enables sweeping of electrons and holes to the electrodes due to the applied electric field. The time taken to collect the charges reflects the mobility and average distance traveled by charge carriers to reach the collection electrodes. The detector has attached external circuitry at which the resultant pulse from the electron-hole pairs is observed. The magnitude of the pulse is proportional to the energy lost by the incident ionizing radiation. A schematic of this process is shown below.

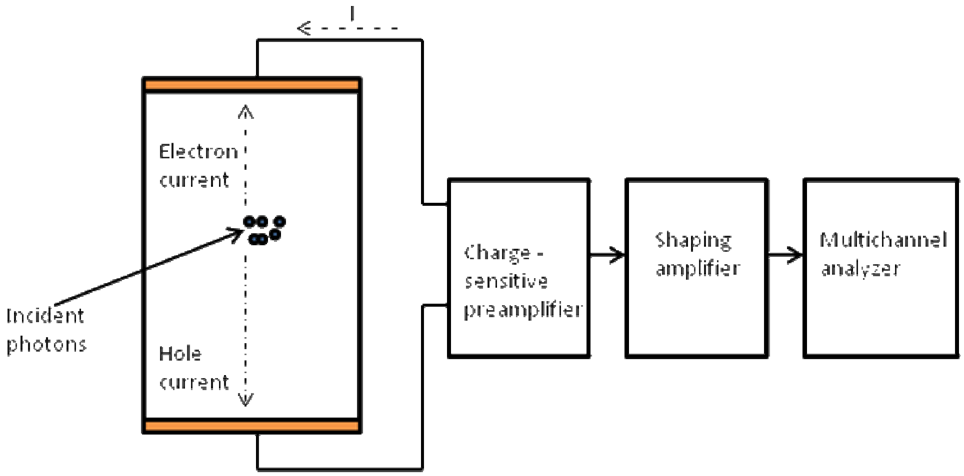

Figure 2.6 Schematics of the operation of a nuclear detector.

2.5 Nuclear Radiation

Radiation refers to energy in the form of waves or sub-atomic particles. Radiation could be either uncharged or charged. Charged radiations, such as beta particles (electrons and positrons), protons, alpha particles and fission fragments, are also known as ionizing radiation because they transfer energy to orbital electrons during interaction with matter. Uncharged radiations include x-rays, gamma rays and neutrons. Radiation is produced by many processes such as:

1. Relaxation of an excited atom to its ground state either by ionization or by emission of an orbital electron.

2. Spontaneous decay of heavy nucleus to produce alpha particles or fission fragments, or neutrons.

3. Relaxation of an excited nucleus to a lower energy state to emit gamma rays.

Gamma rays can also be emitted from annihilation of electrons or positrons. Gamma rays are the most energetic form of electromagnetic radiation. Alpha particles typically have energy from ~3 to 7 MeV. Slow neutrons have energies ~0.025 eV while fast neutrons have 10 keV to 15 MeV. Electron energies on the other hand range from a few keV to 100 MeV.

2.6 Radiation detection

For radiation to be detected, it must first undergo interaction with the medium. The methods of gamma ray and x-ray interactions are photoelectric absorption, Compton scattering and pair production.

2.6.1 Photoelectric absorption: In photoelectric absorption, all of the energy of an incident photon is absorbed by one of the orbital electrons of the atoms in the detector material. This photoelectron has a kinetic energy equal to incident photon energy minus atomic binding energy of the electron. The most probable origin of ejected photoelectron is the most tightly bound or the K shell of the atom. The photoelectron then loses its kinetic energy by Coulomb interactions with the semiconductor lattice thereby creating many electron-hole pairs. The number of electron-hole pairs created is a simple function of the energy of the incident photon.

$$E_{e^-} = hv - E_b \qquad \text{.................. (4)}$$

E_{e-} is the energy of photoelectron, *hv* is the incident photon energy and E_b is the binding energy of the electron in the original shell.

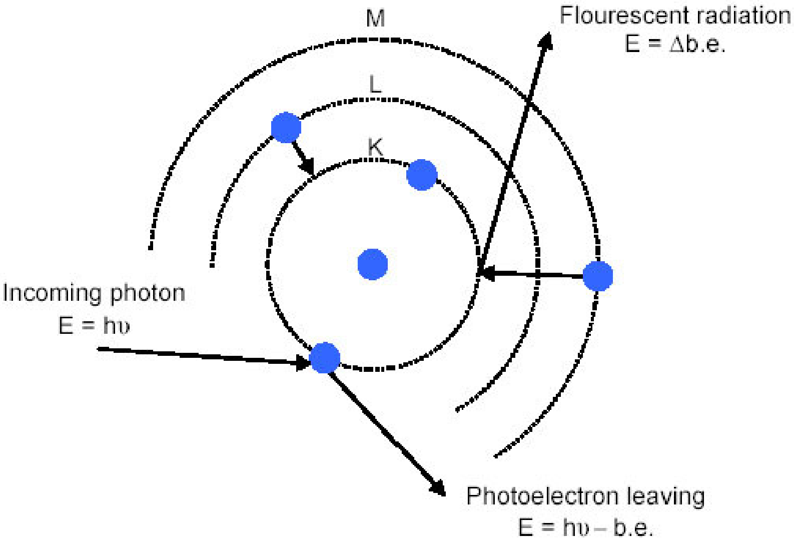

Figure 2.7 Schematic of photoelectric absorption

Some characteristic x-ray photons may be generated and reabsorbed by photoelectric absorption with less tightly-bound shell. Photoelectric absorption is the predominant mode of interaction for gamma and x-rays. The photoelectron process is enhanced for materials with high atomic number Z. Probability, τ, of photoelectric absorption per atom over all ranges of energy ($E_γ$) and atomic number (Z) is roughly approximated as

$$\tau = const * \frac{Z^n}{E_\gamma^{3.5}} \quad \text{.......... (5)}$$

where exponent n varies between 4 and 5 over the energy region of interest. Equation 5 shows the dependence of the probablility of photoelectric absorption on the atomic number of the absorbing material.

2.6.2 Compton scattering: This is the predominant interaction mechanism for gamma ray energies typical of radioisotope sources. An incoming photon collides with an orbital electron. The direction and energy of the incident photon is altered. The incident photon transfers some of its energy to the orbital electron. This electron then loses its energy through creation of electron-hole pairs. Energy transfers are determined from the conservation of energy and momentum during collision.

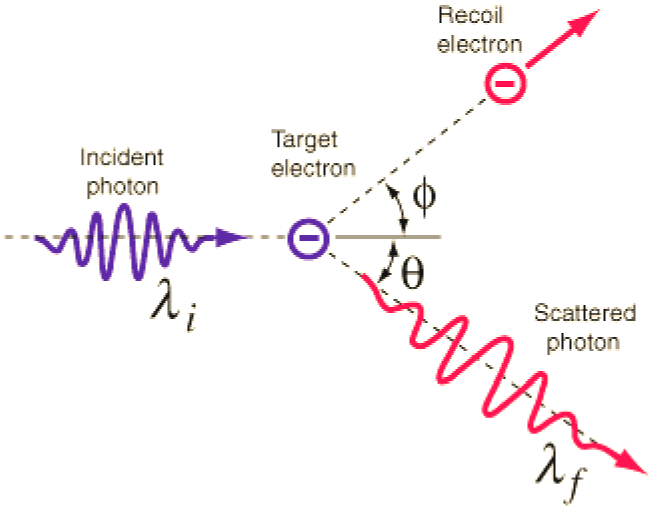

Figure 2.8 Schematic of Compton scattering

2.6.3 Pair Production: An incident photon with energy above 1.02 MeV may create an electron-positron pair. Any excess energy can go into kinetic energy of the electron or positron. The positron has a very short lifetime in the material and so will annihilate with an electron in the material to produce two annihilation photons of energy 0.511 MeV. The annihilation photons then interact with atoms of the material to create electron-hole pairs.

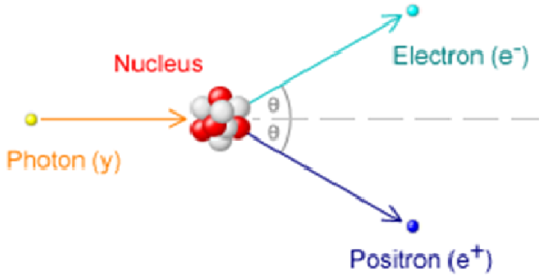

Figure 2.9 Schematic of pair production process

2.7 Operational Characteristics of Semiconductors

2.7.1 Band Structure: Electrons are confined to energy bands in crystalline solids. The valence band is the lower band, corresponding to electrons bound to specific lattice sites within the crystal that constitute inter-atomic forces within the crystal. Conduction bands are next higher bands. Electrons in the conduction band are free to move throughout the crystal and thereby contribute to electrical conductivity of a material. The two bands are separated by the band gap. The number of electrons within a crystal is just enough to fill the valence band completely, so that without thermal excitation, insulators and semiconductors have the same configuration of completely filled valence band and completely empty conduction band and so there is no conductivity.

In metals the highest occupied energy band is not completely full so electrons can migrate throughout the material as small incremental energy is needed to be above occupied states. In insulators and semiconductors, electrons must first cross the Bandgap to reach the conduction band, so conductivity is many orders of magnitude lower.

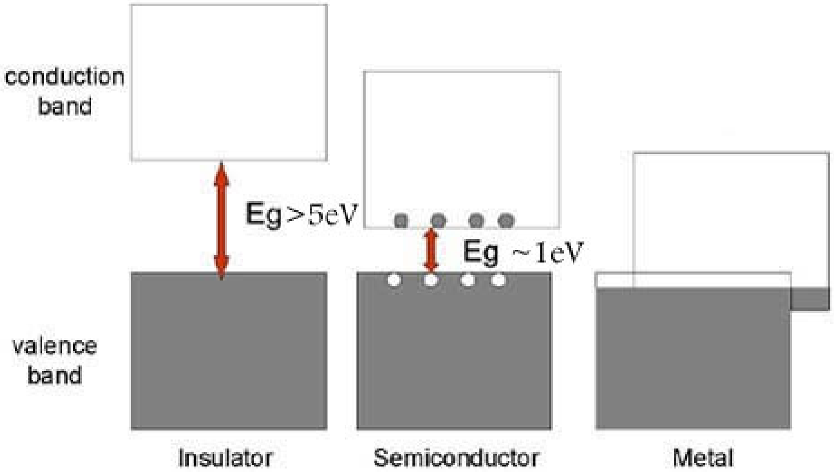

Figure 2.10 Band structure for electron energies in materials.

2.7.2 Charge Carriers: At non-zero temperature, valence electrons can gain sufficient thermal energy to move across the band gap to the conduction band leaving behind a vacancy called hole. Electron – hole pairs are the charge carriers and form the solid state analogy of ion pair in gases. Electron hole mobility contributes to observed conductivity of a material.

Probability, P(T), per unit time that e – h pair is thermally generated is given by

$$P(T) = CT^{3/4} \exp(-\frac{E_g}{2kT}) \quad \text{.................. (6)}$$

where T is the absolute temperature, E_g is bandgap energy, k is Boltzmann constant, and C is proportionality constant characteristic of material. Materials with very large E_g will have low P(T) and show low electrical conductivity as insulators.

Electrons and holes undergo a net migration due to an applied electric field. Electrons are drawn preferentially in opposite direction to the electric field vector while holes move in the same direction as the electric field.

$$\begin{aligned} \upsilon_h &= \mu_h \xi \\ \upsilon_e &= \mu_e \xi \end{aligned} \quad \text{.................. (7)}$$

where μ = mobility, υ = drift velocity (cm/s), ζ = magnitude of electric field. Mobilities of electrons and holes are of the same order. Saturated drift velocity is ~ 10^7 cm/s hence for a thickness of 0.1 cm it takes ~ 10 ns to collect the carriers. This makes semiconductor detectors one of the fastest responding radiation detectors.

2.7.3 Impurities and dopants: Intrinsic semiconductors have equal numbers of electrons in conduction band as holes in valence band. It can be described in theory but never achieved in reality. Extrinsic semiconductors have impurities or dopants. The extrinsic semiconductors are divided into two groups, n-type and p-type semiconductors.

N-type semiconductors are also known as donor impurities as they readily contribute electrons to conduction band. The extra electrons can occupy a position within the normally forbidden gap and have energies near the top of the gap. The added electrons in conduction band increases the rate of recombination and shift the equilibrium between electrons and holes so that equilibrium concentration of holes is decreased. Charge neutrality is maintained by the ionized donor impurities that represent net negative charges that balance the excess electron charges. They differ from holes as they are fixed in the lattice. N-type semiconductor create more conduction electrons and less holes than intrinsic semiconductors, and electrical conduction is determined mainly by the flow of electrons, which are the majority carriers hence holes are the minority carriers and play a very small role in conduction.

P-type semiconductors create an unsaturated covalent bond representing a hole in the lattice. An electron that fills the hole is less tightly attached than a valence electron, so the acceptor sites also create electron sites within the normally forbidden energy gap. The acceptor sites lie near the bottom of energy band. Both donors and acceptors are shallow impurities.

2.7.4 Trapping and recombination: Deep impurities are impurities that occupy substitution lattice positions that introduce energy levels near the middle of band gap. They can act as traps for charge carriers by immobilizing a hole or electron. They can also act as recombination centers by capturing electrons and holes and causing them to annihilate. Trapping and recombination contribute to loss of charge carriers hence reduce average lifetime of detectors. Structural defects within the crystal lattice can lead to trapping and charge carrier loss. These defects include point defects (vacancies and interstitials that behave as acceptors and donors respectively) and line defects or dislocations produced in stressed crystals.

The ionization energy, ε is the average energy expended by the primary charged particle to produce one electron hole pair. ε is independent of energy and type of incident radiation. ε for silicon or germanium is ~ 3 eV compared to 30 eV required to produce an ion in gas-filled detectors, so the number of charge carriers is 10 times greater. This gives better signal to noise ratio. Ionization energy increases with decreasing temperature.

2.7.5 Electrical contacts: Contacts are used to collect the electric charges created by radiation at either boundary. An ohmic contact is a non rectifying electrode through which charges of either spin can flow freely. Ohmic contacts have very high steady-state leakage currents and so cannot be used in semiconductor detector applications.

2.7.6 Leakage current: This originates both from the bulk volume and surface of the detector. A source of leakage current is minority carriers that are transferred through the junction. Another source is thermal generation of electron-hole pairs within the depletion region. The rate of thermal generation of electron hole pairs within the depletion region increases with volume of the region and is reduced only by cooling. High bandgap semiconductors will have low rate of thermal generation of electron-hole pairs.

Generally, leakage current must not exceed 10^{-9} A in high energy applications and 10^{-10} A for soft x-ray applications to avoid significant resolution degradation as higher levels of surface leakage can be more significant than bulk leakage. Iwanczyk et al [35] determined that leakage current of 10^{-11} – 10^{-10} A permits room temperature energy resolution as high as 350 eV for 0.5 mm thick and 3 mm^2 detectors. It is important to avoid surface contamination that can create leakage paths during processing. Grooves, guard rings and surface passivation are introduced in different configurations to reduce surface leakage current. The long term behavior of leakage current is a useful monitor of degree of radiation damage suffered by a detector when used under conditions in which radiation damage is significant.

2.7.7 Reverse biasing: A contact potential of ~1V formed across an unbiased junction is too small to generate large enough electric field to make charge carriers move rapidly, hence incomplete charge collection exists as charges will be lost by trapping and recombination.

An unbiased junction has a very small depletion region and high capacitance. This causes poor noise properties so that unbiased junction cannot be used as detectors but rather an external circuit is applied in a reverse biased direction.

P-n junction will conduct current when biased in forward direction but little conduction when biased in reverse direction. The majority carriers on the p-side are electrons while the majority carriers on the n-side are holes; therefore conductivity through the junction is enhanced. If p side is made negative with respect to n-side, the junction is reverse biased. The natural potential difference from one side of the detector to the other is enhanced. The minority carriers are attracted across the junction and the reverse current is very small.

When a reverse bias is applied to junction, the resistivity of the depletion region is much higher than that of normal n and p type material. The thickness of depletion is increased thereby increasing the volume for collection of radiation produced charge carriers.

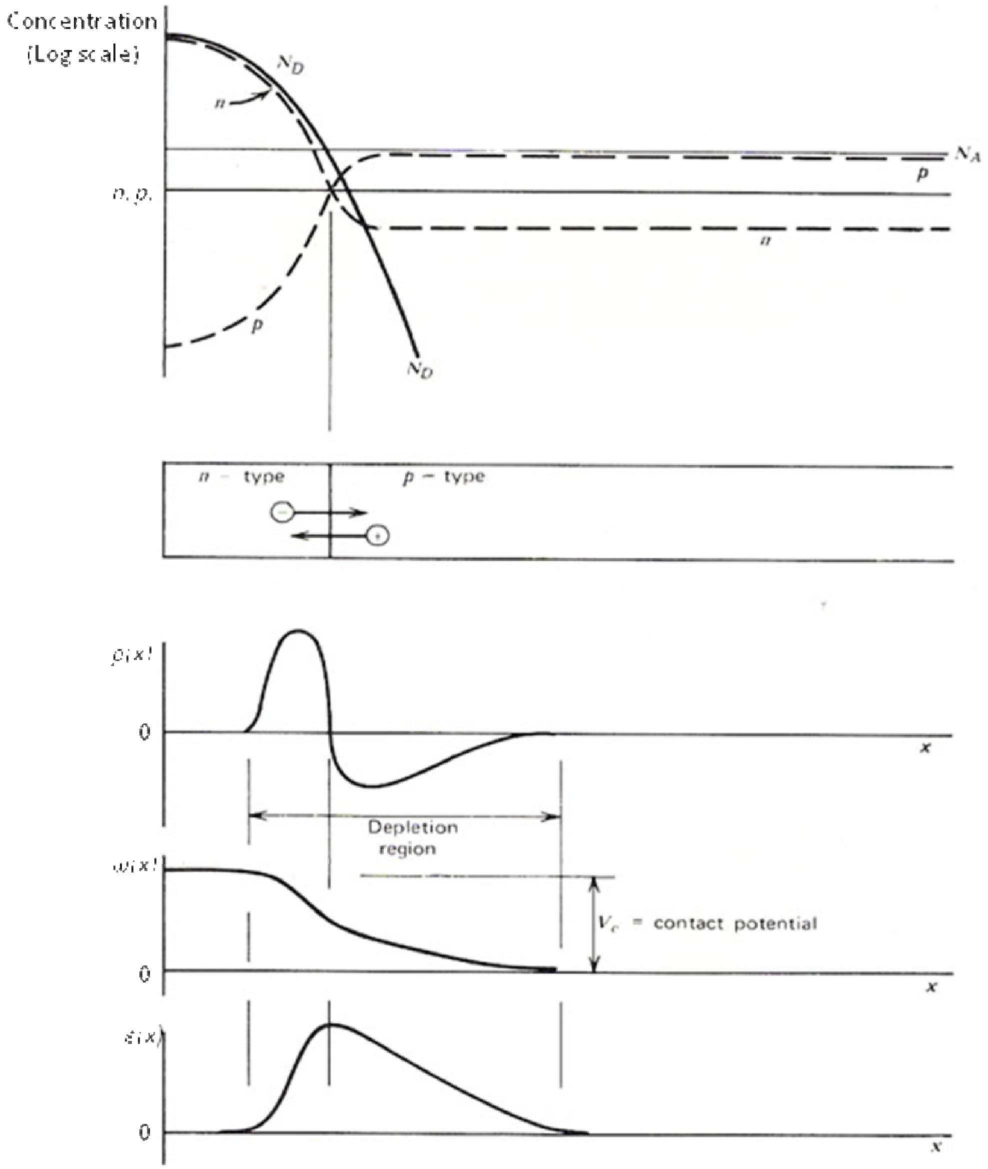

Figure 2.11 Concentration profiles for n-p junction. [5]

The resistivity of the material should be as high as possible to give the largest depletion width possible for a given applied voltage. Resistivity is limited by purity of semiconductor material before doping as enough dopant must be added to override the non uniform effects of residual impurities. For this reason we want to obtain CZT crystals fabricated from highest purity materials possible.

Good energy resolution is obtained by using the largest possible applied voltage up to the point that the detector becomes fully depleted. Maximum electric field occurs at the point of transition between n and p-type material.

$$\varepsilon_{\max} \cong \frac{2V}{d} = \left(\frac{2VNe}{\mathrm{E}}\right)^{\frac{1}{2}} \quad \text{..............} \; (8)$$

Maximum operating voltage must be kept below breakdown voltage to avoid a destruction of detector properties. Reverse biased p-n junction makes an attractive radiation detector because charge carriers created within the depletion region is quickly and efficiently collected.

REFERENCES

1. K. Zanio, Willardson, Beer, Teatise (Eds.), Cadmium Telluride, Semiconductors and Semimetals, Vol. 13, Academic Press, San Diego, 1978, p. 53.
2. G. A. Baraff, Joel A. Appelbaum, and D. R. Hamann. Phys. Rev. Lett. 38, 1977, pp 237 – 240.
3. T. E. Schlesinger et al, Mat. Sci and Eng. 32, 2001, pp. 103
4. L. Vegard, Z. Phys. 5 (1921) 17
5. N. Motta, A. Balzarotti, P. Letardi, A. Kisiel, M.T. Czyzyk, M. Zimnal-Starnawska, M. Podgorny, J. Cryst. Growth, 72 (1985) 205.
6. M.S. Goorsky, H. Yoon, M. Schieber, R.B. James, D.S. McGregor, M. Natarajan, Nucl. Instrum. Methods A 3806 (1996) 6.
7. J.F. Butler, B. Apotovsky, A. Niemela, H. Sipila, Proceedings of the SPIE, Vol. 2009, SPIE, Bellingham, WA, 1993, p. 121.
8. G.F. Knoll, D.S. McGregor (1993), In Semiconductors for Room Temperature Radiation Detector Applications 302, 3, ed. R.B. James, T.E. Schlesinger, P. Siffert, L. Franks. Materials Research Society, Pittsburgh.
9. C.J. Johnson, E.E. Eissler, S.E. Cameron, Y. Kong, S. Fan, S. Jovanovic, K.G. Lynn (1993). In Semiconductors for Room Temperature Radiation Detector Applications 303 ed. R.B. James, T.E. Schlesinger, P. Siffert, L. Franks. Materials Research Society, Pittsburgh.

10. Z. Burshtein, H.N. Jayatirtha, A. Burger, J.F. Butler, B. Apotovsky, F.P. Doty. Appl. Phys. Lett. 63 (1993) 102.
11. P. Siffert, Nucl. Instru. Meth. 216, 259 (1983)
12. R.C. Whited, M.M. Schieber Nucl. Instru. Meth 162, 113
13. E. Sakai Nucl. Instru. Meth 196, 121
14. H. Ohmori, Y. Iwase, R. Ohno, Mat. Sci. and Eng. 1993, B16, 283
15. J.F. Butler, B. Apotovsky, L. Lajzerowicz, L. Verger, Mat. Sci. and Eng. 1993b, B16, 291
16. T.E. Schlesinger et al. Materials Science and Engineering 32 (2001). (Reports, a review journal), pp. 103,189
17. F.A. Kroger, Phys. Stat. Sol. (a) 29 (1975) 465.
18. P. Cheuvart, U. El-Hanani, D. Schneider, R. Triboulet, J. Cryst. Growth 101 (1990) 270.
19. M. Bruder, H. Schwarz, R. Schmitt, H. Maier, J. Cryst. Growth 101 (1990) 266.
20. H.L. Glass, A.J. Socha, C.L. Parfeniuk, D.W. Bakken, J. Cryst. Growth 184/185 (1998).
21. C. Szeles, E.E. Eissler, MRS Symp. Proc. 487 (1998) 3.
22. E. Raiskin, J. Butler, IEEE Trans. Nucl. Sci. 35 (1988) 81.
23. J.F. Butler, F.P. Doty, C. Lingren, Proc. SPIE Ð Int. Soc. Opt. Eng. 1734 (1992) 131.
24. F.P. Doty, J.F. Butler, J.F. Schetzina, K.A. Bowers, J. Vac. Sci. Technol. B 10 (1992) 1418.

25. K. Lynn, M. Weber, H. Glass, J. Flint, C. Szeles, Mater. Res. Soc. Symp. 487 (1998) 229.
26. K. Chattopadhyay, H. Chen, K.-T. Chen, A. Burger, J.P. Flint, H.L. Glass, R.B. James, Mater. Res. Soc. Proc. 487 (1998) 123.
27. T.E. Schlesinger, B. Brunett, H. Yao, J. Van Scyoc, R.B. James, S. Egarievwe, K. Chattopadhyay, X. Ma, A. Burger, N. Giles, U. El-Hanany, A. Shahar, A. Tsigelman, J. Electron. Mater. 28 (1999) 864.
28. W. Palosz, K. Grasza, D. Gilles, G. Jerman, J. Cryst. Growth 169 (1996) 20.
29. A. Szczerbakow, J. Domagala, D. Rose, K. Durose, V. Ivanov, A. Omeltchouk, J. Cryst. Growth 191 (1998) 673.
30. L. Ben-Dor, J. Cryst. Growth 71 (1985) 519. M. Fiederle, T. Feltgen, J. Meinhardt, M. Rogalla, K.W. Benz, J. Cryst. Growth 197 (1999) 635.
31. L. Chibani, M. Hage-Ali, J.P. Stoquert, J.M. Koebel, P. Siffert, Mater. Sci. Eng. B16 (1993) 202.
32. O.S. Babalola, Growth and Characterization of Cr^{2+}:CdSSe crystals, Masters Thesis, Fisk University, Nashville, TN, 2004.
33. U.N. Roy, O.S. Babalola, J.Jones, Y. Cui, T. Mounts, A. Zavalin, S. Morgan and A. Burger: J. Elect. Mater. Vol. 34 no.1, 2005, pp 19.
34. U.N. Roy, O.S. Babalola, Y. Cui, T. Mounts, A. Zavalin, S. Morgan and A. Burger. J. Crys. Gr. 265, Issues 3-4, 1, 2004, pp 453.
35. Iwanczyk, J. Z Nucl. Instr. And Meth. A283 , (1989) pp. 208.
36. G. F. Knoll, Radiation Detection and Measurement 2nd edition, 1989 pp. 52

Part Two

Original studies

CHAPTER III

STUDIES OF SURFACE CONDITION

Overview

Surface processing determines, to a large extent, the performance of crystals used for nuclear detectors. Up until recently only uncollimated sources of radiation were available for studying detector crystals for both surface and bulk effects. However the development of National Synchrotron Light source (NSLS) at Brookhaven National Laboratory (BNL) provides us, for the first time, with the ability to scan nuclear detector crystals with very high spatial resolution synchrotron radiation. The tunable energy range of the monochromatic x-ray radiation enables us to scan the surface of detectors and study surface effects. This chapter shows how surface roughness, studied by micro-scale x-ray scan from NSLS, directly affects detector performance in terms of charge collection. The difference in response of CZT nuclear detector when irradiating the rough surface as anode and cathode are also shown and explained. A model is used to explain charge collection behavior on rough anode and cathode surfaces using Ramo's theory. [1]. The results show that rough surfaces contain trapping centers that enhance leakage current and distorts the signal.

Many of the findings from this study have been published in Journal of Electronic Materials. [2]

3.1 Motivation

Surface processing plays an important role in determining the performance of nuclear detectors. Surface processing affects detector's leakage current [3] which in turn affects the pulse height resolution of the detector [4-10]. The maximum voltage that can be applied to a detector is limited by the conductivity of the detector surface, which depends on surface processing. During the process of the CZT detector fabrication, mechanical polishing and chemical etching always induce surface damage and non-stoichiometry of detector surface. Dangling bonds, surface roughness and non-stoichiometric surface species produce the defects responsible for high surface leakage current. Surface properties also influence the electric field and affect charge transport, signal generation and signal collection[10-13]. For these reasons it is important to study CZT surface processing to obtain an optimal surface condition that would result in high-quality radiation detectors.

Prior to contact deposition to fabricate a nuclear detector, the surfaces are prepared by polishing to remove the damaged layer induced during cutting. The main steps involved are successively polishing with silicon carbide (SiC) paper of decreasing grit size followed by final polishing with alumina slurry of 0.01 μm. The crystals are then etched usually with 0.5-10% Bromine-methanol solution at room temperature followed by rinsing with methanol solution to produce a fine optically flat and damage-free surface. Deviations from the standard procedure have been shown to have notable effects on dark currents [14, 15]. To fully understand these effects, it is necessary to study the effect of surface roughness on detector performance, and this is the main focus of this chapter.

Polishing-related defects tend to be evenly distributed over the entire surface and are believed to act as trapping centers. X-ray photons generate charges near the cathode that drift toward the respective electrodes. Holes are swept away quickly to the cathode and make virtually no contribution to the output signal, while electrons travel all the way to the anode before being collected. A fraction of electrons generated near a rough cathode surface encounter the defects caused by the roughness during their drift toward the anode, which distorts the signal and enhances the leakage current. In contrast, when the rough surface acts as an anode, the electrons generated near the smooth cathode surface drift all the way unhindered to the anode before being collected. Though a fraction of the electrons may impinge upon the rough anode surface, eventually most of them will contribute to the signal response. Therefore, a rough surface is likely to yield a dissimilar response when alternatively probing as an anode or a cathode. Furthermore, drifted electrons experience diffusion along their way which causes broadening of the electron cloud [16] and can overwhelm the effects of localized surface defects at the anode region thereby producing poor-resolution images of the defects.

In this work, we systematically studied the effects of surface roughness conditions on carrier transport and signal generation to identify the optimal processing methods required to yield high quality radiation detectors using a micro-scale X-ray mapping technique employing a synchrotron beam from National Synchrotron Light Source (NSLS) at BNL. The micro-scale characterization at low X-ray energies provides the ability to reveal fine details of surface properties and spatial response [17-20] in semiconductor detectors.

3.2 Experiment

A 5 x 5 x 2 mm^3 nuclear detector grade CZT crystal in planar configuration was finely polished following the procedure described above. Electroless gold contact from gold chloride ($AuCl_3$) solution was deposited on one side of the planar detector, while the other side was processed with different surface preparations as follows:

a) The surface was polished first with 0.05 µm grit alumina powder and 1 µm, 3 µm, and 5 µm grit Al_2O_3 abrasive papers to obtain various degrees of surface roughness.

b) The surface was scratched with a diamond-tipped cutter to create 20 µm wide and 30 µm deep scratches in specific areas on top of the 1 µm grit polished surface.

c) The surface was prepared with two different roughnesses; one-half of it was polished by 0.05 µm grit and the other half by 3 µm grit abrasive paper.

d) The surface was prepared as in c) above with 0.05 µm and 3 µm grit abrasive paper and then etched with 2% and 5% Bromine Methanol solution.

For each surface condition, a gold contact was deposited and the surface was scanned with micro scale x-ray beam from NSLS. The surfaces were then re-polished, and the next surface preparation was conducted.

Each gold contact deposition on the surface of the crystal was done by the electroless contact deposition technique, in which $AuCl_3$ solution was carefully spread on the detector's surface by a special pipette to avoid its spilling over the side surfaces. After about 30 seconds, the detector was dipped into deionized water to wash out the excess solution and then blow-dried with pressurized nitrogen gas. For each surface preparation, the X-ray scan was conducted as follows: The detector was mounted on a standard eV Product's brass holder in which a gold-plated spring contact held the detector against a beryllium window. The detector's surface against the beryllium window always acts as a cathode and scans by irradiating the collimated X-ray beam from this end. The beam's size was reduced to 10 μm x 10 μm with a tungsten collimator. The whole device was put on a set of x-y translation stages of submicron resolution. A spec user interface (a UNIX-based software package developed for X-ray diffraction) controlled the motors and data-acquisition system. For each point of the raster scan, a pulse height spectrum, corresponding to the area of the detector irradiated at the cathode side, was recorded through a multichannel analyzer and stored for further processing.

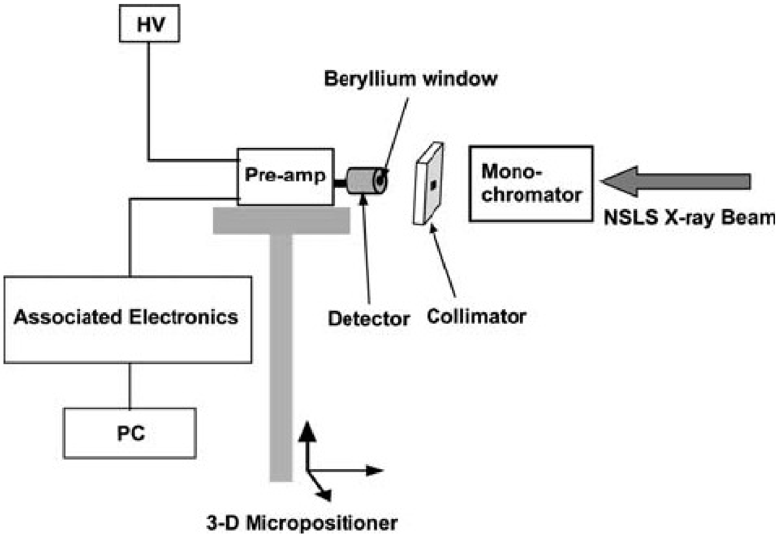

Figure 3.1 Schematic diagram of x-ray scanning experimental setup.

3.3 Results and discussion

3.3.1 Micro-characterization of surface roughness: Using the x-ray scan technique described above, 2-dimensional x-ray images of CZT crystal surfaces with smooth polishing, 1-μm grit and 3-μm grit abrasive paper polishing are generated as shown in Figure 2. The 2 x 2 mm^2 area of CZT surface was irradiated and scanned from the cathode side with a highly stable 20 keV x-ray beam of spatial resolution 10 μm from the synchrotron source. For each scanned spot on the crystal, the position of the corresponding peak was used to generate a 2-D performance map by measuring the shift in energy to the left of the spectrum.

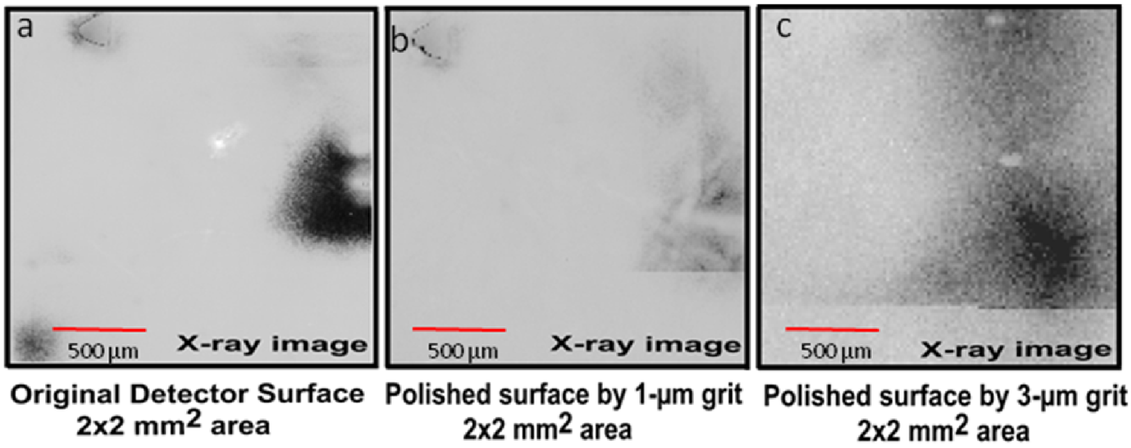

Figure 3.2 X-ray scanned images of a 2x2 mm^2 CZT detector surface with a) smooth polishing, b) 1μm grit and c) 3μm polished surfaces. Non uniform surface defects are apparent in near-surface region of all images.

The x-ray scanned images reveal non-uniform defects in the near-surface region. Polishing grits are known to create a roughness about 10 times their size [21], so that the range of the defects extend from about 5-to 50-μm from the surface, and about 90% of 20-keV x-ray photons are stopped in the CZT material at around 200-micron depth, [22] which is well away from the surface defects created by the grits. Most photon interactions occur below the induced surface defects and explain why the defects are not resolved by 20 keV x-ray scans.

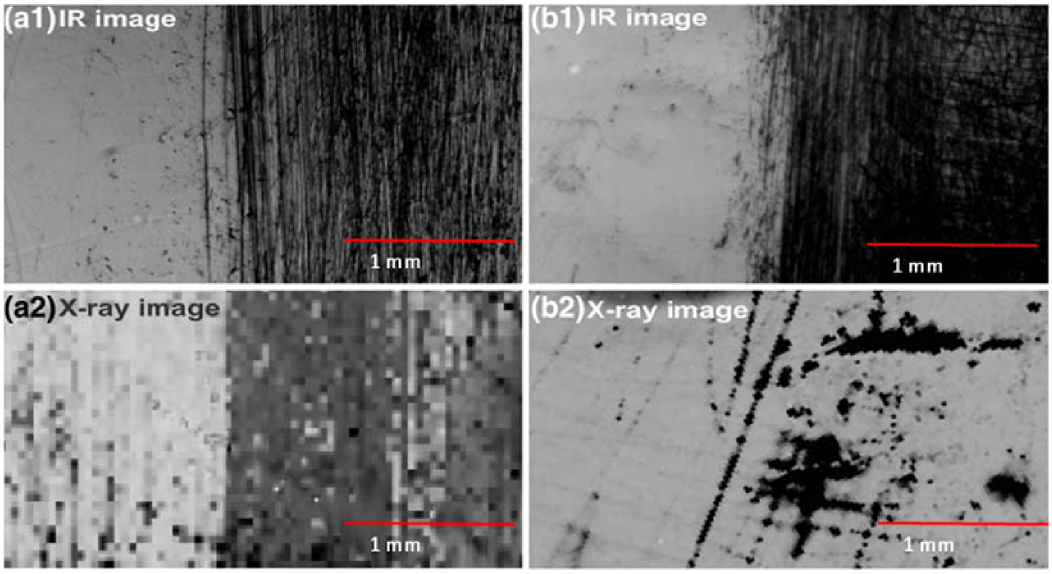

Figure 3.3 Infrared and x-ray images of CZT crystal surfaces with different roughness. a) one-half of surface polished by 0.05 μm and other half by 3 μm grit, scanned with 10 keV x-ray beam, b) one-half of surface polished by 0.05 μm and other half by 5 μm grit scanned with 12 keV x-ray beam. The scanned surfaces are 3.5 mm x 2 mm.

Two 3.5x2 mm^2 dual-grit polished surfaces were scanned by 10 keV and 12 keV x-ray beam at a spatial resolution of 10-μm to observe the effects of the rough and smooth surfaces and the transition effect in the boundary area under identical surface conditions. Fig. 3 shows the microscopic images and the x-ray scan images of both dual-grit polished surfaces.

The 12 keV x-ray beams distinguish effects of the different grits on the surface better than 20 KeV x-ray beams. The near-surface damages are clearly identified. The interesting observation here is the effect of tuning the x-ray energies on the resolution and therefore details of the generated x-ray images. This information could be a potential technique for evaluation of the depth of roughness by using the optimal x-ray energy.

3.3.2 Effect of roughness on leakage current: Although surface polishing is able to remove surface defects, it can induce non-uniform defects on the polished surface that can act as trapping centers and eventually enhance the surface leakage current [23, 24]. Current-voltage measurements of the original surface and surfaces with different roughness were obtained and used to characterize their effects on the detector's properties. The current - voltage plot in Fig. 4 reveals that the leakage current gradually increases with an increase in the surface roughness, indicating an increase in trapping centers with increasing surface roughness.

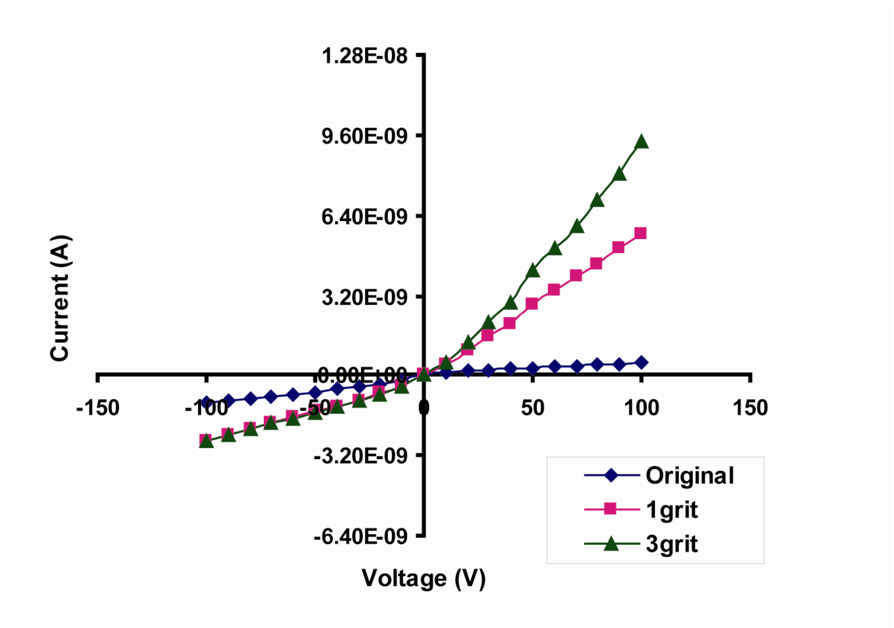

Figure 3.4 I-V measurements of surfaces with different roughness. Original refers to finely polished surface.

As the roughness of the surface increases, fewer carriers are exchanged into the signal, resulting in a degradation of the detector quality. The current-voltage characteristics shown in figure 4 was confirmed with CZT detectors fabricated with guard rings thereby ascertaining the observed leakage to be a direct result of surface modifications and not side effects. Enhanced leakage current can also significantly degrade a device's spectral resolution due to noise, rendering it unusable for gamma-ray spectroscopy.

3.3.3 Effect of surface roughness on leakage current: To understand the effect of surface roughness on surface leakage current, it is important to study the effect of surface states on the metal-semiconductor junction. For isolated metal and isolated semiconductor, no surface states occur and both materials are neutral.

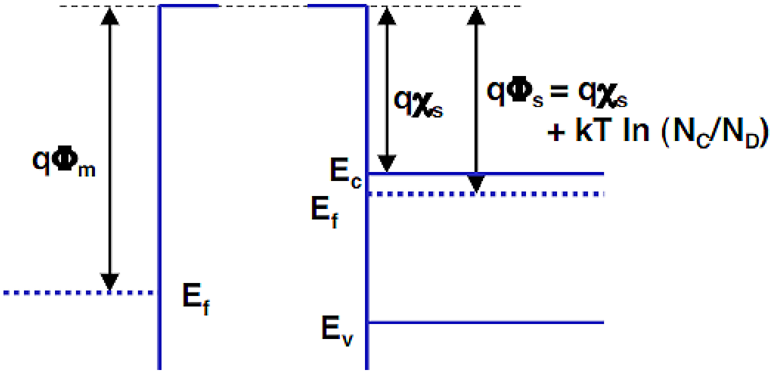

Figure 3.5 Energy band diagram for separated metal and semiconductor.

However, when the metal and semiconductor are brought together, a constant Fermi level is imposed throughout. A junction is formed and electrons flow from the semiconductor to metal until Fermi levels are the same. The semiconductor surface is depleted, and the depletion region grows as the distance between the metal and semiconductor decreases to zero.

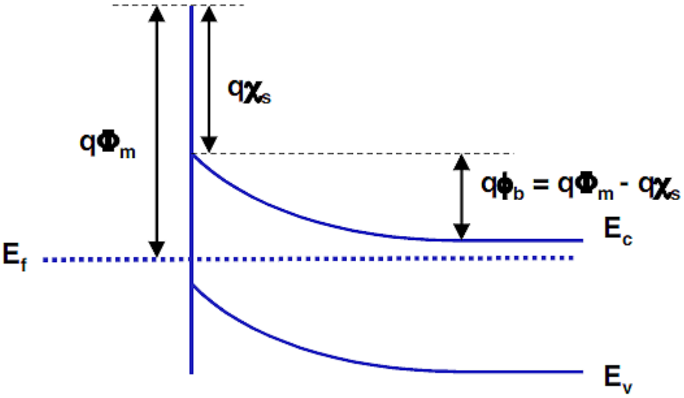

Figure 3.6 Energy band diagram for an ideal metal semiconductor interface.

However, additional energy states are present on the surface of semiconductors due to the termination of perfectly periodic lattice at the surface with unsatisfied (dangling) bonds at the surface. Freshly prepared surfaces of CZT form native oxides when exposed to ambient air. The difference in roughness of the surface of CZT crystal will determine the amount of oxide formed, as surfaces with more roughness features will have larger surface areas for formation of oxides than smoother surfaces. Interface traps and oxide charges exist when metal contact (usually Au for CZT detectors) is applied on prepared CZT surfaces. Figure 3.7 shows a schematic of the location of the interface and oxide trapped charges, as well as fixed oxide charges. Interface trapped charges Q_{it} are produced by excess Te, excess oxygen and impurities, and are located at the Au-CZT interface with energy states in the CZT-forbidden bandgap. Q_{it} exists within the forbidden gap due to the interruption of periodic lattice structure at the surface of the crystal. Oxide trapped charges Qot can be created by radiation or hot-electron injection. These classifications of charges are based on the work of Brews et al [25]. When a bias is applied to the detector, the tips associated with the surface roughness features can form a sufficiently high electric field to produce hot electrons. The higher field at the rough interface can give rise to field emission, impact ionization or even higher Schottky emission, all of which can result in higher leakage current. Fixed oxide charges are located at or near the interface and are immobile under an applied electric field.

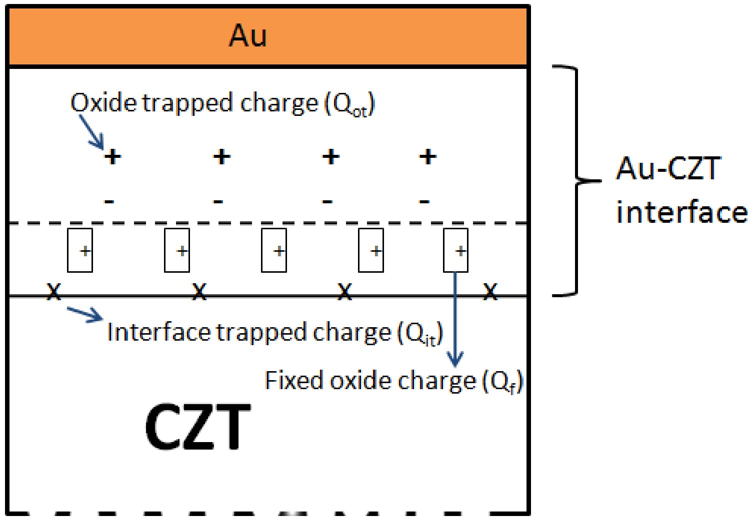

Figure 3.7 Schematic of CZT interfacial charges.

The interface trap density can then be described as

$$D_{it} = \frac{1}{q}\frac{dQ_{it}}{dE} \quad \text{(Number of charges / cm}^2\text{-eV) .... equation 1}$$

where E is the electric field. Q_{it} is expected to be higher for rough surfaces than for smooth surfaces, therefore the interface trap density D_{it} is higher for rougher surfaces under the same applied electric field.

3.3.4 Rough surface as cathode: The following results address some important issues about the effect, position, and size of the defects. Fig. 5a shows the microscopic image of a 2x2 mm^2 area of the detector's surface with intentionally created defects, together with a 2-D map of the same area obtained from raster scans of the sample. The x-ray scans clearly identified the defects that were marked out in the 2-D image. We noted the correlation between the 2-D image and the spectral response (Fig. 3.8b) of the charge collection at different locations on the surface area. In particular, the spectra corresponding to those defects located at marked areas in the x-ray image (Fig. 3.8b) exhibit a significantly lower photo peak and an increased lower energy peak, indicating severe charge losses and large leakage current. The other areas apparently contained no surface defects and show moderate to high charge collection with less noise.

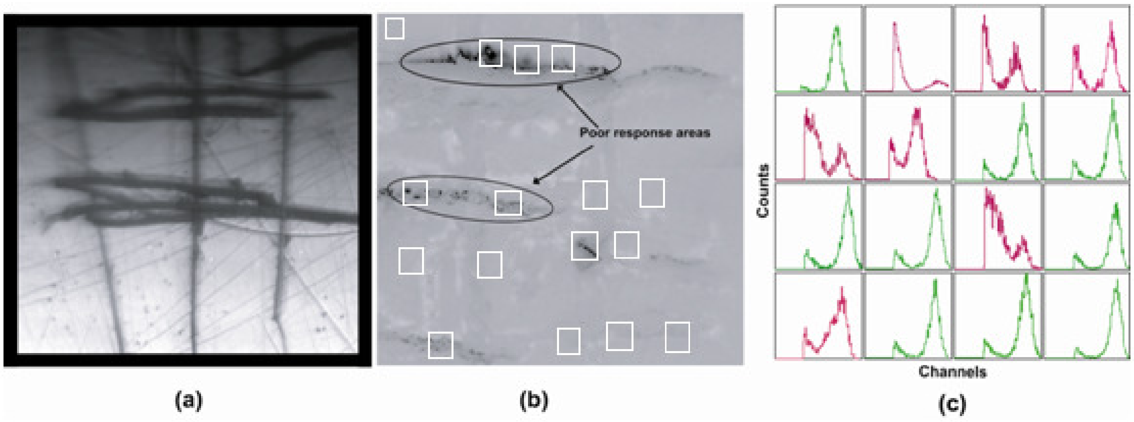

Figure 3.8 IR Image and spectral response of CZT surface with defects (a) a 2x2 mm^2 area of 4X magnified IR image of a polished defective surface; (b) X-ray scanning image of the same area, and, (c) Spectral response in charge collection at arbitrary locations represented as white boxes in (b).

The detector response depends on the position of the generation center and the quantity of charge carriers that survive and reach the respective electrodes. Therefore probing the asymmetric surfaces of electrodes alternatively as an anode and a cathode is likely to yield a different response. In fact, if electrons are generated near rough cathode surface, a certain fraction of them encounter defects due to roughness while they drift toward the anode that results in a distortion of the signal and an enhancement of the leakage current as shown in figure 3.9a.

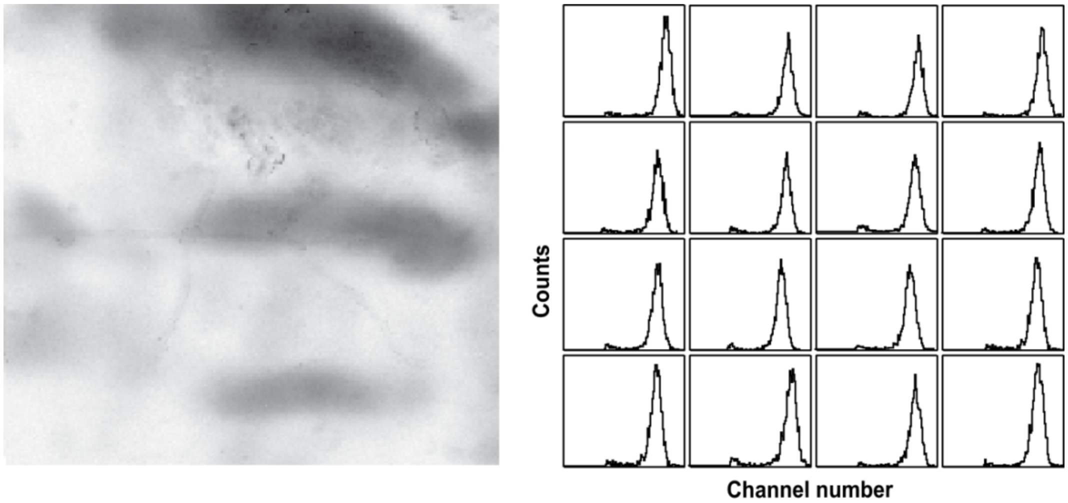

(a) (b)

Figure 3.9 X-ray image and spectral response of a smooth surface (a) a 2x2 mm2 area of X-ray scanning image of a smooth surface while the defect remained on the opposite surface, and (b) Spectral response in charge collection at the various locations on the detector's surface denoted in (a).

Due to the irregularly shaped features, the defects on the rough surface trap and concentrate electrons. These surface electrons cause a reverse current that passes along the surface of the detector causing surface leakage current. Rough detector surfaces have also been shown to result in higher oxide formation and higher Te enrichment, and ultimately increase in surface leakage current [26]. The electrons generated beyond the surface region form a diminished electron cloud that travel under the influence of the applied electric field to the other end to be collected by the anode to produce measurable signals.

3.3.5 Rough surface as anode: A raster scan of a smooth surface while probing a rough surface as an anode allows the generated electrons to drift toward anode without much interference. Fig. 3.9a shows the 2-D image from a raster scan of a smooth surface in which the far surface exhibits specific defects. The corresponding spectral response is shown in Fig. 6b. The spectral response of the charge collection is almost uniform with small and uniform regions of lower energy peak that do not correspond to the location of the defects shown in fig. 3.8a. This uniform response is believed to result from the contribution of the electrons generated near the smooth cathode surface to the detector's response, with virtually no loss. It is worth mentioning that bulk defects are not being considered which may cause the charge losses, because we are comparing two different surfaces of same bulk material.

Electrons generated near the smooth cathode surface, drift all the way to the anode without hindrance before being collected. While electrons drift from the generation center toward the anode under an applied electric field, they undergo diffusion that broadens the electron cloud. Diffusion is believed to overwhelm the effects of induced defects due to roughness.

A fraction of the electrons from the broadened electron cloud impinges on the defects at the rough anode surface causing minimal charge loss that explains the very poor resolution images of the defects (dark regions in fig. 3.9a).

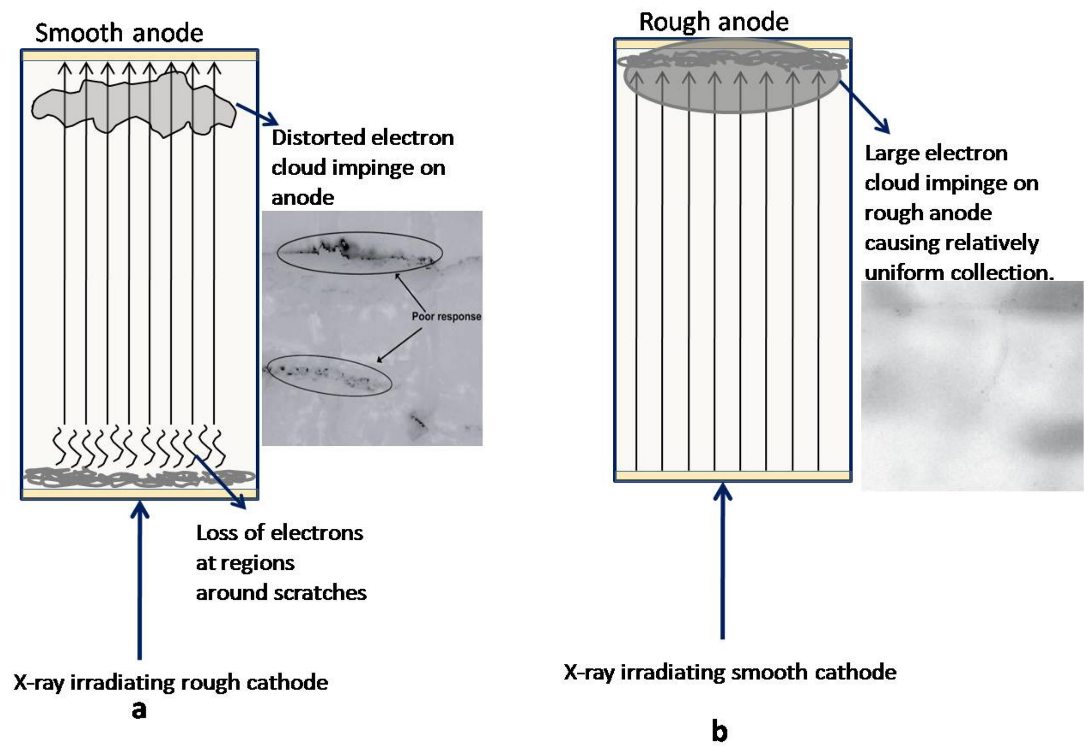

Figure 3.10 Schematics comparing the images generated when rough cathode, anode are irradiated. (a) the rough cathode is irradiated so that electrons are collected at a smooth anode, and (b) the smooth cathode is irradiated so that electrons are collected at a rough anode.

The induced charges mostly will contribute to the signal response as we can see from equation 1 [27, 28]. Full charge collection can be obtained if the thickness of rough region is much less than the electron's traveling distance according to Ramo's theorem. Therefore the effects of roughness will be less pronounced in large volume crystals ideal for high energy radiation detectors than in thin planar x-ray detectors

$$Q_c = Q_\circ\left(\frac{l-x}{l}\right), \ldots\ldots\ldots\ldots\ldots\ldots \text{Equation (2)}$$

where Q_c is the charge collection at rough surface, $Q_\circ$ is the charge collection at the original surface, l is the traveling distance of electron, and x is the thickness of surface roughness.

3.4 Conclusion

In this work, we used a high-spatial-resolution x-ray beam from a synchrotron source that allows us to precisely map areas as small as 10 μm^2 of a CZT detector's surface. We established a correlation between the 2-D images resulting from raster scans and the spectral response in charge collection that aided us in analyzing the characteristics of charge transport. We demonstrated, for the first time, the effects of surface roughness on detector's performance in terms of charge collection. We also demonstrated a clear correlation between the degree of surface roughness and the detector's leakage current.

We showed that the response of detector with a rough anode (and well polished, smooth cathode) differs noticeably from the response of the same crystal with a rough cathode (and well polished anode).

Micro-characterization of the surface roughness in CZT detector was somewhat limited by the fixed energy of x-ray beam, as we were able to evaluate only a certain region of surface roughness. Optimizing the beam's energy may prove beneficial in determining the specific nature and the level of the roughness as well as in resolving fine-grade roughness, knowledge of which may clearly indicate an optimal detector grade surface, and hence optimize the manufacturing process and performance.

REFERENCES

1. S. Ramo, Proc. IRE 27 (1939) 584
2. A. Hossain, A.E. Bolotnikov, G.S. Camarda, Y. Cui, S. Babalola, A. Burger and R.B. James. Journal of Electronic Materials Volume 37, Number 9 / September, 2008
3. Y. Cui, M. Groza, A. Burger, and R. B. James, IEEE Trans. Nucl. Sci., Vol. 51, (2004) 1172 – 1175.
4. H. Chen, K. Chattopadhyay, K.-T. Chen, and A. Burger, M. A. George, J. C. Gregory, P. K. Nag, J. J. Weimer and R. B. James, Journal of Vacuum Science & Technology A: Vacuum, Surfaces, and Films , Volume 17, (1999) 97-101
5. M. J. Mescher, T.E. Schlesinger, J.E. Toney, B.A. Brunett, and R.B. James. Journal of Electronic Materials Vol. 28, (1999) 700-704.
6. G. W. Wright, R. B. James, D. Chinn, B. A. Brunett, R. W. Olsen, J.M. Van Scyoc, M. Clift, A. Burger, K. Chattopadhyay, D. T. Shi, R. C. Wingfield, Proc. SPIE 4141 (2000) 324-335.
7. A. E. Bolotnikov, C. M. Hubert Chen, Walter R. Cook, Fiona A. Harrison, Irfan Kuvvetli, and Stephen M. Schindler, IEEE Trans. on Nuclear Science, Volume: 49 (2002) 1941- 1949.
8. A. A. Rouse, C. Szeles, J.-O. Ndap, S. A. Sodner, K. B. Parnham, D. J. Gaspar, M. H. Engelhard, A. S. Lea, S. V. Shutthanandan, T. S. Thevuthasan, and D. R. Baer, IEEE Trans. Nucl. Sci., Vol. 49, (2002) 2005–2009.

9. Y. Cui, G. Wright, K. Kolokolnikov, C. Barnett, K. Reed, U. N. Roy, Arnold Burger, Ralph B. James, SPIE Proceedings on Hard X-Ray and Gamma-Ray Detector Physics III, Vol. 4507 (2001) 12-22.
10. H. Prettyman, F. P. Ameduri, Los Alamos National Lab.; A. Burger, M. A. Hoffbauer, H. Nasr, D. Reisenfeld, S. E. Soldner, C. Szeles, SPIE Proceedings on Hard X-Ray and Gamma-Ray Detector Physics III, Vol. 4507 (2001) 22-31]
11. H. Chen, M.A. George, K. Chattopadhyay, J.C. Gregory, K.T. Chen, A. Burger, P. Nag, and R.B. James, J. Vac. Sci. Technol. A 17, 97 (1999).
12. A. Ruzin and Y. Nemirovsky, Appl. Phys. Lett. 71, 2214 (1997).
13. G. Tepper, R. Kessick, and Cs. Szeles, Proc. SPIE 4507, 79 (2001).
14. H. Chen, J. Tong, Z. Hu, D.T. Shi, G.H. Wu, K.T. Chen, M.A. George, W.E. Collins, A. Burger, R.B. James, C.M. Stahle, and L.M. Bartlett, J. Appl. Phys. 80, 3509 (1996).
15. H. Chen, S. U. Egarievwe, Z. Hu, J. Tong, D. T. Shi, G. H. Wu, K. T. Chen, M. A. George, W. E. Collins, A. Burger, R. B. James, C. M. Stahle, and L. M. Bartlett, Proceedings SPIE-Int., Soc. Opt.Eng., 2859 (1996) 254
16. H. Chen, J. Tong, Z. Hu, D. T. Shi, G. H. Wu, K.-T. Chen, M. A. George, W. E. Collins, A. Burger, R. B. James, and C. M. Stahle, J. Appl. Phys. 80 (6) 1996, pp 3509.
17. A. E. Bolotnikov, G. S. Camarda, G. A. Carini, Y. Cui, L. Li, and R. B. James, Nucl. Instrum. Methods Phys. Res. A 579, 125 2007
18. G.A. Carini, A.E. Bolotnikov, G.S. Camarda, G.W. Wright, G. De Geronimo, D.P. Siddons, and R.B. James, IEEE Trans. Nucl. Sci. NS-52, 1941 (2005).

19. G.S. Camarda, A.E. Bolotnikov, G.A. Carini, Y. Cui, K.T. Kohman, L. Li, and R.B. James, Proc. SPIE 6319, 1 (2006).

20. B.A. Brunett, J.M. Van Scyoc, N.R. Hilton, J.C. Lund, R.B. James, and T.E. Schlesinger, IEEE Trans. Nucl. Sci. NS-46, 237 (1999).

21. B.A. Brunett, J.M. Van Scyoc, T.E. Schlesinger, and R.B. James, Nucl. Inst. Meth. A 458, 76 (2001).

22. L. Longxia, Yinnel Tech., personal correspondence, 2007.

23. Linear Attenuation Coefficient data, http://www.amptek.com/anczt1.html, 2007

24. S.H. Park, Y.K. Kim, and H.S. Kim, IEEE Nuclear Science Symposium Conference Record, (2005), N35-57.

25. J. R. Brews, IEEE Trans Electron Devices, ED-26 (1979) pp 1282

26. G. Zha, W. Jie, T. Tan, P. Li Applied Surface Science, 253, 7,(2007). pp. 3476

27. H. S. Kim, S. H. Park, Y. K. Kim, J. H. Ha, S. M. Kang and S. Y. Cho, Nucl. Instr. Meth. A 579, 117 (2007).

28. Hecht, K., Z. Phys. Title 77 (1932), p.

CHAPTER IV

CHEMICAL ETCHING EFFECTS ON CZT AND CMT NUCLEAR DETECTORS

Overview

The fabrication process for CZT nuclear detector includes mechanical polishing, which is discussed in full in chapter 3, followed by chemical etching, which is the main focus of this chapter. While mechanical polishing is performed to diminish the damage induced during slicing of the ingot, the polishing process also induces micro-scale damages on the surface. Chemical etching is done to remove the remaining damage on crystal surfaces to obtain defect-free optically flat surfaces. This chapter discusses the results of a systematic study of different etching agents on CZT and CMT crystals. Several CZT and CMT samples were prepared by polishing with decreasing sizes of Al_2O_3 abrasive papers and slurry as described in chapter 3. The crystals were then etched for different durations of time with a 2%, 5% Bromine-Methanol (B-M) solution, and also with an E-solution (HNO_3:H_20:$K_2Cr_2O_7$). These chemical etchants are widely used in surface etching of semiconductor crystals [1-3]. The etched crystals were studied with Atomic Force Microscope (AFM) [see appendix 4] and infrared imaging in reflection mode to reveal the nanometer-scale features of surface morphology. The etching rate, i.e. rate of material removal from the crystal surfaces, was estimated for each of the etchants. The information helped to optimize the surface processing technique that yields suitable quality of nuclear detectors.

4.1 Motivation

CZT is the most promising material for room-temperature radiation detectors in the present day [4, 5]. CMT similarly has attracted attention due to its potentially useful characteristics and its similarities to CZT [6-8]. However, for both materials, many drawbacks remain associated with the various steps from crystal growth to detector fabrication, which must be resolved to produce good quality detectors. We are particularly interested in the fabrication process wherein surface processing is an important step as it plays a critical role in determining the detectors' performance. Many studies have explored the surface processing of CZT radiation detectors [9-13], but only a few have studied CMT detectors. Studies show that surface properties can influence the electric field inside the device, and significantly affect charge transport and signal formation [14,15]. A rough surface enhances leakage current into the medium and creates additional trapping centers, thereby adversely affecting the detector's performance. Therefore, it is essential to evaluate the surface processing steps to identify those that deliver the best surfaces for developing good quality radiation detectors.

The crystal surfaces first are polished mechanically to diminish the damage from cutting, followed by chemical etching to remove any remaining damage from crystal cutting, and damage induced during mechanical polishing. Chemical etching removes a surface layer that has been degraded during storage [16]. Etching is also used for cleaning, for bright surface polishing in which etch pits reveal the Cd or Te termination, and for surface enrichment by Cd, Te or oxides. [17]

Several etchants are suitable for chemically etching CZT and CMT crystal surfaces [18-21], the most widely used being bromine-methanol (B-M) solution. Chemical etchants react with the crystal surfaces, remove a certain amount of material from the top layers, and leave behind a smoother surface. Each chemical has certain etching strength, and hence, the material-removal rate varies depending on the strength of the etchants and the material that is being etched. To ensure a reasonably good surface outcome, we need data to optimize the type of etchant, its concentration, and the etching time for particular crystal surfaces.

4.2 Process of chemical etching

Although finely polished crystal surfaces look optically flat and smooth, the surfaces are actually decorated with localized surface features such as grain boundaries, sub-grains and damages induced by mechanical polishing of the crystal surface. These features have high radii of curvatures such as sharp edges and corners thereby enhancing the electric field that results in higher leakage current. Also, atoms on the surfaces are not completely bound, but rather feature dangling bonds that make surfaces very reactive. Metal-semiconductor contacts are greatly influenced by the presence of surface states, contamination and inter-diffusion between the metal and semiconductor during the metal deposition process. Chemical etching during detector fabrication is usually done for the purpose of cleaning the crystal surface. Chemical etching agents consist of three key ingredients, namely:

a) An oxidizing agent such as H_2O_2 and HNO_3.

b) A reducing agent, which is an acid or base that dissolves the oxidized surface, such as H_2SO_4 and NH_4OH.

c) The diluting media through which reactants and products are transported away from the surface of the etched material, such as H_2O and CH_3COOH.

Etching is achieved in a three-step process. First step involves transport of the reactants to the surface. The second step is the surface reactions involving electron transfer process, i.e. oxidation of one or more species and simultaneous reduction of the other species, while the third step is the transport of the products from the surface to leave a clean material surface thereby reducing the surface states, leakage current and also improving light reflection characteristics of the crystal surface. An example reaction of $H_2O_2 : H_2O : HF$ with the surface of a semiconductor X, is given below:

$$2X + H_2O_2 = 2XO + H_2O \text{ (oxidation)}$$

$$2XO + 6HF = H_2XF_6 + 2H_2O \text{ (Reduction)}$$

The smoothness of the etched surface depends on the rate of material removal by the etchant; slower etchants produces finer surfaces.

The most commonly used chemicals for etching the surfaces of CZT and CMT crystals include bromine-methanol solution [22-26], E-solution [27], P-solution [27], and Nakagawa solution [28]. Table 4.1 summarizes the use of the chemical etchants.

Table 4. Different etching reagents.

Name	**Composition**	**Etching action**
E - solution	Concentrated HNO_3 10ml H_20 20ml $K_2Cr_2O_7$ 4g	Chemical polishing
Br-methanol	2% or 5% Br in methanol	Chemical polishing
P - solution	Concentrated HCl 10ml H_2O 5ml	Chemical polishing
EAg-1	E-solution 10ml $AgNO_3$ 0.5mg	Etch-pit formation
EAg-2	E-solution 10ml $AgNO_3$ 0.5mg	Etch-pit formation
P-Br	P-solution 10ml Br_2 0.5mg	Etch-pit formation
Nakagawa solution	H_2O 100 ml H_2O_2 100 ml HF 150 ml	Etch-pit formation

4.3 Experiment

Several detector-grade CZT and CMT crystals of different shapes and sizes were used in this experiment. All CZT crystals were from the same growth batch, as was the case for the CMT crystals. The CZT samples were bar shaped with dimensions of ~5x5x10 mm^3, while the CMT samples were planar with dimensions of ~8x10x2 mm^3. Three sets, each comprising one CZT and one CMT crystal, were mechanically polished with 5 μm and/or lower grits Al_2O_3 abrasive papers including final polishing with 0.05 μm particle size alumina powder and then rinsed in distilled water. To compare the surface roughness of identical surfaces before and after chemical etching, one half of the polished surfaces of all crystals were covered with nonstick insulating tape while the second half was chemically etched for 2 minutes with a 2%, a 5% B-M solution and with the E-solution, then rinsed with pure methanol and quickly blow dried with pressurized nitrogen gas. Infrared (IR) refection images of the crystals were taken before and after etching the surfaces. To measure the roughness of those surfaces, atomic force microscopy (AFM) was used to image the polished and etched surfaces of each sample. The AFM instrument used is an Innova Scanning Probe Microscope (SPM) with a nanodrive controller for an Innova large area single-tube piezoelectric scanner. A contact mode etched silicon probe with symmetric tip of height of 15 microns and thickness of 4 microns was used in scanning the areas.

Another two sets of CZT and CMT crystals were employed for studies of the dissolution rate and a chemical aging experiment. The crystals were etched with the same chemical etchants for periods up to 10 minutes at room temperature. In each case the crystal thickness was measured with a micrometer before and after etching to quantify the amount of material removed from each surface. The entire crystal was dipped into the chemical solution during etching to ensure the etchants uniformly acted on all the crystal surfaces.

4.4 Results and discussion

Fig. 4.1 shows two set of IR reflection images of six representative crystal surfaces. All samples were lapped and finally polished with 0.05 μm grit alumina powder. Half of each sample was etched with the three different etchants and other half remained as polished.

They were all subjected to the same polishing procedure so that we could use one polished surface as a reference. The IR images in Fig. 4.1 shows chemical etching significantly removed the surface damage. Although the E-solution also removed the polishing damage, it created some pits so yielding a non-homogeneous surface. Longer etching times enhanced the number of pits and the unevenness of the surface. We were unable to generate a flat uniform surface in either CZT or CMT crystals by etching in the P solution, either for 30 sec or up to 2 minutes (Fig. 4.2). Longer etching also enhanced the roughness in this case. Seemingly, the concentrated nitric acid reacted with Cd(Zn/Mn)Te and left behind black tellurium layers on the etched surface, possibly the reason for the unevenness. This effect was reproducible in both the CZT and CMT crystal surfaces and is deemed unsuitable for surface processing of crystals.

The etching rate of different chemical etchants on CZT and CMT crystals after different exposure times was studied. Fig. 4.3 plots the average amount of material removed from CZT crystals after treating with different etchants for times from 30 seconds to 10 minutes.

Etching with the 5% B-M solution removes an average layer of about 125 μm from the crystal's surface in 10 minutes; however, the removal rate is not linear, and gradually decreased with time.

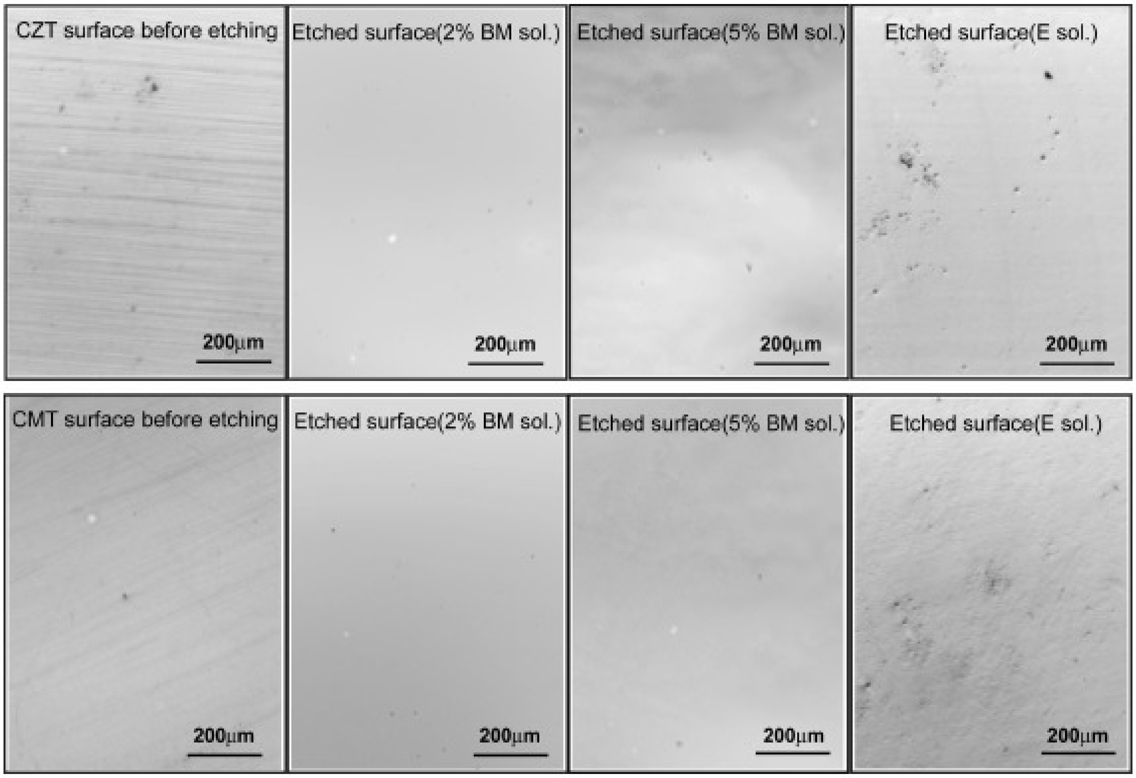

Figure 4.1 IR reflected images of the polished and etched crystal surfaces. The polishing damage was removed substantially by etching with different chemical etchants. The top row consists of images of the CZT crystals, and the bottom row consists of the CMT crystals. Note the pits on the surfaces treated with the E solution.

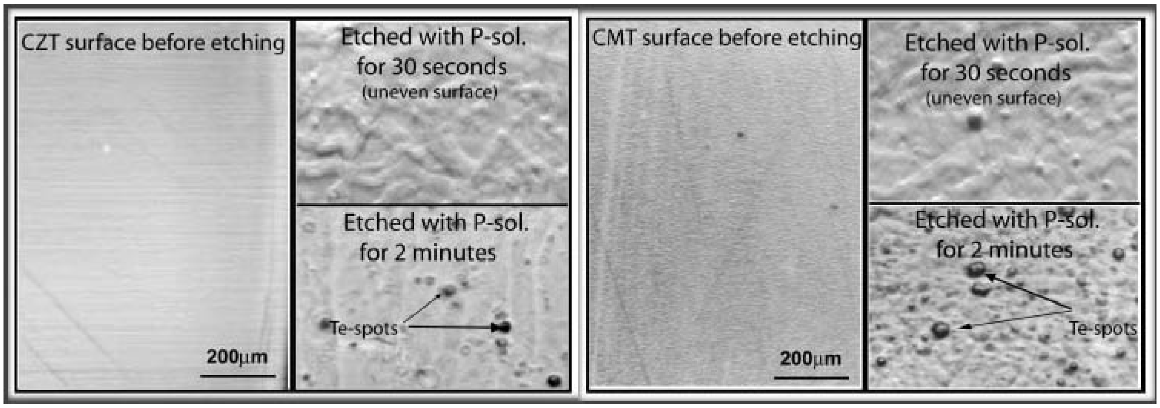

Figure 4.2 IR reflected image of the CZT (left) and the CMT (right) crystal surfaces before and after etching with the P-solution. 30 seconds etching left uneven surfaces, and 2 minutes etching left some Te- spots.

The average etching rate was estimated to be about 30 μm per minute. Etching with 2% B-M solution showed a similar trend, but with a slower rate of 10 μm per minute while the etching rate of the E solution was estimated to be about 15 μm per minute. Burger et al. [10] reported an etching rate about 50 μm per minute for a 2-10% B-M solution. For our solution aging experiments 5% B-M solution and E-solution were prepared at room temperature and exposed to air for 2 hrs, 4 hrs, and 8 hrs after which they were used to etch the samples for 2 minutes.

Fig. 4.4 shows the result of this aging experiment. The samples exposed to fresh B-M solution had a higher etching rate than those treated with solutions aged for 4 hours and even greater for those left 8 hours. Furthermore, the aged solutions left readily visible layers of black tellurium on the etched surfaces. However the reaction of E-solution was more or less linear over the aging period. The aging effect may reflect a change in the solution's pH. Rouse et al. [29] found that the acidity of etching solutions increase significantly over 8 hrs.

The increasing acidity could be due to the uptake of moisture or CO_2 from air with time [30]. As the acidity of the solution increases, selectivity for cation etching increases, leading to an increasingly Te-rich surface.

The etching rate of 5% B-M solution decreased with increasing exposure time, but remained more or less linear for E-solution over the aged period. The uniformity and roughness of the etched surfaces are not easily analyzed by IR images, so the AFM method was used to study more precisely the surface roughness of the polished and etched surfaces.

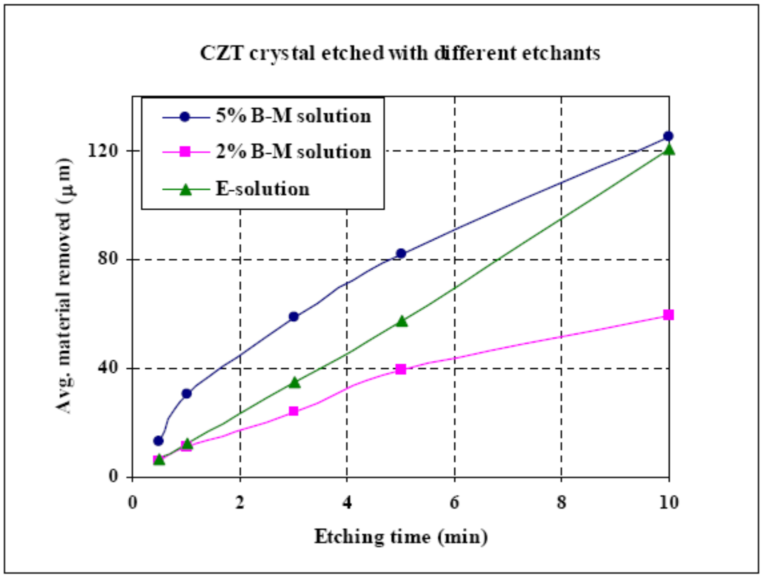

Figure 4.3 Plot of the effect of different chemical etchants on CdZnTe crystals. The etching rate of the 2%-, 5%- B-M solutions and the E solution is about 10 μm, 30 μm, and 15 μm, respectively.

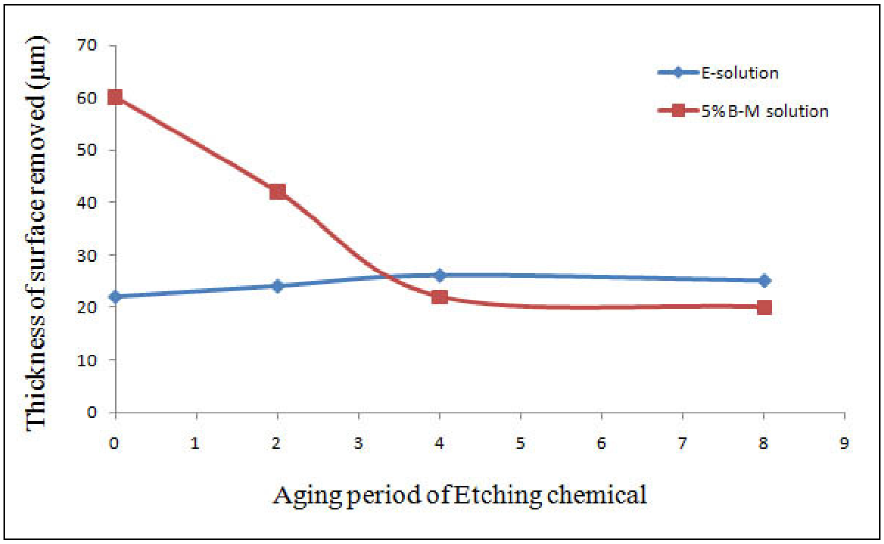

Figure 4.4 Graph of the effect of aging the etchants in air on the removal of materials from two crystals.

Fig. 4.5 shows AFM images of one polished surface and three different etched surfaces of CdZnTe crystals. The Root-Mean-Square (RMS) roughness of the polished surface was estimated to be around 9 nm. Etching with 2% B-M solution lowered the RMS roughness value to about 2.5 nm, while etching with 5% B-M solution reduced the RMS roughness to about 1.3 nm. From AFM images it can be seen that etching with 5% B-M solution has removed the surface damage that can be estimated to be about 88%, whereas 74% with 2% B-M solution and 35% with E-solution.

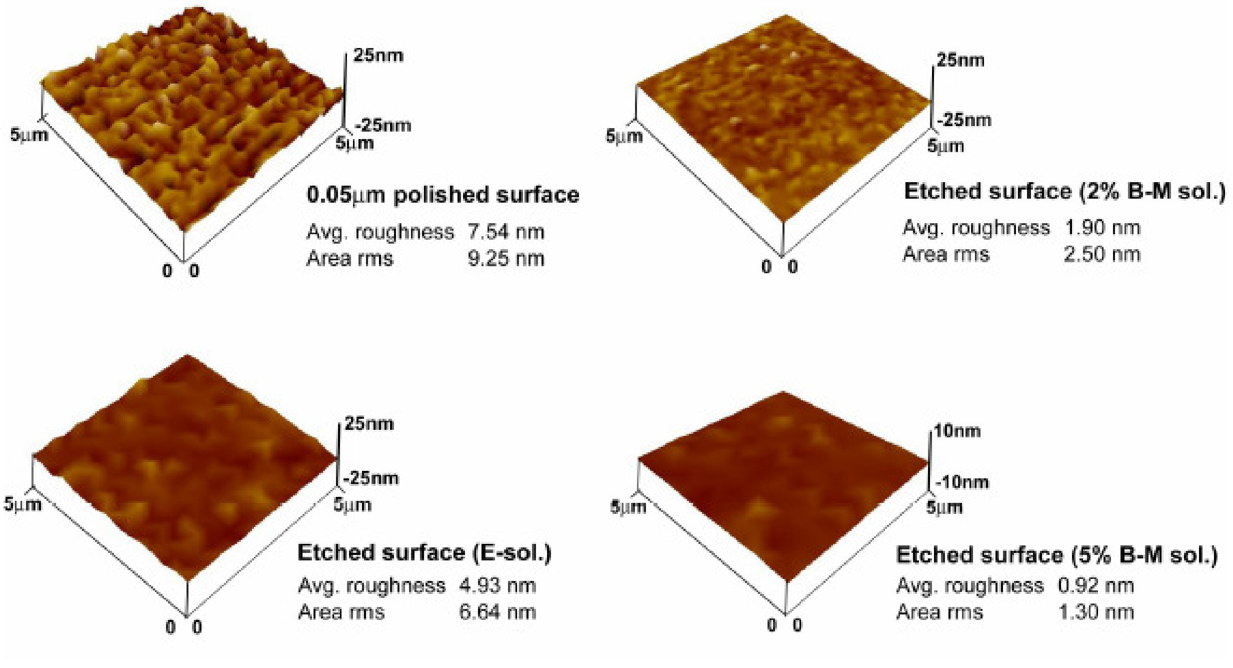

Figure 4.5 AFM images of polished and etched surfaces of the CdZnTe crystals. The lowest rms roughness was obtained after etching with 5% B-M solution followed by the 2% B-M solution; the E- solution was not as efficacious.

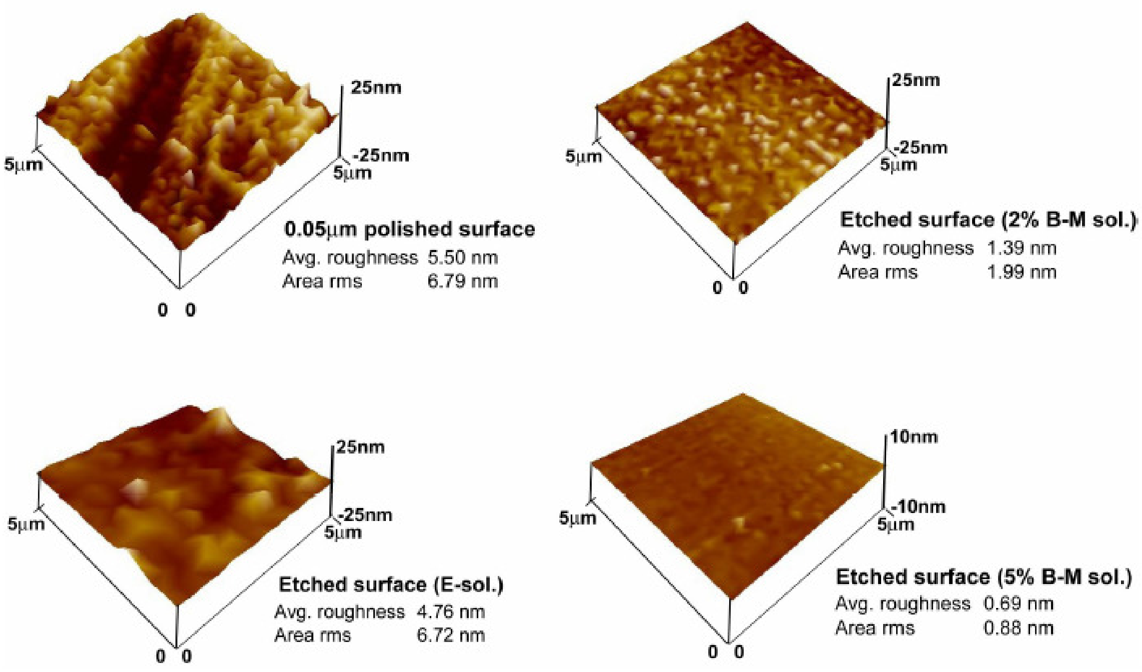

Figure 4.6 AFM images of the polished and etched surfaces of CdMnTe crystal. The lowest rms roughness was attained after etching with 5% B-M solution as compared to a 2% B-M solution and the E solution.

Fig. 4.6 shows the same measurement for CMT crystals. Chemically etching these crystal surfaces provided even better RMS roughness values than did the CZT surfaces. Starting with an RMS roughness of polished surface of around 7 nm, etching with 2% B-M solution lowered the value to about 2 nm, and to 0.9 nm with the 5% B-M solution. Etching CMT crystal's surface with the E solution left a comparatively rougher surface than did the B-M solution at either concentration.

4.5 Conclusion

This work demonstrated that polishing damage can be substantially removed by chemical etching with either type of chemical etchant i.e., a B-M solution at different concentration, or an E solution, although to different extents. The amount of material removed with different concentrations of these etchants and different immersion times were estimated. This information will help to enhance the process of preparing smooth crystal surfaces. This study shows higher percentage of B-M solution with shorter etching time to yield a smoother surface, which is suitable for detector fabrication. This experiment shows that E- and P-solutions are not useful for polishing-etching of CZT and CMT crystals for detector fabrication; however, further investigation is needed to understand the reason behind this observation. AFM was used to obtain detailed information about the topography of the etched surfaces, especially roughness and uniformity, which will help in selecting the appropriate surface-etching preparations for making good detectors. The effects of different chemical etchants on the surfaces of CZT and CMT detectors, and the differences in etching rates between the E solution and the B-M solution that reduced with time over 10 minutes are reported. However, further investigation is needed to optimize conditions, using the smallest sized polishing grit and the subsequent most suitable chemical etchant. In combination with other surface processing, this may yield a crystal surface of suitable quality for fabricating a good detector.

REFERENCES

1. C.S. Fuller, H.W. Allison, J. Electrochem. Soc. 109 (1962) pp. 880
2. I.M. Dharmadasa, G.G. Roberts, M.C. Petty, J. Phys. D: Appl. Phys. 15 (1982) pp. 901.
3. P.Gaugasa, A.G. Milnes. J. Electrochem. Soc. 128 (1981) pp. 924.
4. Takahashi, T. and Watanabe, S., "Recent Progress in CdTe and CdZnTe Detectors", EEE Trans. Nucl. Sci. NS-48 (4),950-959 (2001).
5. Eisen, Y., "Current state-of-the-art industrial and research applications using room-temperature CdTe and CdZnTe solid state detectors", Nucl. Instr. and Meth. A 380, 431-439 (1996).
6. Burger, A., Chattopadhyay, K., Chen, H., Ndap, J.O., Ma, X., Trivedi, S., Kutcher, S.W., Chen, R. and Rosemeier, R.D., J. Crys.Growth 198/199, 872-876 (1999).
7. Zhang, J., Jie, W., Wang, T., Zeng, D. and Yang, B., J. Crys.Growth 306, 33-38 (2007).
8. Parkin, J., Sellin, P.J., Davies, A.W., Lohstroh, A., Ozsan, M.E. and Seller, P. Nucl. Instr. and Meth. A 573, 220-223 (2007).
9. Hossain, A., Bolotnikov, A.E., Camarda, G.S., Cui, Y., Babalola, S., Burger, A. and James, R.B., J. Elect. Mat., DOI: 10.1007/s11664-008-0431-6, (2008).
10. Burger, A., Chen, H., Chattopadhyay, K., Shi, D., Morgan, S.H., Collins, W.E. and James, R.B. Nucl. Instr. and Meth. A 428, 8- 13 (1999).
11. Yoon, H., Van Scyoc, J.M., Goorsky, M.S., Hermon, H., Schieber, M., Lund, J.C. and James, R.B. "Investigation of the effects of polishing and etching on the

quality of Cdl_xZnxTe using spatial mapping techniques", J. Elect. Mat. 26, 529-533 (1997).

12. Duff, M.C., Hunter, D.B., Burger, A. Groza, M., Buliga, V. and Black, D.R., Applied Surface Science 254, 2889-2892 (2008).
13. Kima, H.S., Parka, S.H., Kimb, Y.K., Haa, J.H., Kanga, S.M. and Choc, S.Y., Nucl. Instr. and Meth. A 579, 117-119 (2007). Proc. of SPIE Vol. 7079 70791E-7
14. Prettyman, T.H., Ameduri, F.P., Burger, A. Gregory, J.C., Hoffbauer, M.A., Majerus, P.R., Reisenfeld, D.B. Soldner, S.A. and Szeles, Cs., Proc.SPIE 4507, 25-31 (2001).
15. Prettyman, T.H., Hoffbauer, M.A., Rennie, J.A., Cook, S., Gregory, J.C., George, M. A., Luke, P.N., Amman, M., Soldner, S.A. and Earnhart, J.R. Nucl. Instr. and Meth. A 422, 179-184 (1999).
16. X.J. Bao, T.E. Schlesinger, R.B. James, A.Y. Cheng, C. Ortale (1990),Mat. Res. Soc. Symp. Proc. 163, pp 1027.
17. page 269 of semiconductors n semimetals
18. Chen, H., Tong, J., Hu, Z., Shi, D.T., Wu, G.H., Chen, K.-T., George, M.A., Collins, W.E. and Burger, A., J. Appl. Phys. 80,3509-3512 (1996).
19. Rybka, A.V., Leonov, S.A., Prokhoretz, I.M., Abyzov, A.S., Davydov, L.N., Kutny, V.E., Rowland, M.S. and Smith, C.F., Nucl. Instr. and Meth. A 458, 248-253 (2001).
20. Wright, G., Cui, Y., Roy, U.N., Barnett, C., Reed, K., Burger, A., Lu, F., Li, L. and James, R.B., IEEE Trans. Nucl. Sci. NS-49(5),2521-2525 (2002).

21. Sang Wenbin; Jin Wei; Zhang Qi; Min Jiahua; Zhang Minglong; Teng Jianyong; Qian Yongbiao, 2004. HDP '04. Proceeding of the Sixth IEEE CPMT Conference on , vol., no., pp. 377-379, 30 June-3 July 2004.
22. Zheng, and A. Burger, J. Appl. Phys., vol. 77, no. 7, pp. 3134-3137, Apr. 1995.
23. J. G. Werthen, J.-P. Haring, A. L. Fahrenbruch, and R. H. Bube, J. Appl. Phys., vol. 54, no. 10, pp. 5982-5989, Oct. 1983.
24. J.-P. Haring, J. G. Werthen, R. H. Bube, L. Gulbrandsen, W. Jansen, and P. Luscher, J. Vac. Sci. Technol. A, vol. 1, no. 3, pp. 1469-1472, 1983.
25. I. M. Dharmadasa, J. M. Thornton, and R. H. Williams, Appl. Phys. Lett., vol. 54, no. 2, pp. 137-139, Jan. 1989.
26. J.F. Butler, in Properties of Narrow Gap Cadmium-based Compounds, P. Capper, Ed., London, INSPEC, pp.587-590, 1994.
27. Inoue, M., Teramoto, I. and Takayamagi, S., “Etch pits and polarity in CdTe Crystals”, J. Appl. Phys. 33,2578- 2582 (1962).
28. K. Nakagawa, K. Naeda and S. Takeuchi, Appl. Phys. Lett. 34, 574 (1979).
29. Rouse, A.A., Szeles, Cs., Ndap, J.-O., Soldner, S.A., Parnham, K.B., Gaspar, D.J., Engelhard, M.H., Lea, A.S., Shutthanandan, S.V., Thevuthasan, T.S. and Baer, D.R., IEEE Trans. Nucl. Sci. NS-49(4),2005-2009 (2002).
30. A. Etcheberry, F. Iranzo-Marid, E. Novakovic, R. Tribouletb, and C. Debiemme-houvy, J. Crys. Growth 184/185, 213-217 (1998). Proc. of SPIE Vol. 7079 70791E-8

CHAPTER V

STUDY OF BULK DEFECTS IN CZT AND CMT CRYSTALS

Overview

One of the major limitations to the use of CZT and CMT crystals for high energy gamma ray detection at room temperature is the presence of defects in the bulk crystals that affect detector performance. This chapter addresses the different defects found in CZT and CMT crystals. The defects are discussed in terms of their formation, concentration, methods of study and the findings. The effects of such defects on nuclear detector performance are studied and reported. The CMT crystal has the potential to be a better nuclear detector material than CZT. However CMT crystals have just been introduced and are the subject of extensive on-going research. This report introduces CMT nuclear detectors and highlights their advantages and drawbacks. Also spectra obtained from CMT nuclear detector's response to high energy gamma ray are reported for the first time, and a key limiting factor for detection performance in today's best CMT crystals is identified. The effects of this limitation on electric field distribution within the bulk of the crystal as well as on spectra are discussed. In this work, extended defects have been characterized using infrared (IR) spectroscopy both in transmission and reflection mode, white-beam X-ray diffraction topography, Pockels electro-optic effect employing the birefringence nature of the crystals, etch pit density (EPD) measurements and microscale x-ray mapping, and the results and discussions are presented.

5.1 Motivation

Large volume CZT and CMT crystals are sought for making detectors for high energy gamma-rays with extended thicknesses and large effective areas. However the crystallinity of CZT and CMT materials remain a serious problem. Large crystals are usually not perfect single crystals due to several defects present in the ingot. The structural defects include voids and pipes. The defects also include impurities from source materials, Tellurium (Te) inclusions and Te precipitates, vacancies and vacancy-impurity complexes produced during crystal growth. Other extended defects include grain boundaries, micro twins and dislocation walls. Identification and control of these defects and charge compensators in the bulk material are currently important issues that affect detector yield.

5.2 Defects

The major defects in any single crystal, including CZT and CMT crystals can be classified as either point or extended defects. Point defects occur when an atom is missing or is irregularly placed in the lattice structure. They include self interstitial atoms, interstitial and substitution impurity atoms, and vacancies. The point defects identified in CZT and CMT crystals include impurities from source materials, vacancies and vacancy-impurity complexes. Extended defects include Te inclusions, dislocations, grain and twin boundaries as well as ‘pipes’.

5.2.1 Te inclusions and precipitates: Te inclusions, typically ranging from 1-20 um, are formed in CZT at the growth interface [1] or annealing process due to the retrograde slope of the solidus line towards lower temperature or non-stoichiometric compositions [2,3] and also during the process of etching, due to the loss of Cd and Zn. Te inclusions can be easily identified by using transmission IR microscopy. They are different from Te precipitates (typical sized 10-50 nm) that form as a result of the nucleation of native defects. CZT decomposes thermally by evaporation of Cd leaving behind Te-rich melt (as illustrated in figure 5.1). The Te then precipitates along grain boundaries in the crystal.

Although the concentration of Te inclusions may exceed 10^7 cm^{-3}, this is several orders-of-magnitude less than that of the Te precipitates.

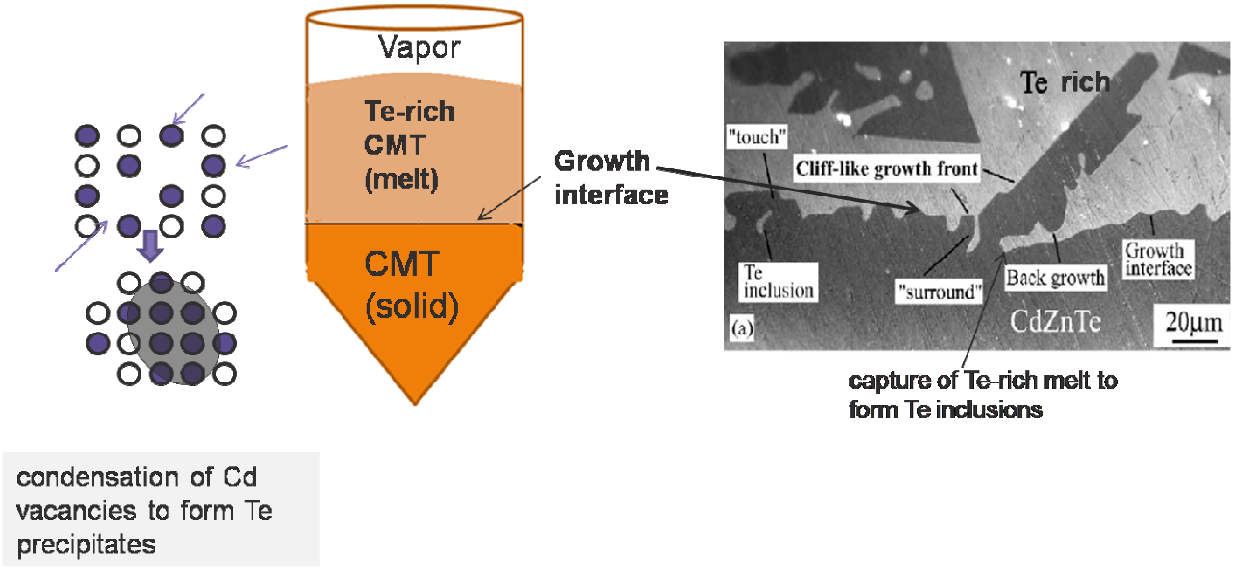

Figure 5.1 Schematic of formation of Te precipitate and CZT growth interface showing formation of Te inclusion [4]

Te precipitates and inclusions introduce stress and distort crystal lattices [5, 6], thereby reducing the transmittance of the crystals [7-9] and degrading the electrical properties. Te precipitates on the surface can also increase the leakage current [10], thereby deteriorating the device performance. Te inclusions and precipitates also act as traps for the charge carriers.

5.2.2 Other extended defects: Other extended defects in CZT crystals include grain and sub-grain boundaries, twins, dislocation walls and pipes. A grain boundary is the interface between two planes in a polycrystalline material. Strong charge trapping occur at grain boundaries, and for this reason high-performance detectors are exclusively fabricated from carefully mined single crystals. Twins occur when two separate grains symmetrically share some of the same crystal lattice points causing an intergrowth of two separate grains separated by a twin boundary. Dislocations are caused by termination of a plane of atoms in the middle of the crystal. Dislocations, shown in figures 5.2 and 5.3, are associated with dislocation walls or low angle boundaries [11]. Dislocations are introduced into the CZT and CMT wafers by means of bending deformations at elevated temperatures [12]. Dislocations have detrimental effects on nuclear detectors. Dislocations have been shown to create a large number of trapping or acceptor centers in CZT nuclear detectors [12]. Also, non-symmetrical conductivity in these detectors has been attributed to inhomogeneous distribution of dislocations [12]. The often quoted average density of dislocations in detector-grade CZT crystals is 10^4–10^5 /cm^2 [13-

15], but recently, high-quality crystals were grown with lower density (~3x10^3 /cm^2) [16].

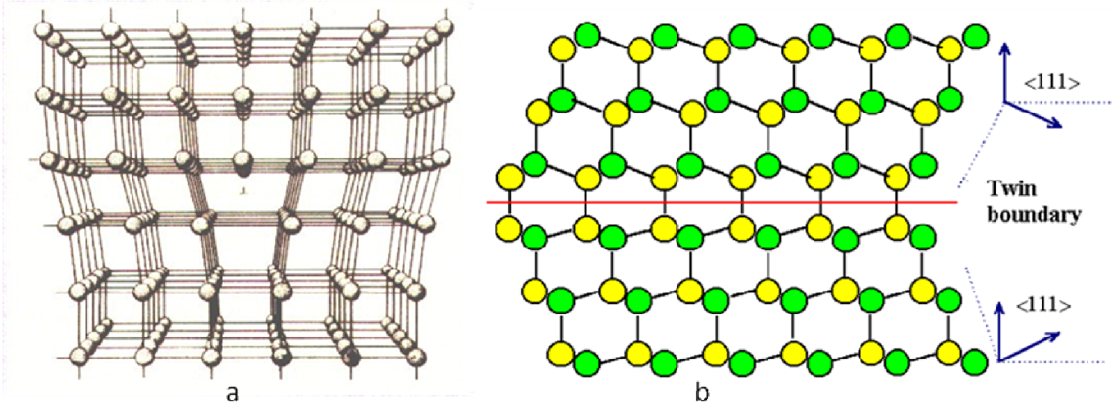

Figure 5.2 Schematics of a) edge dislocation, showing an extra plane of atoms, b) twin boundary, a highly symmetric grain boundary.

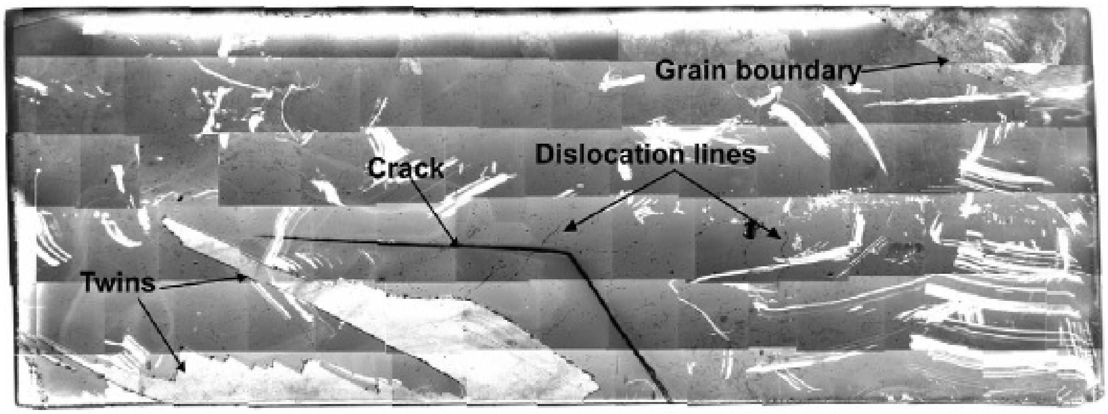

Figure 5.3 Infrared images (reflection) of 5 mm by 12 mm CZT crystal showing grain boundaries, twins, dislocation lines and cracks present on the surface of the crystal. The crystal was etched in Nakagawa solution.

5.3 Study of Defects in CZT and CMT crystals

Several techniques have been employed in the study of defects in CZT and CMT crystals for nuclear detector applications. These techniques and findings are presented below.

5.3.1 Infrared (IR) microscopy and analysis: Te-rich volumes have different optical and electrical properties than bulk CZT and CMT crystals. Due to the different absorbance, they can be identified by IR transmission microscopy. The IR microscopy system developed at BNL consists of a microscope with a large field of view objective and a 2208 x 3000 pixels CCD camera. An automatic IR transmission microscope system was developed at BNL for screening internal defects in CZT samples. The system encompasses a large field-of-view microscope coupled with a 3.5 μm pixel size digital camera, a set of translation stages for positioning the samples, and a light illuminator. The digital camera provides 2208 x 3000 pixel images with a resolution of 0.19 and 0.75 m per pixel depending on the lens' optical magnification. The system consists of a XYZ motorized translation stage with a resolution of 0.1 um. The three actuators are controlled via a PC using serial connectors. The software to communicate with the actuators was developed and written at BNL using a VC++ programming environment. The microscope objective, CCD camera, and the optic assembly system are mounted in line with the XYZ translation stages and the backlight fiber optic. Long working-distance objectives with magnifications (field-of-view (FOV)) from 2x (h 5.3mmx v 3.8mm) to 20x (h 0.53mm x v 0.38mm) were used. (see appendix A for details of IR microscopy system)

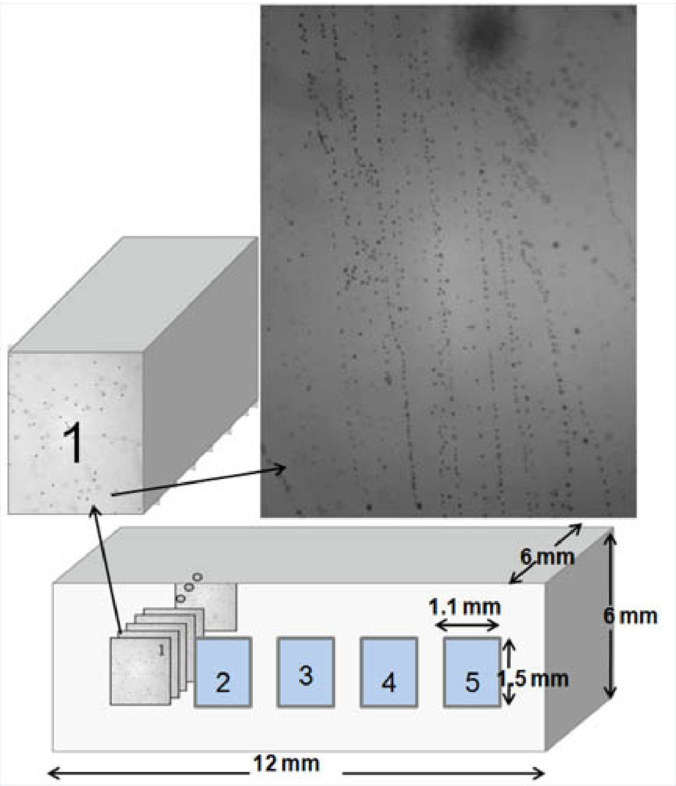

Figure 5.4 Schematics of automated IR imaging process. Five 1.1 x 1.5 mm^2 regions of a 6 x 6 x 12 mm^3 CZT crystal are imaged. Up to 100 images are taken from one surface to another in each region to make a total of ~500 IR images. One such image showing parallel lines formed by Te inclusions is shown.

IR images of the CZT are obtained in steps as shown systematically in figure 5.4. The important feature of this system is its iterative algorithm, developed using the Integrated Data Language (IDL) computer programming language, for counting Te inclusions and identifying their shapes and sizes. The code counts the number of Te inclusions in focus for each IR image while rejecting those Te inclusions that are out of focus. From the data obtained and also employing other IDL codes, the concentration, volume, excesses and statistical distribution of the Te inclusions are deduced. An example of the statistical data and a 3-D reconstructed image obtained by using the knowledge of the spatial positions of the Te inclusions in the crystal are

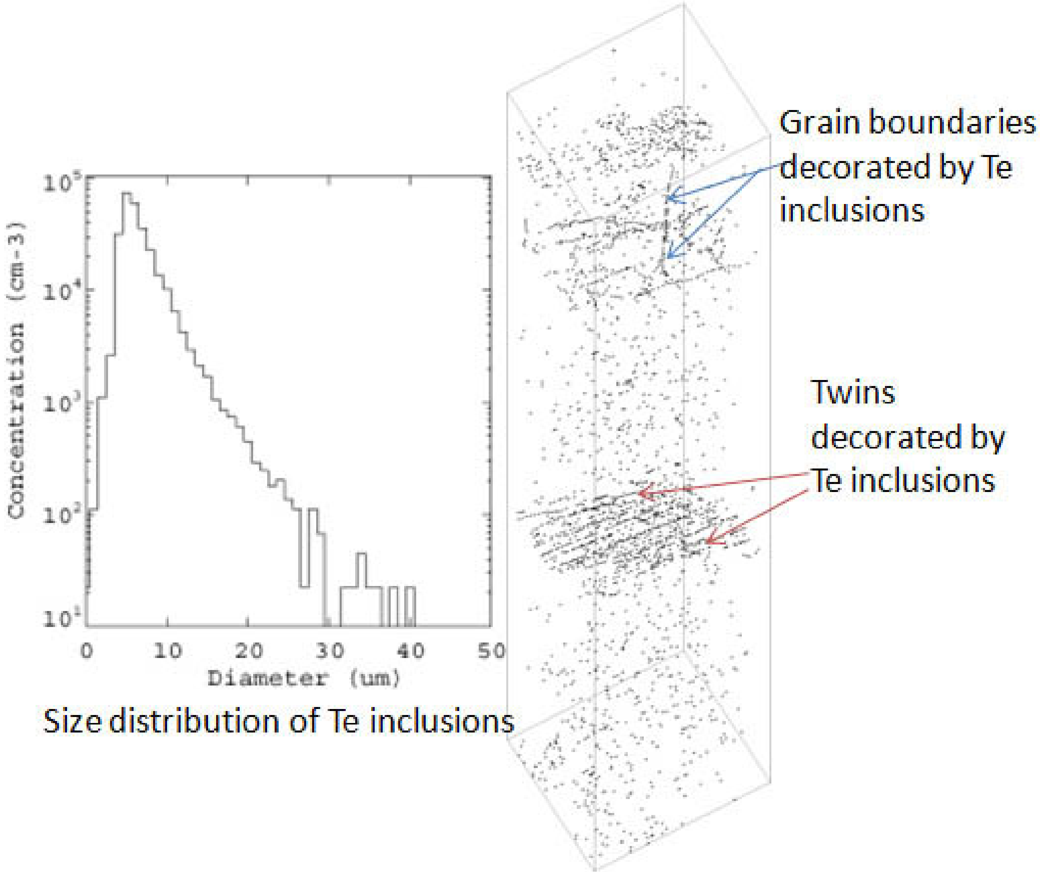

Figure 5.5 Size distribution and 3-D image of the 6 x 6 x 12 mm^3 CZT crystal generated from ~500 IR images showing grain boundaries and twins as decorated by Te inclusions.

shown in figure 5.5. The arrangement of Te inclusions along twins and grain boundaries are clearly observed. [17-18]. Te inclusions are seen in IR images as 2D intensity distributions of regular or more often irregular shapes depending on the inclusions' sizes and orientations.

5.3.2 Chemical etching to reveal defects in CZT and CMT crystals: The use of chemical etching to obtain optically flat and defect-free surfaces ideal for nuclear detectors was discussed in the previous chapter. Chemical etching is also used to reveal etch pits for observing Cd or Te termination. CZT samples were mechanically polished with Al_2O_3 abrasive paper of successively decreasing grits followed by fine 0.1 µm alumina powder. The samples were then chemically polished in 2% bromine–methanol (B–M) solution for 5 minutes. Afterwards, they were etched for 2–3 min by gently stirring in Nakagawa solution ($HF:H_2O_2:H_2O$; 3:2:2) solution [19]. After etching, the samples were dipped in B–M solution for one second to remove the black layer formed by etching, followed by blow-drying with nitrogen gas. The etched surfaces were studied with the IR microscope system in both transmission and reflection light modes. Figure 6 shows IR images of CZT crystal surface before and after etching. Linear etch-pits are observed on the surface of the crystal after etching. These etch pits are not Te inclusions on the surface as they are not observed before etching, but rather the etch pits represent termination of dislocation lines that are formed in the bulk of the CZT crystal and extend to the surface. Fig. 7 shows the etch pits on the surface of the crystal and the dislocation lines that extend into the bulk of the crystal.

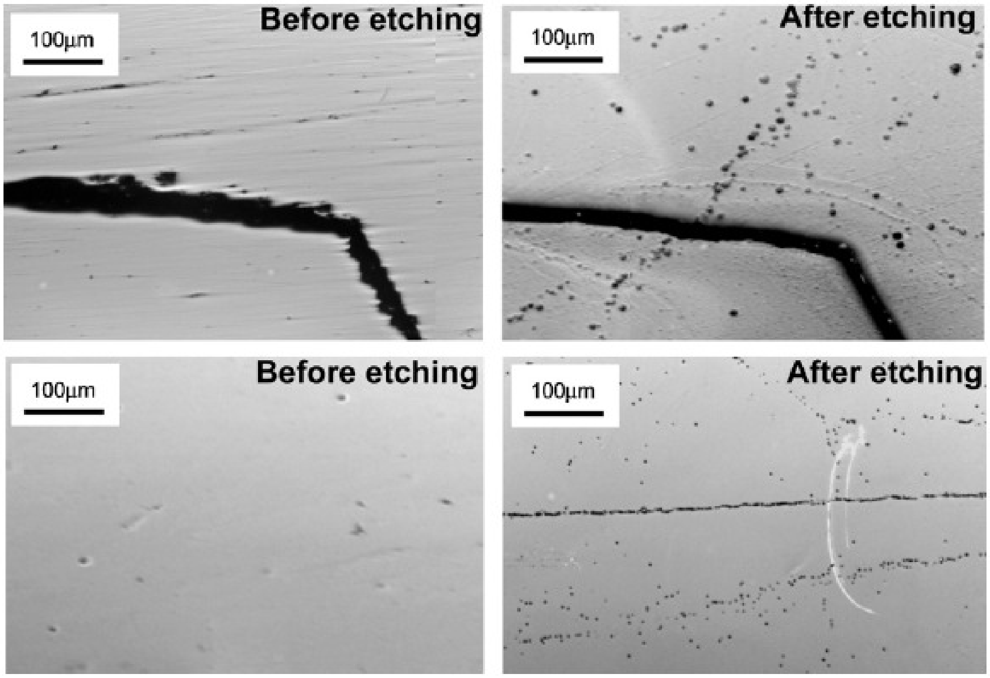

Figure 5.6 Nakagawa etching reveals linear etch-pit patterns on the surface of CZT crystals. The images at the right show linear etch-pit patterns that cannot be attributed to Te inclusions.

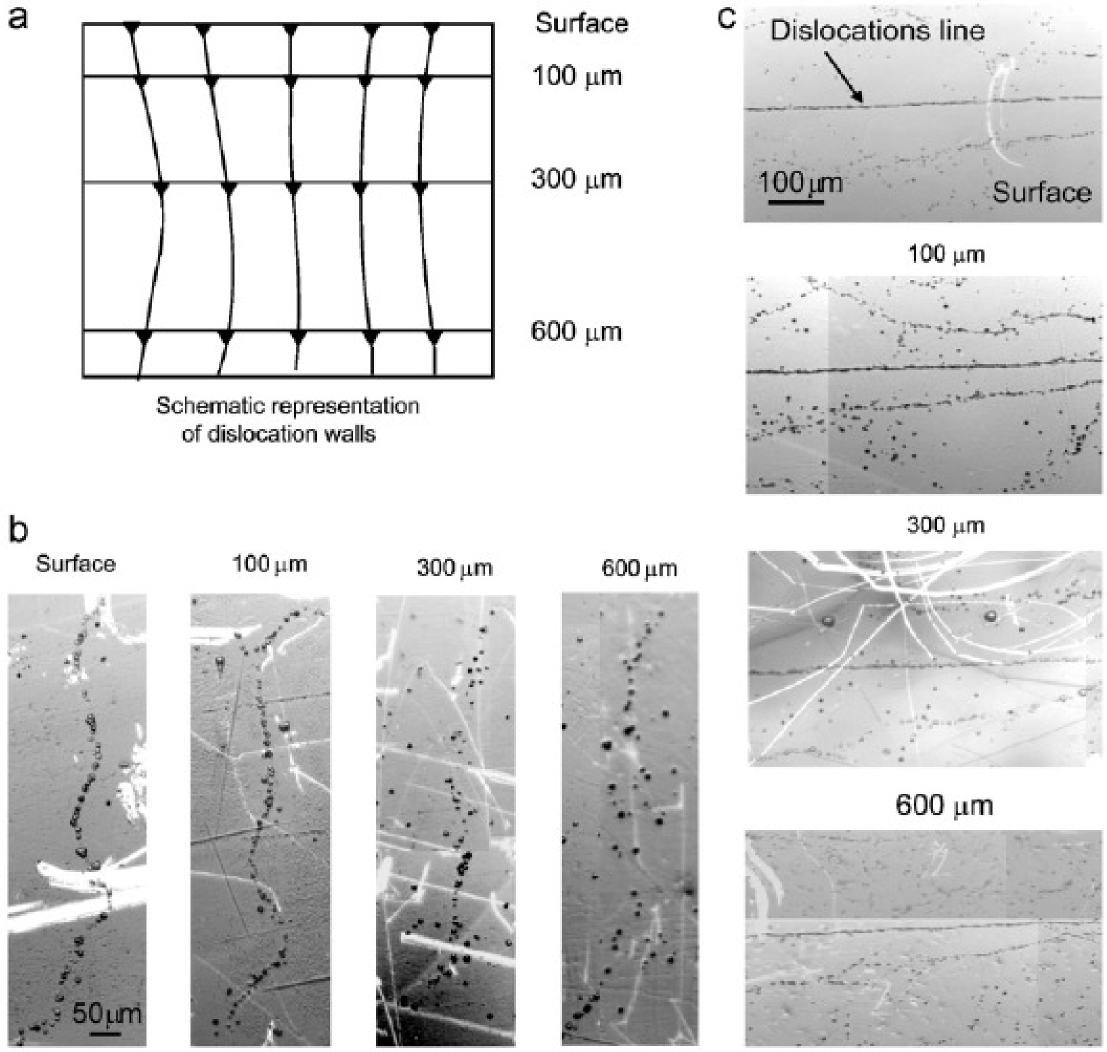

Figure 5.7 (a) Schematic representations of the dislocation lines and etch pits; (b, c) two sets of images showing dislocation lines emerging on the surfaces at different depths (indicated on the top of each image) taken from two different regions in the crystal.

5.4 Effects of Te inclusions and precipitates on the performance of CZT nuclear detectors

Several studies have shown that Te inclusions and precipitates in current CZT material could be critical in lowering the performance of thick, long-drift CZT detectors, thereby limiting the size and efficiency of the detectors[20-23]. Using the X-ray scan technique described in appendix 1, Carini et al [20] showed the correlation between Te inclusions and detector performance. In her work, 5x5x10 mm^3 Frisch-ring CZT detectors were scanned using 85 KeV quasi-monochromatic x-ray beam of 10 μm x 10 μm beam size. For each X-Y position of the x-ray beam, the pulse height spectra and peak positions (which correspond to the total collected charge) are evaluated and the scan result is plotted as two-dimensional maps of device performance as shown in fig. 8. The dark regions of x-ray map correspond to poor performance, i.e. shift of the spectra's peak position to lower energy , correlate well with Te inclusions identified with IR image of the sample. Fig. 9 shows ^{60}Co spectra and x-ray scans of two Frisch-ring CZT detectors with low and high concentration of Te inclusions. Both detectors were fabricated from the same region of CZT ingot and have similar values of the μτ product. The degradation of detector response is attributed to fluctuations of charge loss caused by trapping centers associated with inclusions. Te inclusions are extended local defects with a very high local concentration of trapping centers. The fluctuations in charge loss are therefore proportional to the total number of defects encountered by the electron cloud. Electric field distortions around Te inclusions can also contribute to the dispersion of the collected charges leading to further degradation in spectroscopic performance.

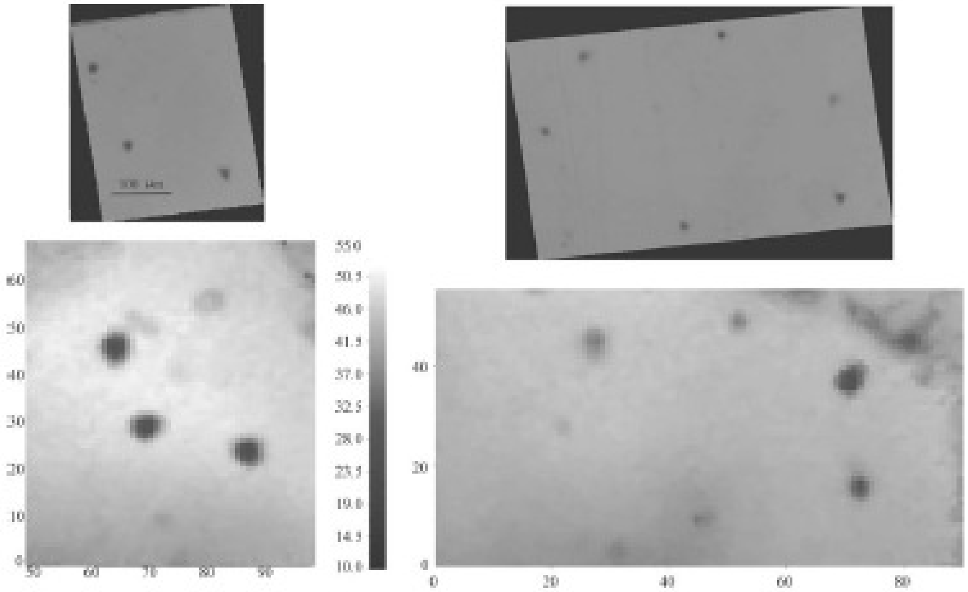

Figure 5.8 Correlations between x-ray (bottom) and IR transmission (top) maps measured for a 1 mm thick CZT planar device. The scans were performed by using a 10 x 10 μm^2 size, 85 keV x-ray beam. [19]

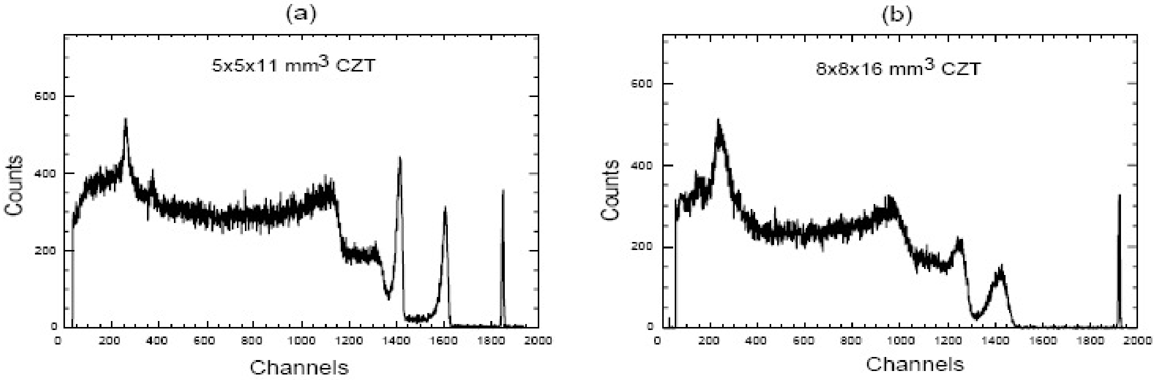

X-ray map
5x5x11 mm3 CZT

X-ray map
8x8x16 mm3 CZT

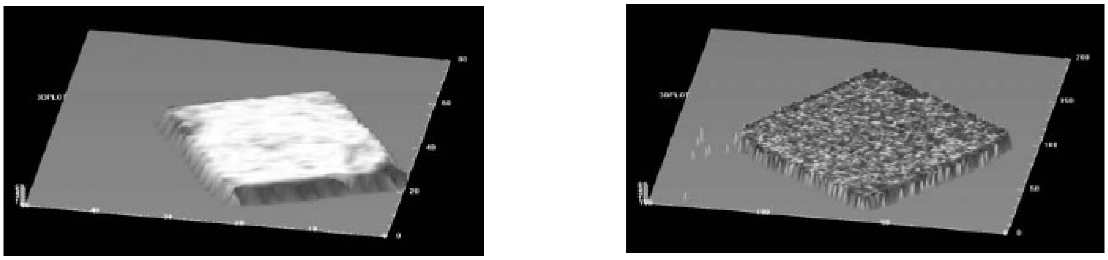

Figure 5.9 ^{60}Co spectra and X-ray scans measured for two Frisch-ring CZT detectors: (a) 11-mm long with a low concentration of Te precipitates, and (b) 16-mm long with high concentration of precipitates. The scans were performed by using a 25x25 μm^2 size, 85-keV beam. [20]

5.5 Modeling charge loss due to Te inclusions

The number of trapped electrons depends on the spread of the electric cloud, which in turn is governed by the amount of initially deposited charge and the electron drift time. A model for estimating the electron cloud broadening is suggested following the calculations of the effects of the spread of electron cloud on Si drift detectors [24]. The model predicts that for large deposited energies, electrostatic repulsion becomes the dominant effect that broadens the electron cloud. The broadening is independent of the initial charge distribution but depends on the total amount of deposited charge. Charge loss due to ordinary traps, i.e. uniformly distributed impurity levels, is described by

$$Q = Q_o \exp\left(\frac{t_{drift}}{\tau_{bulk}}\right) \qquad (1)$$

where Q and Q_o are the collected and initial charge generated, t_{drift} is the drift time of electron cloud from interaction point to the anode, and τ_{bulk} is the electron's lifetime in the CZT bulk. If an individual Te inclusion is considered as a microscopic region filled with a high concentration of ordinary traps, then

$$Q = Q_i \left(1 - n_i \left[1 - \exp\left(\frac{t_i}{\tau_i}\right)\right]\right) \qquad (2)$$

where t_i and τ_i represent the electron drift and lifetime respectively average over the i'th inclusion, and n_i is a fraction of charge from an electron cloud crossing the geometrical region of an inclusion. This equation is only applicable when exp $(t_i/\tau_i) < 1$. Charge loss due to interactions of an electron cloud with inclusions is a stochastic process, and t_i/τ_i could differ from one inclusion to the other. The fraction of electrons, η_i, located within a footprint of the i'th inclusion of a certain effective diameter D_i can be calculated based on a simplified approach [25-27]. This approach assumes Te inclusions to be geometrical spheres that punch holes in the electron cloud, which is also considered a sphere with an electric distribution described by a 3-D Gaussian function. This simple model does not account for variations in local electric fields, electron detrapping and extended areas of defects. The amount of charge left in the electron cloud after encountering a Te inclusion is

$$Q = Q_i \left(1 - n_i \left[1 - \exp\left(-\frac{D_i}{E_i \mu_i \tau_i}\right)\right]\right) \qquad (3)$$

where E_i is the local electric field and $\mu_i\tau_i$ product associated with the i'th inclusion. The product $E\mu\tau_i$ is the inclusion's attenuation length λ_i. The attenuation length averaged over all inclusions can be used to reduce the number of free parameters. We can assume nontransparent inclusions for the simplest case so that all electrons get trapped so that

$$\left(\frac{D_i}{E_i\mu_i\tau_i}\right) \gg 1 \qquad (4)$$

Therefore, the charge trapped by a Te inclusion depends on its effective diameter and its location with respect to the center of the electron cloud.

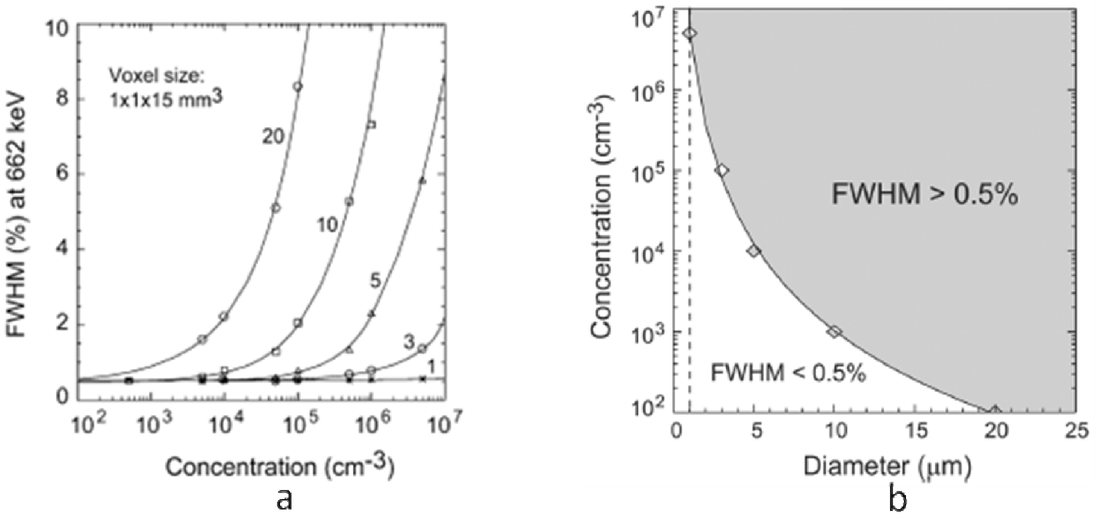

a

b

Figure 5.10 Simulated results using the model described above for 15 mm long CZT detector at 662 KeV. a) Energy resolution (% FWHM) versus concentration of Te inclusions of 1, 3, 5, 10 and 20 μm diameter, b) Regions where the contribution of Te inclusions to the peak width is greater (top) and less (bottom) than 0.5% FWHM [28].

Bolotnikov et al [28] have used this model to simulate the effect of presence and size distribution of Te inclusions on charge collection in CZT crystals. Fig. 10 shows simulated results in which the energy resolution increases as the diameter and concentration of Te inclusions increase [28].

5.6 Study of defects in CMT nuclear detectors

In this work we studied CMT crystals grown by modified low pressure Bridgman (MLPB) technique at Yinnel Tech [29]. Infrared microscopy was used to screen the crystals for the presence of defects, specifically twins and Te inclusions, and also to estimate the sizes and concentrations of Te inclusions in the CMT samples. A distinct pattern of twinning was also observed.

CMT, like other Zinc-blende crystals such as CdZnTe, belongs to a class of crystals that undergo birefringence, making it possible to probe the internal electric field using Pockels imaging. Pockels electro-optic effect has been used to probe the internal electric field of other crystals in the past [30, 31]. However there is no data reported on imaging the internal electric field in CMT crystals. In this study, the Pockels effect was used to measure the distribution of internal electric field of CMT crystals. This study shows, for the first time, the effect of a plane of Te inclusions on the internal electric field distribution of CMT radiation detectors.

5.6.1 Experiment: Four sets of 6x6x12 mm^3 CdMnTe crystals from two different ingots were used in this experiment. Ingot one crystal was indium-doped at 4 ppm while ingot 2 was 2.5-ppm indium doped. All other growth conditions were the same for both ingots. The crystals were mechanically polished with decreasing grit sizes of Al_2O_3 abrasive papers followed by alumina slurry also of decreasing sizes as described in section 3.2. The crystals were then etched with 2% Bromine-Methanol (BM) solution for 3 minutes, flushed with methanol and carefully cleaned to remove any residue from etching, and then blow-dried using nitrogen gas. 6x6x2.4 mm^3 samples were prepared for mobility-lifetime measurements, while 6x6x12 mm^3 samples were prepared for radiation response measurements. The sizes and distributions of Te inclusions in the bulk of the CMT crystals were studied with an IR microscope system developed at BNL to reveal the patterns of Te inclusions (Appendix A). The IR images of the crystal from ingot 2 reveals a region that has a thin plane of Te inclusions. This region was selected and a 6x6x6mm^3 sample was carefully cut out to feature the Te inclusion plane. This CdMnTe sample has only a single twin plane and was used for Pockels imaging and electric field studies. The sample was polished, etched and cleaned as described above. A Kurt J. Lesker sputtering system utilizing Radio frequency (RF) magnetron was used to deposit Au electrodes on the (111) planes as shown schematically in figure 11.

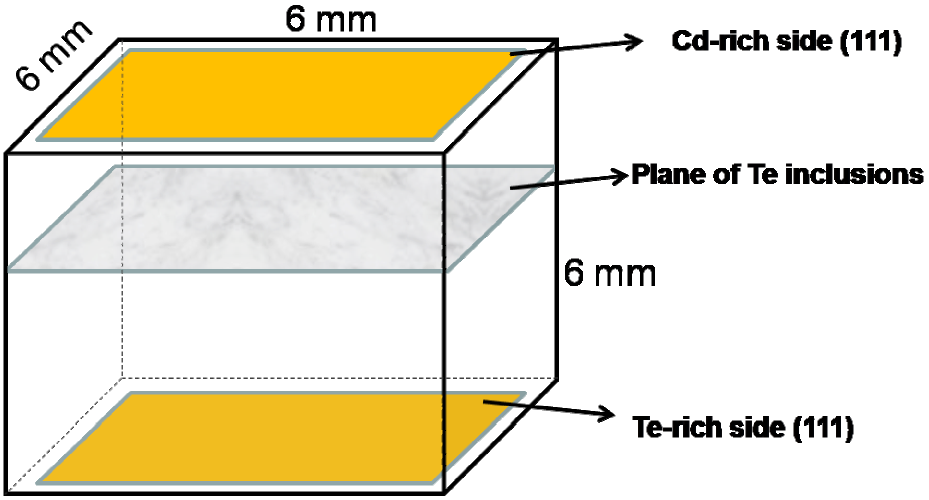

Figure 5.11 Schematic of 6 x 6 x 6 mm^3 CMT crystal showing a layer (plane) of tellurium inclusions.

Materials with zinc-blende structure possess a linear electro-optic effect, known as Pockels effect, in which the refractive index is modified anisotropically. The crystal is placed between a cross polarizer and analyzer. It is then irradiated with infrared light of wavelength below the band-gap of the crystal, and the total intensity of light is detected with a CCD camera. The intensity is given by

$$I = I_o Sin^2(\partial) \qquad (5)$$

Here I_o is the maximum transmitted light with aligned polarizers, and I is the difference between cross-polarized transmitted light between the biased and unbiased crystal. ∂ is the retardation of light beam passing through the crystal, expressed as

$$\partial = \frac{\pi n_o^3 r d}{\lambda} E \qquad (6)$$

Here *d* is the optical path length (thickness of crystal), r is the linear electro-optic coefficient, n_o is the field free refractive index, and E the mean electric field. Pockels images were obtained and analyzed with an IDL code specifically generated for this application to give the 3-dimensional distribution of internal electric field (See appendix B).

Two 6x6x12 mm^3 CdMnTe crystals from ingot #2 were fabricated in planar configuration for radiation response measurements. Planes of Te inclusions were observed in one of the crystals while the other crystal is relatively free of Te inclusion planes.

5.6.2 Results and discussions: CdMnTe crystals obtained from the two ingots show distinct differences. Firstly, as observed in Figure 12, ingot 1 crystals have a higher concentration of Te inclusions than crystals from ingot 2. Inclusions of larger diameters (10 μm to 36 μm diameter) are two orders of magnitude greater in ingot 1 crystals than ingot 2 crystals. Ingot 1 crystals feature three distinct size distributions of Te inclusions, i.e. ~5, 10 and 25 μm, while ingot 2 features a higher distribution of ~5 μm Te inclusions. Also, Te inclusions in ingot 1 crystals are more uniformly distributed within the bulk of ingot 1 crystals, but are more concentrated around a planar region in ingot 2 crystals. The major differences between Te inclusions in ingot 1 and ingot 2 are summarized in table 1 below.

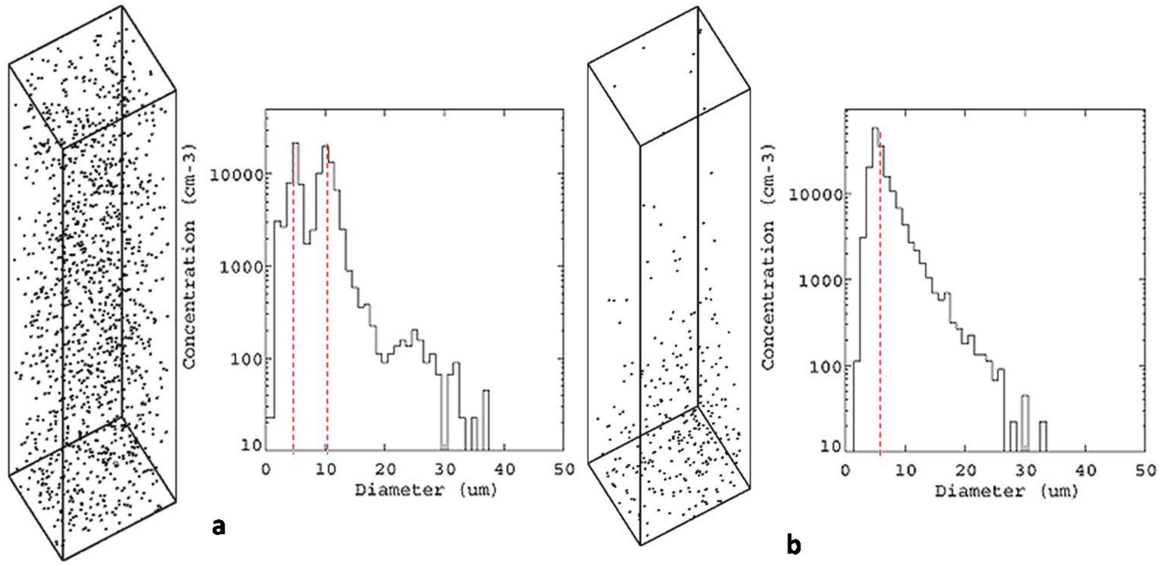

Figure 5.12 Concentration and size distribution of Te inclusions in a 1.5x1.5x6 mm^3 region of CMT crystal from (a) ingot 1 and (b) ingot 2.

Table 5. Comparison of Te inclusions between ingot 1 and ingot 2 crystals

	Ingot 1 (a)	**Ingot 2 (b)**
Indium doping (parts per million)	4	2.5
Conc. of Te inclusions (/cm^3 CMT)	3.45 x 10^5	9.5 x 10^4
Vol. of Te inclusions (?cm^3 CMT)	5.57 x 10^{-5}	2.43 x 10^{-5}
Conc. of Te inclusions (≥ 10μm dia./cm^3 CMT)	1.6 x 10^5	1.4 x 10^3

Another distinct difference observed is the arrangement of Te inclusions. Inclusions are randomly distributed across the volume of crystal obtained from ingot 1, but they are more localized in ingot 2 crystals, as seen in figure 13.

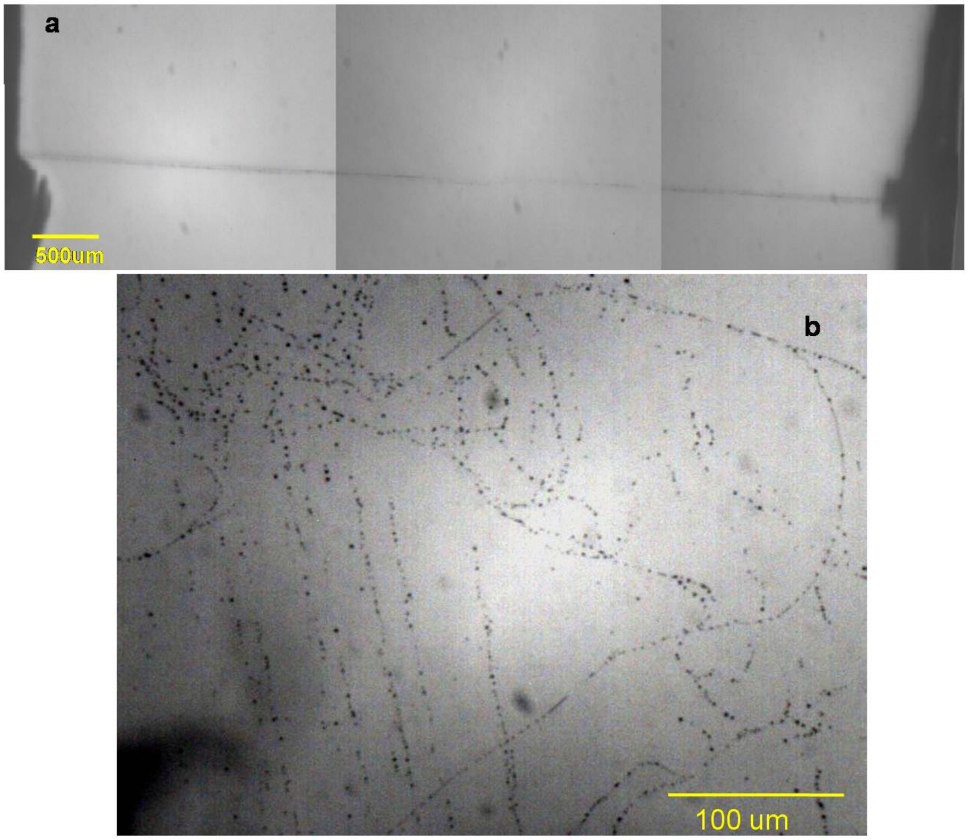

Figure 5.13 a) IR images of CMT crystal from ingot 1, a) stitched together to show a 'line' of Te inclusions from one side of the crystal to the other. b) showing the layer of Te inclusion. IR light is parallel to (111). The IR light is perpendicular to (111) direction.

Also, a distinct feature of Te inclusions in ingot 2 is the planar arrangement within the bulk of the crystal. Figure 13 shows a plane of Te inclusions observed both parallel to (observed from the side) and transverse to (observed from the top) the (111) plane. This plane of Te inclusions has characteristics of twin boundaries in its shape and orientation, forming along the closest-packed (111) plane.

5.6.3 Study with Pockels effect: Tellurium is hexagonal with smaller lattice unit cell edges than cubic CdTe, thereby Te inclusions induce strain in the CdMnTe lattice. Strain-induced birefringence is observed around the plane of Te inclusions with cross-polarized infrared images at zero bias as shown in fig. 14.

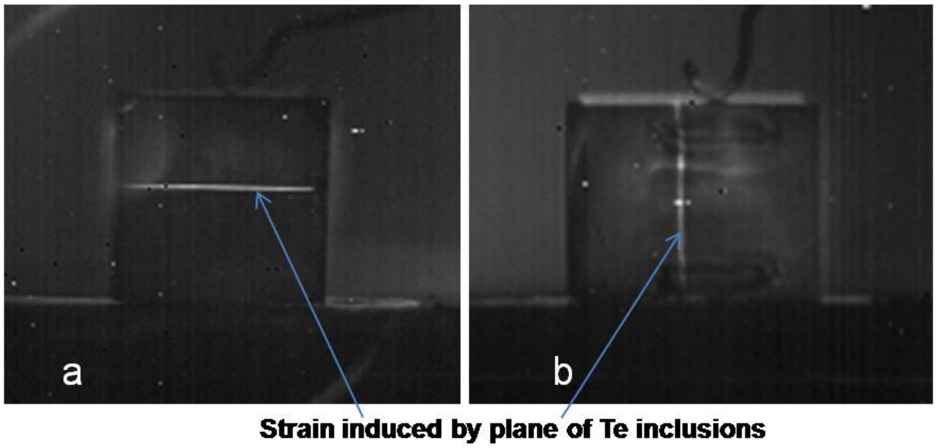

Figure 5.14 IR images of 6 x 6 x 6 mm^3 CdMnTe crystals from ingot 2 with cross-polarized IR light at zero bias, showing strain-induced birefringence due to the plane of Te inclusions.

The effect of a plane of Te inclusions on the electrical properties of CdMnTe was studied by Pockels electro-optic effect. Pockels images of the CdMnTe crystal taken at different bias is shown in fig. 5.15.

The intensity of cross-polarized light increases as the bias is increased, showing the expected increase in electric field due to increasing the bias. At higher bias, charge buildup is clearly observed as an increase in intensity of transmitted light around the region that corresponds to the position of the plane of Te inclusions.

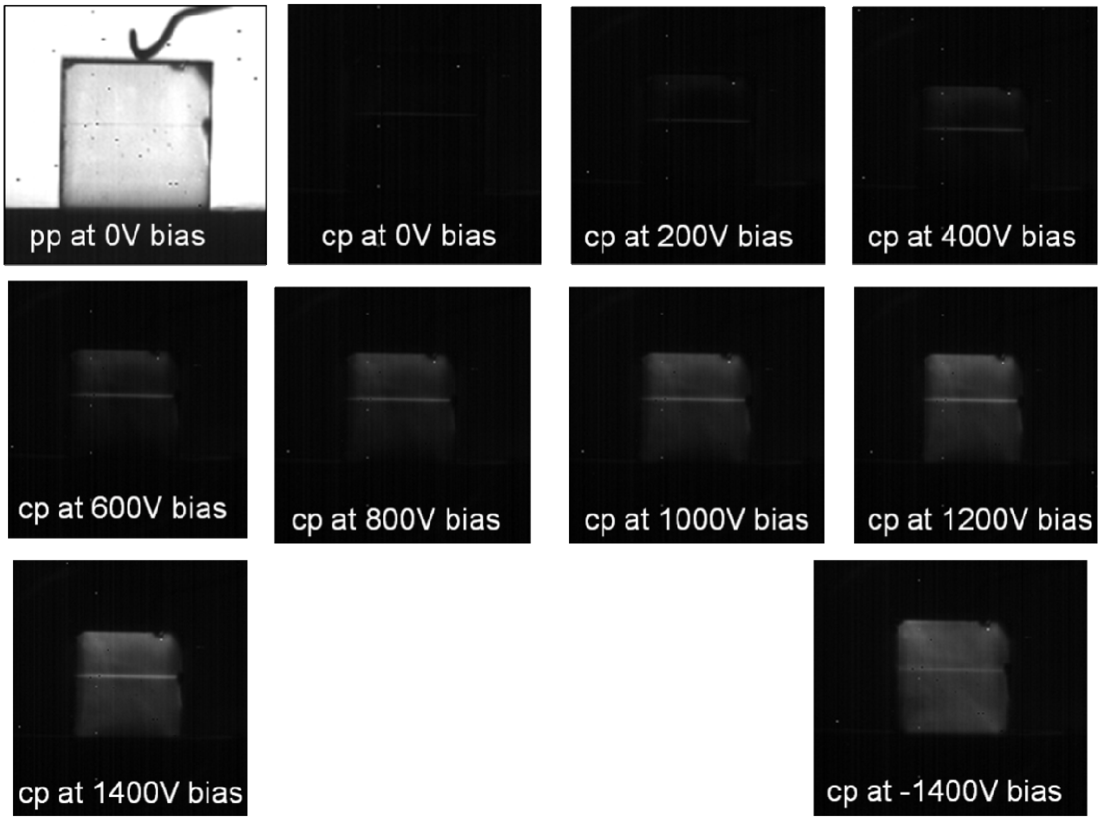

Figure 5.15 Pockel's images of the CMT crystal illustrated in figure 5.11. The electric field increases as the bias is increased. A charge buildup is observed at high bias around the position corresponding to the region around the Te inclusion as shown in fig. 5.14.

Here we observe that the plane of Te inclusions cause a buildup of electric field around the vicinity of the plane. Individual Te inclusions such as the sizes observed in the CdMnTe crystal behave as point defects and will not affect the uniformity of electric field within the bulk of the crystal.

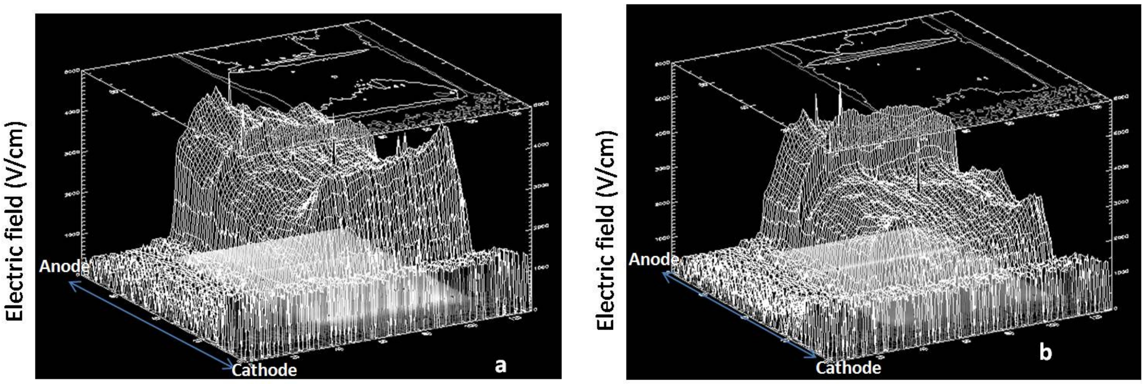

Figure 5.16 Electric field distribution evaluated for the CMT crystal a) at -1400 V applied bias and b) at +1400 V applied bias. Notice the contour map of the distribution showing distinct irregularity due to the localized plane Te inclusions. The Y-axis is parallel to direction of IR light (111 plane).

However a plane of Te inclusions as observed in this crystal will accumulate charges and distort the uniformity of electric field as shown in figures 5.15 and 5.16. The accumulation of charges around the region of Te inclusion plane causes a non-uniform distribution of the electric field within the bulk of the detector crystal. This non-uniformity is observed as deviation from the expected (theoretical) average electric field represented by the dashed lines in figure 5.17. The higher the electric field peak, the higher is the deviation from theoretical average electric field, i.e. the higher is the non-uniformity. On the average, the drift velocity of charge carriers, given as (where μ is the mobility of charge carrier and E is the electric field), will be less in regions with low electric field and high in regions with high electric field so that motion of charges will be compensated and so non-uniform electric field will not affect charge collection. When gamma interaction occurs near the cathode, an electron moving from the cathode to the anode will induce the same charge within both uniform and non-uniform electric field situations. However, when gamma

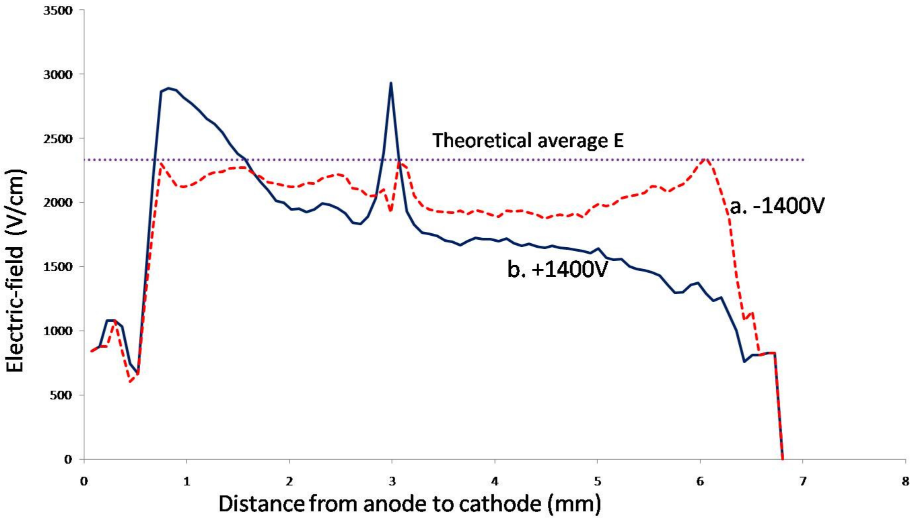

Figure 5.17 Electric field distribution of CMT crystal with a) negative bias, and b) positive bias. Sharp peaks are present at the region of the plane of Te inclusions.

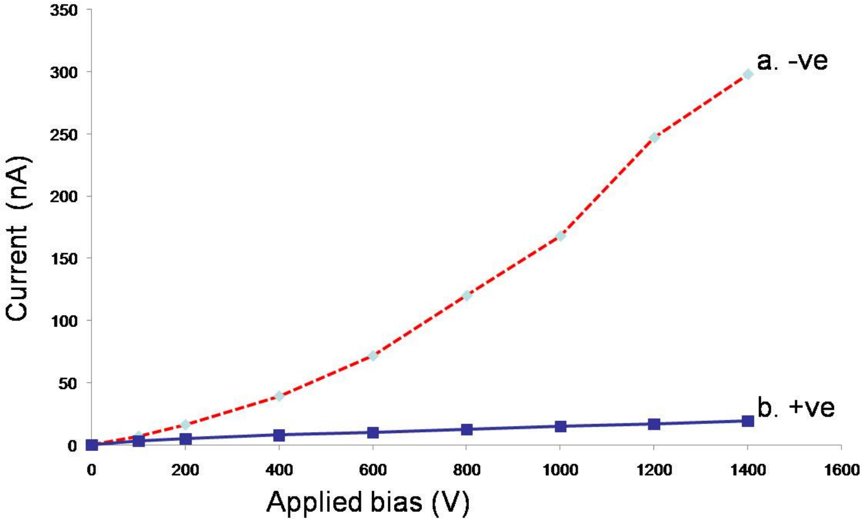

Figure 5.18 I-V characteristics measured during Pockels IR imaging, a. for negative bias, and b. for positive bias. The total current here is a combination of photo-induced and dark currents.

interaction with the material occurs at low electric field regions, the electric field may not effectively separate the generated electrons and holes and indeed charges may be lost through recombination, which will affect the collection efficiency and deteriorate detector performance.

Figure 5.16 shows the electric field profiles of the CdMnTe detector at an applied bias of 1400 V, calculated from Pockels images by equation 1 and assuming a value of 5.5 pm/V for the optical tensor, r_{41}, based on doped CdTe studies [32-34]. A negative bias was applied to the Te-rich side of the crystal in the case of Figure 16a, thereby making the detector forward-biased. In this configuration, electric field buildup around the cathode, anode and plane of Te inclusions are observed.

The electric field in the bulk is more uniform, and there is small distortion of electric field around the plane of Te inclusions.

Fig. 5.16b, however, shows the electric field profile obtained when the detector is reverse-biased by applying a positive bias to the Te-rich side of the crystal.

Higher intensity is observed around the plane of Te inclusions as seen in fig. 6b. The intensity increases with increase in applied bias (fig. 5) showing an increase in electric field around the Te inclusion plane.

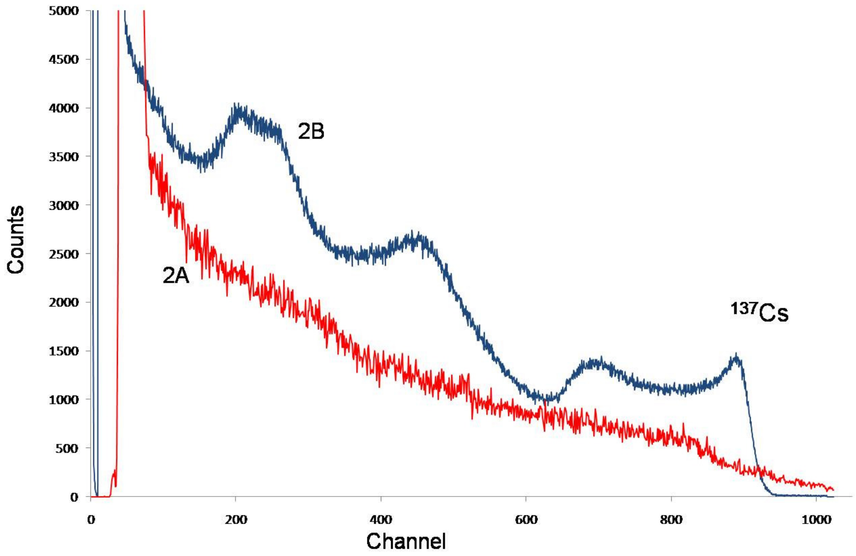

Figure 5.19 Response of two CMT bar detectors from ingot 2 (6x6x12 mm^3) to ^{137}Cs in planar configuration. Spectrum (2B) obtained from crystal relatively free of Te inclusion planes shows a peak corresponding to 662 keV of gamma radiation, while spectrum (2A) obtained from crystal with observed Te inclusion showed no response.

Figure 5.17 shows the different electric field profiles for a positively and negatively biased detector along the middle of the CMT crystal. The voltage is applied to the Te-rich (111) plane of the detector, and in this configuration the negative is forward-biasing while positive is reverse-biasing.

The CMT radiation detector performs best when reverse-biased to form a rectifying Schottky barrier as this reduces the charge-injected leakage current [35]. The current was measured as a function of applied bias and plotted in figure 5.8 for both forward and reverse biasing. As expected, a reverse biased detector gives much lower current of 19 nA, while forward biased detector gives a current of 298 nA when a bias of 1400 V was applied. However, reverse biased detector also shows higher charge buildup due to the plane of Te inclusions. Two 6x6x12 mm^3 CMT detectors (crystals 2A and 2B) from ingot 2 were tested; crystal 2A has observed planes of Te inclusions while crystal 2B is relatively free of Te inclusion planes. Figure 5.19 shows the spectra response of these two crystals. A photopeak that corresponds to 662 keV of gamma radiation is observed for crystal 2B, while crystal 2A shows no response. Although both crystals have low collection efficiencies, crystal 2B shows improvement over crystals from ingot 1 and 2A, as the other crystals show no response to gamma radiation.

5.7 Conclusion

The pattern, concentration and size distribution of Te inclusions in two batches of CMT ingots grown with varying indium concentrations of 4 ppm and 2.5 ppm respectively were studied. Ingot-1 crystals feature three different size distributions of Te inclusions, i.e. ~5, 10 and 25 μm, while ingot 2 contains mainly ~5 μm Te inclusions. The number of large Te inclusions (diameter ≥ 10 μm) are two orders of magnitude greater in ingot 1 than in ingot 2 crystals. The largest sized Te inclusions in ingot 1 are 20 μm in diameter, while in ingot 2 are 36 μm in diameter. Also, Te inclusions in ingot-1 crystals are more uniformly distributed within the bulk of ingot 1 crystals, but are more concentrated around a planar region of ingot-2 crystals. The effect of the plane of Te inclusions on the electric field distribution within the bulk of the crystal was shown in this study. A plane of Te inclusions was found to induce strain within the lattice and also accumulate more charges thereby creating higher non-uniformity of the electric field within the detector. Ingot 2 crystals indicate improvement in the growth of detector-grade CMT crystals. Changing the concentration of indium dopant is shown to influence the size and distribution of Te inclusions in grown CMT crystals. However, the twin planes decorated by Te inclusions will deteriorate detector performance and must be addressed to realize detector-grade CMT crystals.

REFERENCES

1. P. Rudolph, Cryst. Res. Technol. Vol. 38, n. 7-8, pp. 542-554, 2003.
2. P. Rudolph, M. Neubert, M. Muhlberg, J. Cryst. Growth 128 (1993) 582–587.
3. P. Rudolph, A. Engel, I. Schentke, A. Grochochi, J. Cryst. Growth 147 (1995) 297–304.
4. Y. Wang et al. / Journal of Crystal Growth 284 (2005) 406–411
5. K. Zanio, in: R.K. Willardson, A.C. Beer (Eds.), Semiconductors and Semimetals, Academic Press, New York, 1978, pp. 125–129.
6. G.W. Greenwood, A.J.E. Foreman, O.E. Rimmer, J. Nucl. Mater. 4 (1959) 305–324.
7. R.D.S. Yadava, B.S. Sundersheshu, M. Anandan, R.K. Bagai, W.N. Borle, J. Electron. Mater. 23 (1994) 1349–1357.
8. J. Zhu, J. Chu, X. Zhang, J. Cheng, J. Cryst. Growth 171 (1997) 357–360.
9. W.J. Kim, M.J. Park, S.U. Kim, T.S. Lee, J.M. Kim, W.J. Song, S.H. Suh, J. Cryst. Growth 104 (1990) 677–682.
10. H.Y. Pei, J.X. Fang, Phys. Status Solidi A 188 (2001) 1161–1167.
11. A. Hossain, Y. Cui, A.E. Bolotnikov, G.S. Camarda, G. Yang, D. Kochanowska, M. Witkowska-Baran, A. Mycielski, R.B. James. J. Elect. Mat. 38 (8) (2009) 1593.
12. G. Zha, W. Jie, T. Tan, L. Wang Phys. Stat. Sol. (a) 204, No. 7 (2007). pp. 2196
13. W.J. Everson, C.K. Ard, J.L. Sepich, B.E. Dean, G.T. Neugebauer, J. Electron. Mater. 24 (5) (1995) 505.
14. A.Koyama, A.Hichiwa, R.Hirano, J. Electron. Mater. 28 (1999) 683.

15. A.K.Garg, M.Srivastava, R.C.Narula, R.K.Bagai, V.Kumar, J. Crystal Growth 260 (2004) 148.
16. A.Fauler, A.Zwerger, M.Dambacher, M.Fiederle, IEEE Nucl. Sci. Symp. Conf. Rec.R01-4(2006)3585
17. G. S. Camarda, A. E. Bolotnikov, G. A. Carini, Y. Cui, K. T. Kohman, L. Li, and R. B. James. Proc. SPIE Conf. Hard X-ray, Gamma-Ray Detector Phys. Penetrating Radiat. Syst. 6319(2006)63190Z.1.
18. L. A. Franks, A. Burger, R. B. James, H. B. Barber, F. P. Doty, and H. Roehrig, Eds., “High spatial-resolution imaging of Te inclusions in CZT material,” in Proc. SPIE, Hard X-Ray and Gamma-Ray Detector Physics VIII, Bellingham, WA, 2006, vol. 6319.
19. K. Nakagawa, K. Naeda and S. Takeuchi, Appl. Phys. Lett. 34, 574 (1979).
20. G. A. Carini, A. E. Bolotnikov, G. S. Camarda, G. W. Wright, L. Li, and R. B. James, Appl. Phys. Lett. 88, p. 143515, 2006.
21. G. S. Camarda, A. E. Bolotnikov, G. A. Carini, and R. B. James, Countering Nuclear and Radiological Terrorism, edited by S. Aprkyan and D. Diamond, Springer, 2006, pp. 199-207.
22. A. E. Bolotnikov, G. S. Camarda, G. A. Carini, Y. Cui, L. Li, and R. B. James, “Nucl. Instr. Meth. A 571, pp. 687–698, 2007.
23. A. E. Bolotnikov, G. S. Camarda, G. A. Carini, Y. Cui, K. T. Kohman, L. Li, M. B. Salomon, and R. B. James, IEEE Trans. Nucl. Sci., NS 54, n 4, pp. 821 – 827, 2007.

24. E. Gatti, A. Longoni, P. Rehak, and M. Sampietro, Nucl. Instrum. Methods Phys. Res. A, vol. A253, pp. 393–399, 1987
25. A. E. Bolotnikov, G. S. Camarda, G. A. Carini, Y. Cui, L. Li, and R. B. James, "Cumulative effects of Te inclusions in CdZnTe radiation detectors," Nucl. Instrum. Methods Phys. Res. A, 2006, submitted for publication.
26. A. E. Bolotnikov, M. Black, G. S. Camarda, G. A. Carini, Y. Cui, K. T. Kohman, L. Li, M. Salomon, and R. B. James, (incomplete)
27. L. A. Franks, A. Burger, R. B. James, H. B. Barber, F. P. Doty, and H. Roehrig, Eds., "The effect of Te precipitates on characteristics of CdZnTe detectors," in Proc. SPIE, Hard X-Ray and Gamma-Ray Detector Physics VIII, Bellingham, WA, 2006, vol. 6319.
28. Y. Cui, M. Groza, G. W. Wright, U. N. Roy, A. Burger, L. Li, F. Lu, M. A. Black, R. B. James. J. Electr. Mater., Vol. 35, No. 6, (2006) 1267.
29. H. W. Yao, R. J. Anderson, R. B. James, and R. W. Olsen, Proc. Materials Research Society Symp. Vol. 487, (1998) 51.
30. A. Zumbiehl, M. Hage-Ali, P. Fougeres, J. M. Koebel, R. Regal, and P. Siffert, J. Crystal Growth 197, (1999) 650.
31. A. E. Bolotnikov, G. S. Camarda, Y. Cui, K. T. Kohman, L. Li, M. B. Salomon, and R. B. James, "Performance-Limiting Defects in CdZnTe Detectors", IEEE Trans. Nucl. Sci. 54, (2007) 821.
32. G. S. Camarda, A. E. Bolotnikov, G. A. Carini, Y. Cui, K. T. Kohman, L. Li, R. B. James, Proceedings of SPIE Conf. Hard X-ray and gamma-ray detector physics and penetrating radiation systems. Vol. 6319, (2006) 63190Z.1.

33. A. Cola, I. Farella, A. M. Mancini, and A. Donati, IEEE Trans Nucl. Sci. 54, No. 4 (2007) 1487.
34. R. B. Bylsma, P. M. Bridenbaugh, D. H. Olson, A. M. Glass, Appl. Phys. Lett. 51, no. 2, (1987) 889.
35. Y. Nemirovsky, A. Ruzin, G. Asa, Y. Gorelik, L. Li, J. Elect. Mater. 26, no 6, (1997) 756.

CONCLUSION

The findings associated with this thesis have contributed to the wider research efforts aimed at understanding the defects limiting the performance of CZT and CMT crystals as room temperature nuclear detectors. Understanding these defects will ultimately lead to ways of minimizing and/or eliminating defects thereby producing superior quality crystals for room temperature nuclear detector applications. The main conclusions are summarized below.

Surface defects

The National Synchrotron Light Source (NSLS) affords us the ability to, for the first time, use x-rays with micrometer-scale beam spots to probe the surface defects associated with surface preparation of CZT nuclear detectors. First we established the importance of surface preparation process for detector performance by explicitly showing the effect of surface roughness on detector's leakage current. Also employing the microscale x-ray mapping, we showed the detector performance to correlate with surface conditions (Chapter 3).

We then reported a detailed systematic study of surface preparation methods combining polishing and etching for achieving the desired optically flat and smooth surfaces (Chapter 4). The findings from this study propose an optimal surface preparation technique CZT and CMT crystals for nuclear detector applications. Specifically, a final polishing with 0.05μm grit size alumina slurry followed by etching with freshly prepared 5% Bromine-Methanol solution for five minutes was found to be an optimum surface preparation process. This process removes about 88% of surface damages as observed with the Atomic Force Microscopy (AFM) studies. This surface preparation achieves a superb surface smoothness with an average surface roughness feature not more than one nanometer in diameter.

Bulk defects

The studies reported in this thesis have immensely contributed to better understanding the defects in CZT and CMT crystals and how these defects affect the performance of the nuclear detectors based on the crystals. These studies have used experimental quantification of the concentration and size distribution of Te inclusions to support the model describing charge loss due to Te inclusions.

A major breakthrough in the research on semiconductors for room temperature nuclear detector applications is the realization of the first response of CMT crystals to high energy gamma rays. CMT was introduced as a new and promising material for room temperature nuclear detector applications by Arnold Burger in 1999 and research efforts have since been directed towards realizing x-ray and gamma ray detectors based on CMT crystals. This thesis reports the study of internal defects, specifically Te inclusions and precipitates. The study of the sizes, concentrations and distribution of Te inclusions in CMT crystals led to identification of unique planes of Te inclusions that is a characteristic of an otherwise promising CMT ingot. The effect of these characteristic planes on the internal electric field of detector crystals was reported. It was found that these Te inclusion planes induce stress and act as charge traps within the crystal. A careful selection, fabrication and testing of CMT crystals with less inclusion planes gave a spectral response, for the first time, to high energy gamma rays (response to 137Cs at 662KeV). The optimization of crystal growth conditions is proposed to realize detector grade CMT crystals. This optimization is best achieved by establishing a continued feedback loop between crystal growth, defect characterizations and detector performance testing of CMT and CZT crystals.

APPENDIX A

INFRARED IMAGING AND ALGORITHM

Infrared imaging

The sizes and distributions of Te inclusions in the bulk of the CZT and CMT crystals were studied with an infrared (IR) microscope system developed at Brookhaven National Laboratory. The system is automated to count and record the number and sizes of the Te inclusions within the bulk of the crystals. CZT and CMT crystals are opaque to visible light but transparent to IR light. The Te inclusions however have different optical properties and are opaque to IR light and so appear as dark spots in an IR image. The IR system consists of an illuminator, a backlight fiber optic that transfers the light through an optical condenser onto the sample. The sample is placed on a translational stage that consists of three actuators, each for the x, y and z Cartesian coordinates that are connected to a motion controller which is connected to a PC through serial connectors. Software was developed in C++ programming environment for communicating with the actuators.

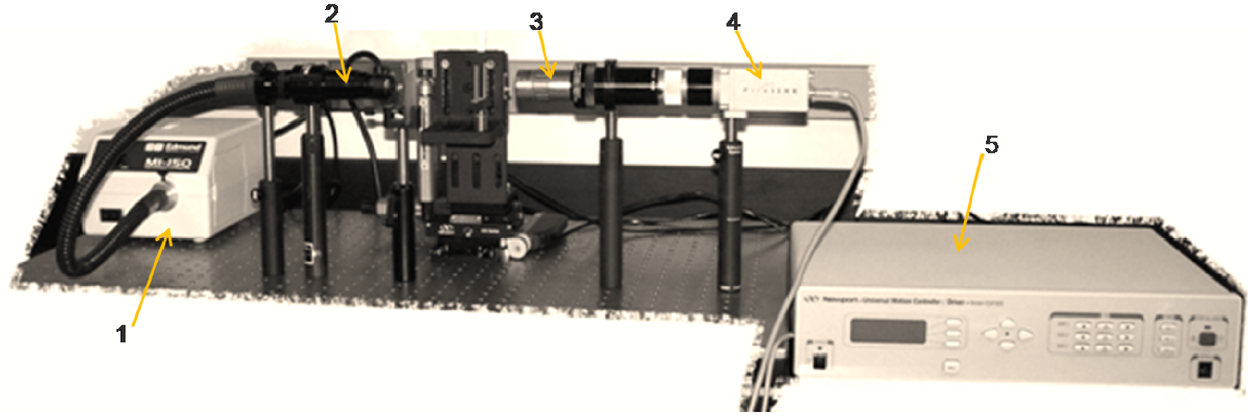

Figure A1. Infrared imaging setup.

Table A1. List of the major components of the IR microscopy system.

	Item	Manufacturer	Serial
1	High intensity illuminator	Edmunds Optics	MI-150
2	Optical condenser	Optem International	25-70-49
3	Objective lens	Mitutoyo American Corporation	K 00128904
4	CCD camera	Pixelink	PL-B955H
5	Motion controller	Newport	ESP 300

A large field-of-view (FOV) objective microscope is attached to the CCD camera using a lens adapter. An optics assembly system is mounted in-line with the translational stage and the backlight fiber optic. Different objective lenses with magnifications from 2x to 20x can be used, which correspond to a FOV of 5.3 mm (horizontal) x 3.8 mm (vertical) and 0.53 mm (horizontal) x 0.38 mm (vertical) dimensions respectively. The CCD camera used in the system is a Pixelink camera with sensor area of 7.8 mm x 10.6 mm and resolution of 2208 x 3000 pixels. The camera is connected to the PC by a firewire cable and is controlled by the C++ software. The system takes images one point after the other. The number of images taken at a point depends on the number of steps specified from one surface to the other as shown schematically in fig. 2. The step size for the scan depends on the depth of focus (DOF).

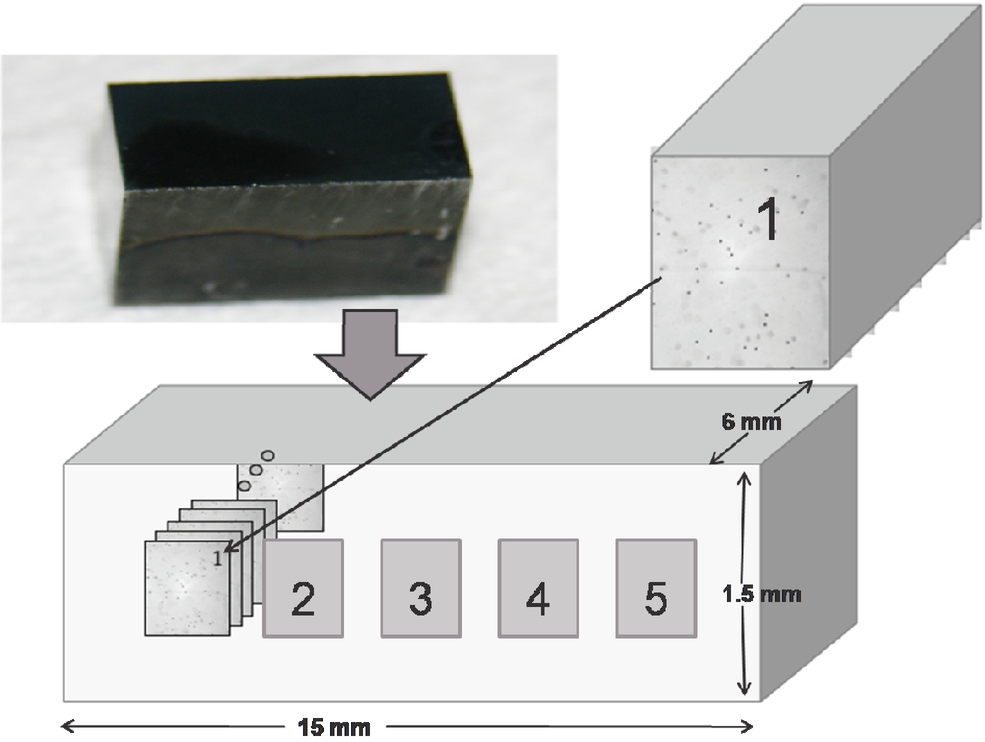

Figure A2. Schematics of the process of image capture by the IR microscopy system.

Iterative algorithm

An iterative algorithm was developed with Interactive Data Language (IDL) programming environment to count the Te inclusions present in the CZT and CMT crystals from the IR images and to measure their sizes, concentration, volume and excesses, as well as to reconstruct a 3-dimensional image of the crystal showing the positions of Te inclusions within the bulk of the crystal.

The first step of the algorithm involves converting the image to its negative image as shown in fig. 3. The negative image reveals large objects with relatively low brightness representing out-of-focus Te inclusions and compact objects with high brightness representing in-focus Te inclusions. The algorithm discards the Te inclusions that are out of focus and counts only those in focus. This is done in a two-step process. The first step is the background subtraction, in which the algorithm applies a cutoff on the brightness to suppress the contribution of objects of low brightness that represent out of focus Te inclusions. The second step selects only one Te inclusion present at the same position in 3 to 5 layers depending on the depth of field, while also correcting for shifts of images so that a Te inclusion is counted only once. This process is shown in figures 4 and 5.

The concentration of Te inclusions for each layer is calculated from the field-of-view, the size of the z-scan step and the number of Te inclusions for each layer. The algorithm also records the sizes of the Te inclusions, and can be modified to give the concentration, volume and excess of Te inclusions of a given radius.

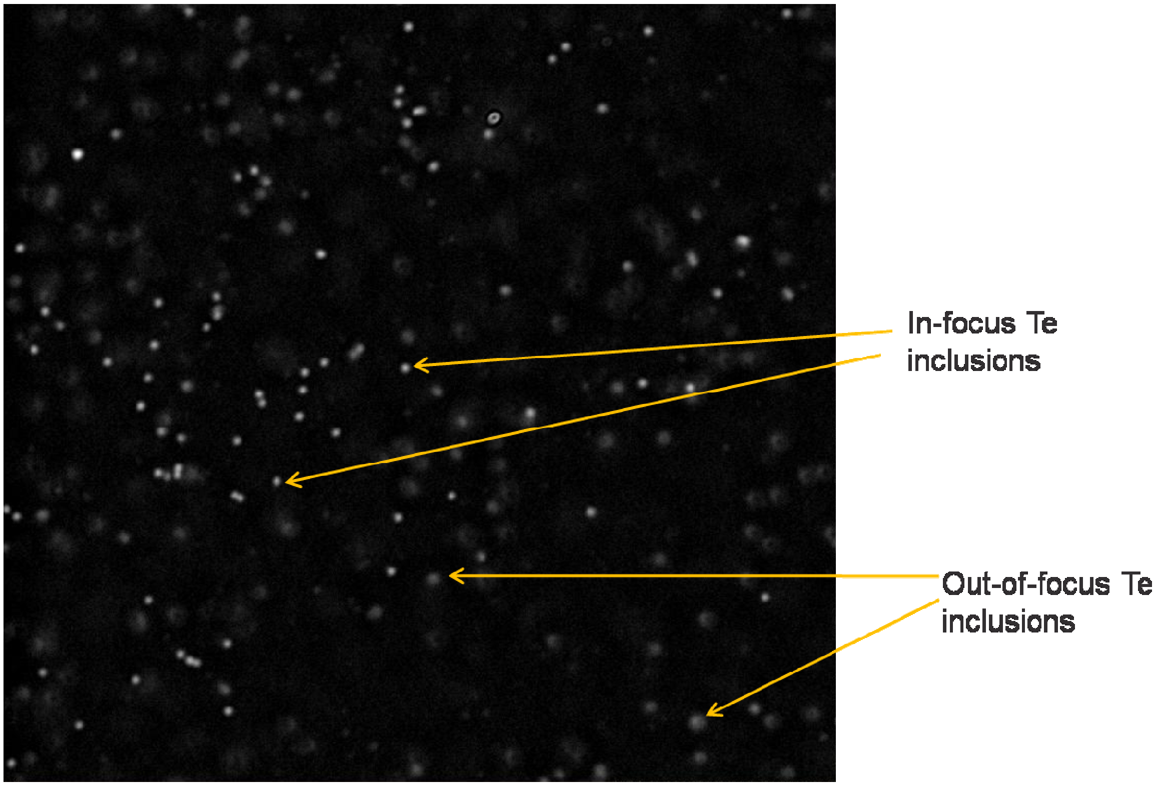

Figure A3. A negative infrared image of a section of CZT crystal showing in-focus and out-of-focus Te inclusions.

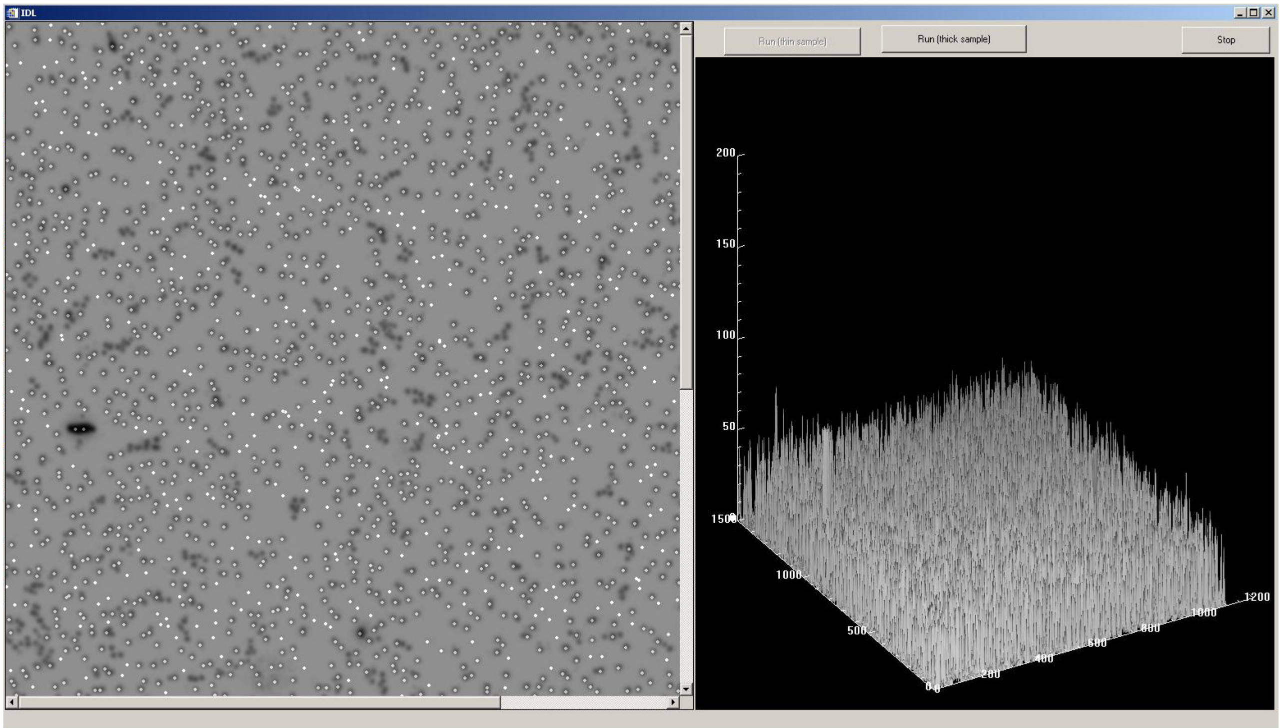

Figure A4. IDL iterative algorithm showing the background subtraction and counting process. Each object on the left plane is represented as a spectrum of inverted intensity against the position.

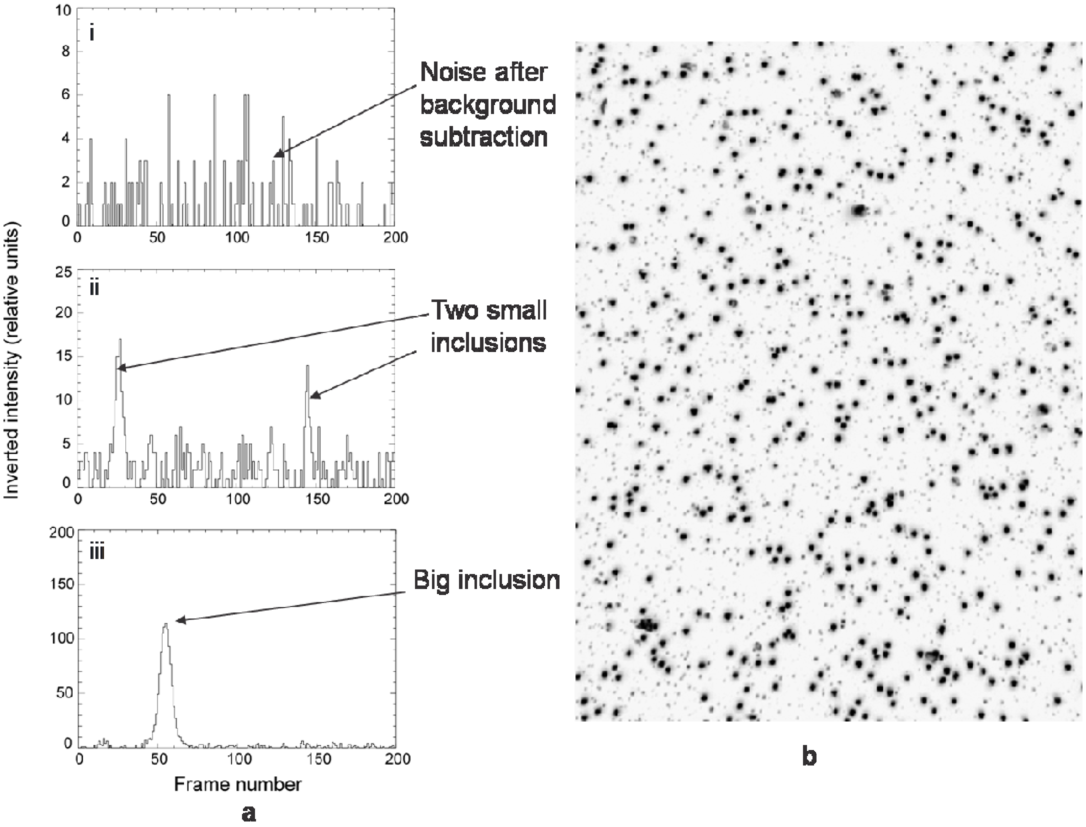

Figure A5 a) Spectra of inverted intensity showing i) the noise associated with the measurements, ii) two small inclusions and iii) a large inclusion. b) A stack of 200 images projected on a single plane after background subtraction.

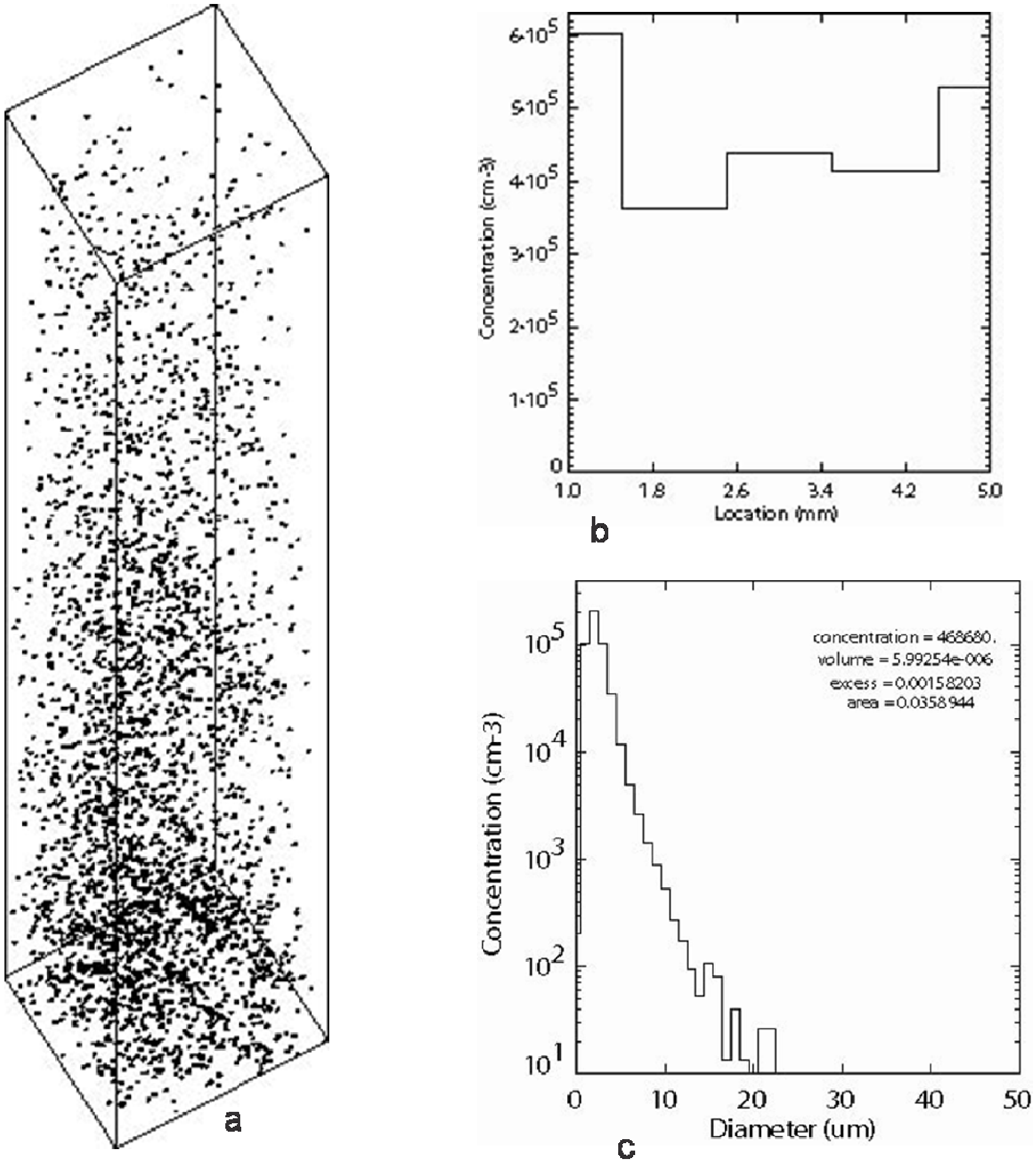

Figure A6. a) A 3-dimensional image showing the positions of the Te inclusions in the bulk of a 5 x 5 x 12 mm^3 CZT crystal. The image is reconstructed from the different infrared images of the CZT crystal using the algorithm. b) A plot of the concentration of Te inclusions against the location of the inclusions within the bulk of the CZT crystal, from one surface to the other. c) A histogram showing the concentration of Te inclusions according to their sizes.

APPENDIX B

POCKELS ELECTRO-OPTIC EFFECT AND ALGORITHM

Materials with zinc-blende structure possess a linear electro-optic effect, known as Pockels effect, in which the refractive index is modified anisotropically so that the crystal becomes birefringent in the presence of applied bias. Therefore, the electro-magnetic vector of the light is rotating with the intensity of the electric field throughout the detector. To employ the Pockels effect, the crystal is placed between two polarizers, i.e. a cross polarizer and analyzer. The crystal is then irradiated with infrared light of wavelength below the band-gap of the crystal, and the total intensity of light is detected with a CCD camera. The intensity is given by

$$I = I_o Sin^2(\partial) \tag{1}$$

Here I_o is the maximum transmitted light with aligned polarizers, and I is the difference between cross-polarized transmitted light between the biased and unbiased crystal. ∂ is the retardation of light beam passing through the crystal, expressed as

$$\partial = \frac{\pi n_o^3 rd}{\lambda} E \tag{2}$$

where *d* is the optical path length (thickness of the crystal), r is the linear electro-optic coefficient, n_o is the field free refractive index, and E the mean electric field. Pockels images were obtained and analyzed with an IDL code specifically generated for this application to give the 3-dimensional distribution of internal electric field.

Figure B1 shows the schematics of the Pockels effect setup. The setup consists of a light source, a narrow band infrared light filter, a set of polarizers (polarizer and analyzer) and the CCD camera. These components are shown in figures B2 and B3. Figure B4 shows the light source and associated power supply, as well as the high voltage power supply.

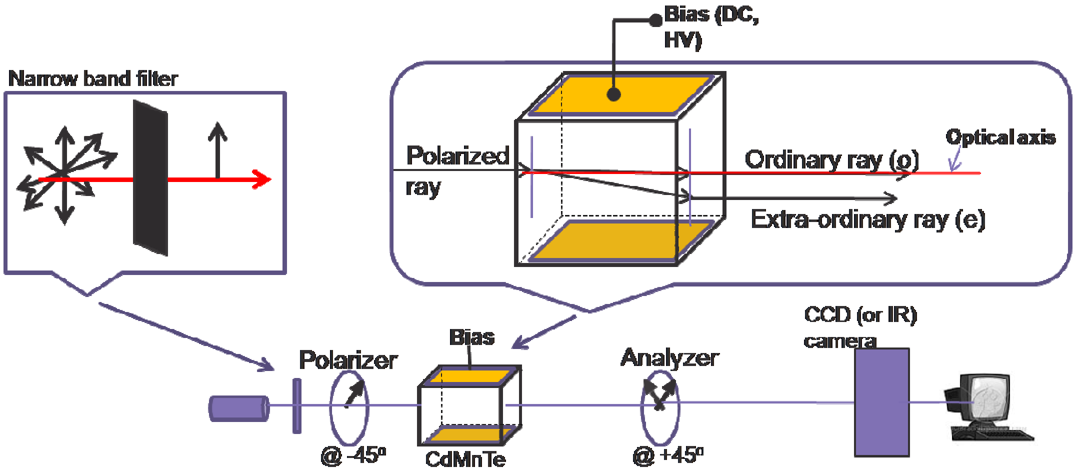

Figure B1. Schematics of Pockels effect measurement setup

Figure B2. Pockels effect setup at BNL

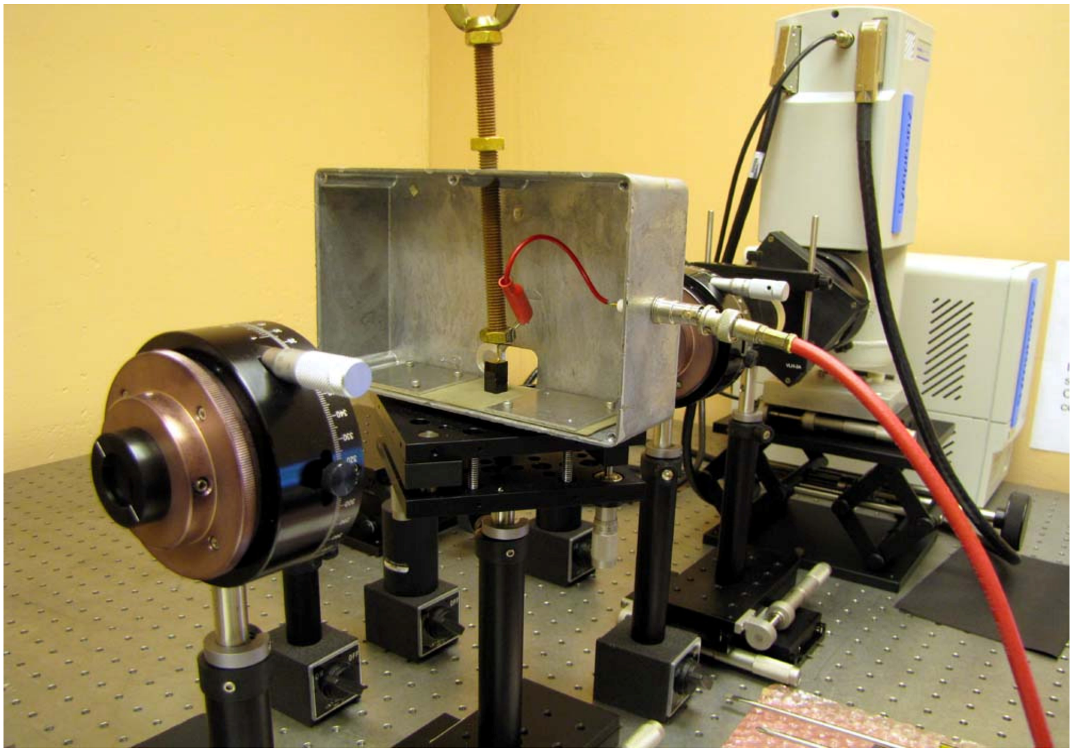

Figure B3. Pockels effect setup. The Sample holder with a CZT crystal, the polarizer, analyzer, high voltage power supply connector and the CCD camera can be seen.

Figure B4. Pockels effect setup. The light source and associated power, as well as the high voltage power supply are seen.

IDL algorithm

Interactive data language (IDL) is a programming language that is very useful for analysis of scientific data and visualization. The syntax is based on FORTRAN syntax and also includes some C programming constructs. Using IDL, we have developed an algorithm for calculating and visualizing the internal electric field within the bulk of CZT and CMT crystals. The algorithm is simplified into five steps as appears below.

IDL algorithm steps

1. Images are read into IDL and the windows' attributes are defined.
2. Images are converted to floating point arrays of numbers. For each image, two vectors are constructed containing the x and y position, respectively, of the array.
3. A bilinear interpolation of the image values is conducted
4. Image math is processed to subtract the Pockels images of biased crystal from the unbiased crystal with cross-polarized transmitted light.
5. The electric field is computed and visualized.

A flowchart of the algorithm featuring the steps and processes of calculating and visualizing the internal electric field is shown in figure B5. With further work, this algorithm can be developed into a software with a user interface that can useful for the automation of internal electric field imaging which can ultimately lead to a new imaging instrumentation for crystal selection in device fabrication industries.

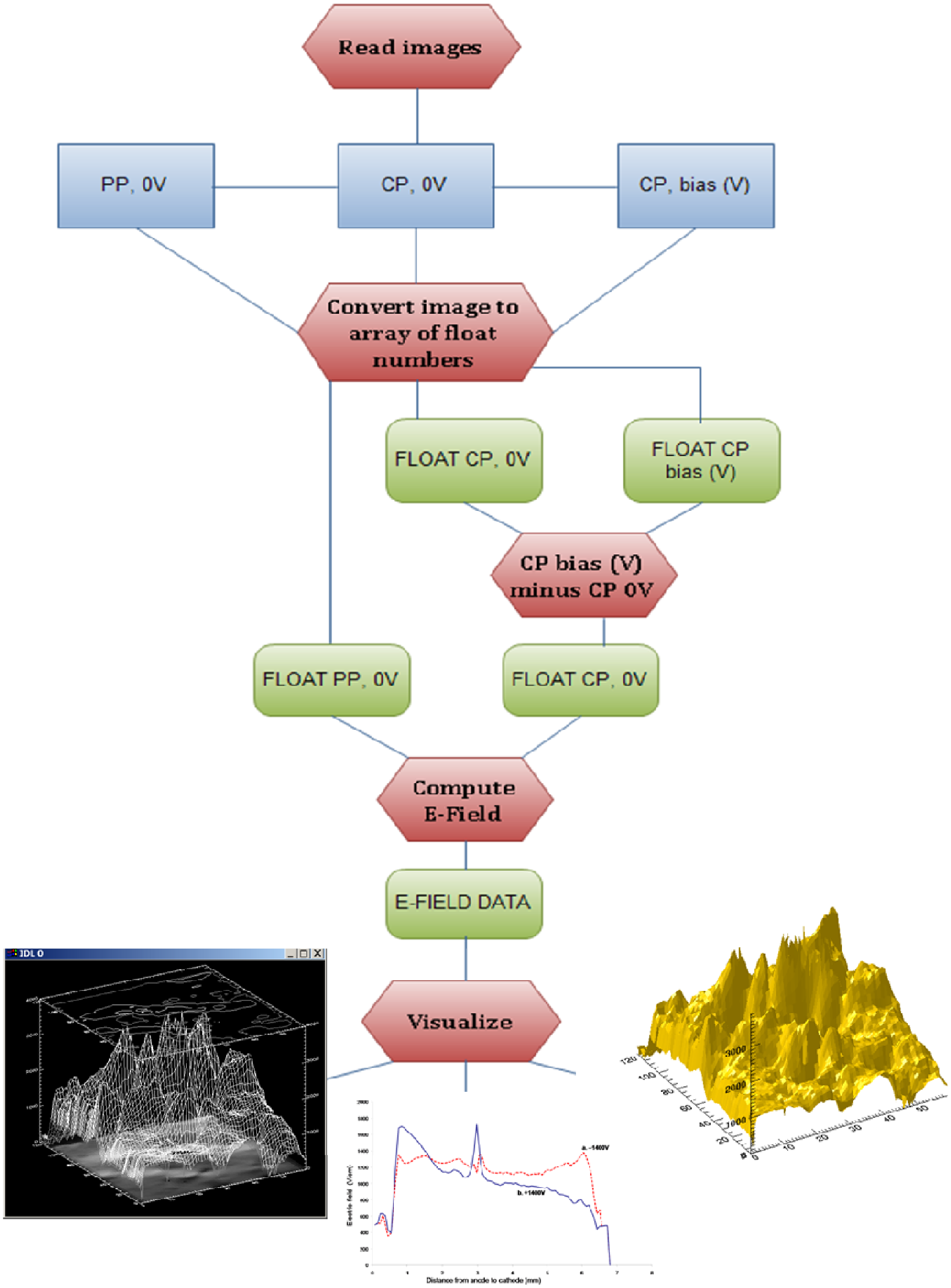

Figure B5. Flowchart of IDL algorithm for processing Pockels images